NTNU
Norwegian University of
Science and Technology

Energy utilization from deep geothermal sources

Daniel Ommedal

Master of Energy and Environmental Engineering
Submission date: June 2018
Supervisor: Erling Næss, EPT
Co-supervisor: Silje Bordvik, EPT
Lars O. Nord, EPT

Norwegian University of Science and Technology
Department of Energy and Process Engineering

NTNU
Norwegian University
of Science and Technology

Department of Energy
and Process Engineering

EPT-M-2018-64

MASTER THESIS

for

Student Daniel Ommedal

Spring 2018

Energy utilization from deep geothermal sources

Energiutnyttelse fra dype geotermiske kilder

Background and objective

Geothermal energy is a renewable energy resource having a large potential for utilization in heating and/or power production.

Recently, heat extraction from supercritical water (i.e. high pressure and high temperature) has received significant attention. Supercritical water from aquatic reservoirs several kilometers below the surface is led to the surface, and the thermal and potential energy is converted to electricity in steam turbines. This technology is presently on the experimental/demonstration stage, but the potential is vast. Norway has, from its oil and gas exploration knowledge and expertise in well-boring, a potential of taking a leading role in the international geothermal industry.

The main focus of the project work will be to analyze the problems associated with heat extraction from the ground (ca. 5 km or more below the surface) and the usage of the heat in power production applications.

The following tasks are to be considered:

1. The properties of a generic hydrothermal well is to be established in cooperation with the Department. In this respect, the relevant well and fluid properties shall be presented, and their possible variation ranges shall be discussed and presented.
2. For the generic case described in Part 1, a methodology for the fluid pressure and enthalpy for various relevant flow rates shall be developed, and the top-site conditions shall be calculated and presented.
3. Electric power production from the wellbore fluid shall be evaluated. Based on the analysis of Parts 1-3, one or more possible power cycle designs shall be proposed, and their total efficiencies shall be determined. Based on the results, recommendations shall be made.
4. Suggestions for further work shall be made.

The master thesis is a continuation of the project work.

-- ” --

Within 14 days of receiving the written text on the master thesis, the candidate shall submit a research plan for his project to the department.

When the thesis is evaluated, emphasis is put on processing of the results, and that they are presented in tabular and/or graphic form in a clear manner, and that they are analyzed carefully.

The thesis should be formulated as a research report with summary both in English and Norwegian, conclusion, literature references, table of contents etc. During the preparation of the text, the candidate should make an effort to produce a well-structured and easily readable report. In order to ease the evaluation of the thesis, it is important that the cross-references are correct. In the making of the report, strong emphasis should be placed on both a thorough discussion of the results and an orderly presentation.

The candidate is requested to initiate and keep close contact with his/her academic supervisor(s) throughout the working period. The candidate must follow the rules and regulations of NTNU as well as passive directions given by the Department of Energy and Process Engineering.

Risk assessment of the candidate's work shall be carried out according to the department's procedures. The risk assessment must be documented and included as part of the final report. Events related to the candidate's work adversely affecting the health, safety or security, must be documented and included as part of the final report. If the documentation on risk assessment represents a large number of pages, the full version is to be submitted electronically to the supervisor and an excerpt is included in the report.

Pursuant to "Regulations concerning the supplementary provisions to the technology study program/Master of Science" at NTNU §20, the Department reserves the permission to utilize all the results and data for teaching and research purposes as well as in future publications.

The final report is to be submitted digitally in DAIM. An executive summary of the thesis including title, student's name, supervisor's name, year, department name, and NTNU's logo and name, shall be submitted to the department as a separate pdf file. Based on an agreement with the supervisor, the final report and other material and documents may be given to the supervisor in digital format.

☐ Work to be done in lab (Water power lab, Fluids engineering lab, Thermal engineering lab)

☐ Field work

Department of Energy and Process Engineering, 15. January 2018

Erling Næss

Erling Næss
Academic Supervisor

Research Advisor:
Silje Bordvik, ph.d.-student
Lars O. Nord, Associate professor

Preface

This master's thesis regarding Energy utilization from deep geothermal sources was carried out at the Norwegian University of Science and Technology, NTNU Trondheim, during the spring semester of 2018. The thesis comprises 30 credits in the 10^{th} and last semester of my Master degree in Energy and Environmental Engineering at the Department of Energy and Process Engineering.

Trondheim, 27-06-2018

Daniel Ommedal

Department of Energy and Process Engineering

Acknowledgment

"GOD Thank you for giving me the strength and encouragement especially during all the challenging moments in completing this thesis. I am truly grateful for your exceptional love and grace during this entire journey".

First and foremost, my deepest gratitude to my head supervisor, Prof. Erling Næss, for his patience, continuous supervision, guidance, advice, and support in completing this thesis. My sincere gratitude my co-supervisor, PhD Candidate Silje Bordvik, which has provided fruitful discussion regarding the development of supercritical water systems.

Finally, I would like to thank my family and friends with all my heart for being helpful and supportive during my time studying Environmental Engineering at the Norwegian University of Science and Technology.

Abstract

Recently, heat extraction from supercritical water (i.e. high pressure and high temperature) has received significant attention. Supercritical water from aquatic reservoirs several kilometres below the surface are led to the surface, and the thermal and pressure energy is converted to electricity in steam turbines. This technology is presently on the experimental/demonstration stage, but the potential is huge.

A case study is conducted to explore the potential for electric power generation from a supercritical geothermal reservoir situated 5 km below the surface with a temperature and pressure of 500°C and 230 bar, respectively. Evaluations of the fluid composition of deep geothermal wells at the most significant geothermal sites on Iceland, prove that the chemical composition of geothermal fluids highly depends on the geologic condition of the reservoirs. Based on the laws of thermodynamics, a program for calculating temperature, enthalpy and pressure variations during extraction from reservoir to wellhead for high temperature and high pressure geothermal fluids is obtained. Calculations on the case study reveal a pressure drop of 70 bar and a temperature loss of 55°C during extraction, resulting in a superheated fluid at 459°C and 160 bar available at the wellhead. The wellhead condition is further analyzed for electric power production by evaluating five power cycle designs. The most efficient design, containing three turbines, two heat exchangers and one throttling valve, resulted in a calculated electrical power output of 38.37 MW_e, a total efficiency of 24% and a predicted energy production of 302.5 GWh/year. These results suggest that if the geothermal power cycle for the most efficient design analyzed could be realized with the given assumptions, it would be one of the (if not the) most efficient geothermal power plants worldwide.

Sammendrag

I den senere tid har utnyttelse av energi fra hydrotermale brønner med superkritisk vann (dvs. høyt trykk og høy temperatur) blitt fokusert. Superkritisk vann hentes fra vannreservoarer flere kilometer under overflaten og opp til overflaten, hvor trykket og den termiske energien blir konvertert til elektrisk energi ved hjelp av dampturbiner. Denne teknologien er foreløpig på eksperiment-/demonstrasjonsstadiet, men potensialet er betydelig.

Et case-studie er gjennomført for å undersøke potensialet for elektrisk kraftproduksjon fra en superkritisk geotermisk brønn lokalisert 5 kilometer under overflaten med temperatur og trykk på henholdsvis 500°C og 230 bar. En evaluering av fluidsammensetningen av dype geotermiske brønner på Island viser at kjemisammensetningen av geotermiske fluider i stor grad avhenger av brønnens geologiske tilstand. Basert på de termodynamiske lovene, er et program utviklet for å beregne trykk- og entalpivariasjoner ved utvinning av det geotermiske fluidet fra reservoaret til brønnhodet. Gjennomførte beregninger på case-studiet viser et trykkfall på 70 bar og et temperaturfall på 55 °C ved utvinning, noe som resulterer i at det geotermiske fluidet går over i det underkritiske området. Ved brønnhodet er fluidet tilgjengelig som overhetet damp ved en temperatur og trykk på henholdsvis 459 °C og 160 bar. Fluidet er videre analysert for elektrisk kraftproduksjon ved å evaluere fem modeller for kraftproduksjon. Den mest effektive modellen, som er bygd opp av en strupeventil, to varmevekslere og tre turbiner, resulterte i en beregnet elektrisk effekt på 38.37 MW_e, en total effektivitet på 24% og en forventet energiproduksjon på 302.5 GWh/år. Disse resultatene antyder at dersom den mest effektive modellen analysert i dette studiet kunne realiseres med de forutsetningene tatt, ville den være en av de (om ikke den) mest effektive geotermiske kraftverkene produsert.

Contents

List of Figures

List of Tables

Abbreviations

IAPWS The International Association for the Properties of Water and Steam

IAPWS-IF97 IAPWS Industrial Formulation 1997 for the Thermodynamic Properties of Water and Steam

IDDP Iceland Deep Drilling Projec

KG-# Well located in the Krafla geothermal field

KhG-# Well located in the Kolvidarholl geothermal field

KJ-# Well located in the Krafla geothermal field

NJ-# Well located in the Nesjavellir geothermal field

RN-# Well located in the Reykjanes geothermal field

LCOE Levelized Cost of Electricity is an economic assessment of the average total cost to build and operate a power-generating asset over its lifetime by the total energy output of the asset over that lifetime.

MATLAB (Matrix Laboratory) is a multi-paradigm numerical computing environment

NTNU Norwegian University if Science and Technology

PHREEQC A Computer Program for Speciation, Batch-Reaction, One-Dimensional Transport, and Inverse Geochemical Calculations

TEPP A MatLab Script for Calculations of Temperature, Enthalpy & Pressure variations in Extraction of Geothermal Fluids

X Steam A matlab.m file, which is an implementation of the IAPWS IF97 standard formulation.

WATCH A Computer Program for Calculating Aqueous Speciation in Natural Waters

Nomenclature

Constants

g	gravitational acceleration (9.81 m/s^2)

Greek Symbols

α	Angle between pipe axis and horizontal direction
ϵ	Pipe Roughness
η	Energy conversion efficiency
η_T	Isentropic efficiency
η_g	Generator efficiency
λ	Darcy friction factor
$\bar{\lambda}$	Additional friction factor
μ	Viscosity
ρ	Density
χ	Vapour quality

Latin Letters

A_{ht}	Heat transfer area
D	Pipe Diameter
h	Enthalpy
L	Pipe Length
$\dot{m}$	mass flow rate
P	Pressure
P_{is}	Isentropic Pressure
$\dot{Q}$	Heat transfer rate
Re	Reynolds Number
T	Temperature
T_{is}	Isentropic Temperature
T_∞	Temperature in surrounding rock
U	Overall heat transfer coefficient
v	Velocity
$\dot{W}$	Work rate
$\dot{W}_e$	Generated electric power
z	Vertical axis

Chapter 1

Introduction

1.1 Background

Geothermal energy is an abundant renewable energy resource, which could be accessed throughout the world. The interest in geothermal energy has grown rapidly as the demand for clean and renewable energy has increased. The potential for geothermal energy is enormous, estimates suggest that geothermal energy sources contain 50,000 times the energy of all oil and gas resources in the world (Vision and Mission, 2009).

Geothermal energy has some unique features. It is continuous and the energy production rate is independent of local weather conditions, which makes geothermal energy ideal as a base load since it provides a stable and predictable energy production. Despite significant potential, geothermal energy utilization faces several barriers to growth. These issues include limited geothermal siting opportunities, inadequate technology, and high investment costs related to drilling and reservoir stimulation. As a result, commercial operation of geothermal power plants is only feasible at sites with special geological conditions. Accordingly, the geothermal industry aims to improve the exploration and production from geothermal systems, including the development of enhanced geothermal systems (EGS) and heat extraction from supercritical water. Present geothermal power generation comes from hydrothermal reservoirs and is somewhat limited in geographic application to specific ideal areas. The development of the EGS concept which includes the extraction of heat by creating subsurface fracture systems to which water can be added through injection wells, allow a wider application for geothermal energy production. (Tester et al., 2006)

Recently, heat extraction from supercritical water (i.e. high pressure and high temperature) has received significant attention. Supercritical water from aquatic reservoirs several kilometres below the surface is led to the surface, and the thermal and pressure energy is converted to electricity in steam turbines. Supercritical water systems contain much greater enthalpy and transfer abilities compared to subcritical or conventional hydrothermal systems. These

benefits can improve the power output with 5 to 10 times compared to a typically developed subcritical liquid dominated resource, which may result in considerable improved cost efficient geothermal systems (Tester et al., 2006). This technology is presently on the experimental/demonstration stage, but the potential is huge. Norway has, from its oil and gas exploration knowledge and expertise in well-boring, a potential of taking a leading role in the international geothermal industry.

Accordingly, the Norwegian University of Science and Technology aims to develop projects in the field of geothermal energy utilization from deep geothermal resources.

1.2 Objectives, limitations and remaining work

The main objective of this thesis was to analyze the problems associated with heat extraction from the ground (about 5 km or more below the surface) and the use of heat in power production. To achieve the main objective, it was divided into three.

- Establishing the properties of a generic hydrothermal well: The first task was to determine the properties of a generic hydrothermal well at the depth in consideration. Including temperature, pressure and fluid composition based on available literature.
- Developing a methodology for calculating fluid pressure and enthalpy during extraction from a reservoir to wellhead: Based on the properties of the established generic hydrothermal well, the second task involved developing a methodology for calculating pressure and enthalpy variation during extraction of the geothermal fluid and determining top-site conditions.
- Evaluate electric power production from the wellbore fluid: As a result of the calculations of the top-site conditions, the last task involved developing and evaluating one or more possible power cycle designs in addition to determining their total efficiencies and providing recommendations.

Furthermore, it was initially intended to calculate chemistry equilibrium throughout the geothermal power plant to determine corrosion and deposition potential. In such, a comprehensive attempt was carried out to obtain software for such calculations, concluding in that chemical equilibrium calculations at close to supercritical conditions was not possible for the software examined. However, the chemistry variation ranges in the generic hydrothermal well is discussed, but its effect during power utilization remains to be determined.

The developed methodology for calculating enthalpy and pressure variations during extraction of the geothermal fluid from a reservoir to wellhead should be verified with experimental data. However, such data for supercritical water or superheated steam could

not be acquired during this study. First of all, temperature and pressure logs at these conditions prove highly expensive as it requires equipment which could resist high pressure and temperatures as well as the chemical composition of the fluid. Secondly, an attempt at retrieving such information from some large geothermal energy companies was attempted, resulting in a conclusion that such information is of sensitive concern.

Thus, obtaining a software for calculating chemistry equilibrium at close to supercritical conditions and obtaining pressure and enthalpy logs from deep geothermal wells is, along with other elements, mentioned as a proposal for further work.

1.3 Outline of the report

This report is basically divided into three main parts, starting by determining the properties of a generic hydrothermal well, following developing a method for calculating thermodynamic properties during extraction of the geothermal fluid, and finally analyzing five power cycle designs for electric power production from the fluid.

The first part commences with a literature study on the chemical composition and thermodynamic properties of previous drilled deep geothermal wells in Iceland to determine the properties of a generic hydrothermal well. In such, the three main geothermal sites on Iceland along with their chemical characteristics and potential for exploitation of supercritical water is discussed. Furthermore, the characteristics of two supercritical wells, IDDP-1 and IDDP-2, are presented and a further approximation on the geothermal fluid contained in the reservoir of IDDP-2 is carried out. Subsequently, as a result of the literature study, a discussion regarding chemistry variation ranges for the deep geothermal wells is carried out, resulting in the properties of a generic hydrothermal well which is referred to as the case study.

The second part of this report presents a methodology for calculating temperature, enthalpy and pressure variations during extraction of the geothermal fluid from a reservoir to wellhead. Starting by deriving the theoretical background for the method, presenting the method, and arriving at a presentation and discussion of the results obtained from the case study well.

The final and third part evaluates five possible power cycle designs based in the available fluid at the wellhead. As such, their characteristics and effectiveness are presented and discussed and recommendations are made.

Conclusions of this study and a recommendations for further work completes the report.

Chapter 2

Chemical Composition of Deep Hydrothermal Fluids

This chapter commences with an introduction to chemistry variations of geothermal fluids. Subsequently, based on available literature, an overview of the largest geothermal sites in Iceland is presented (Fig. 2.1). In such, a discussion regarding their chemical characteristics and potential for obtaining supercritical conditions is carried out. Furthermore, the Iceland Deep Drilling Project has completed two wells, IDDP-1 and IDDP-2, aiming to explore the potential of energy utilization from supercritical water on Iceland. The development of these wells along with a discussion regarding their chemical composition is carried out in this chapter. Based on the chemistry of the geothermal wells presented, their variations and main compounds of concern are discussed. A summary and a presentation of a generic hydrothermal well conclude the chapter.

2.1 Genesis of Geothermal Fluids

The chemistry of geothermal fluids highly depends on the origin and evolution of the fluids and solutes contained. In the early stages of geothermal field exploration, it was thought that the source of fluids, solutes and heat of geothermal systems originated from magmas. However, in the 1960's this model was radically changed when it was demonstrated that the fluids were dominant of meteoric origin, while solutes could be derived from rock-water reactions. The solutes may also be contributed by mixing with seawater, formation waters or magmatic brine. Although there is no doubt that the fluids are dominant of meteoric origin, isotopic signatures of fluids show that 5–10% of the fluid can be formed from alternative sources, such as a magmatic brine. Mixing with even a small amount of magmatic brine would significantly affect the chemistry of the final geothermal fluid. (Nicholson, 1993)

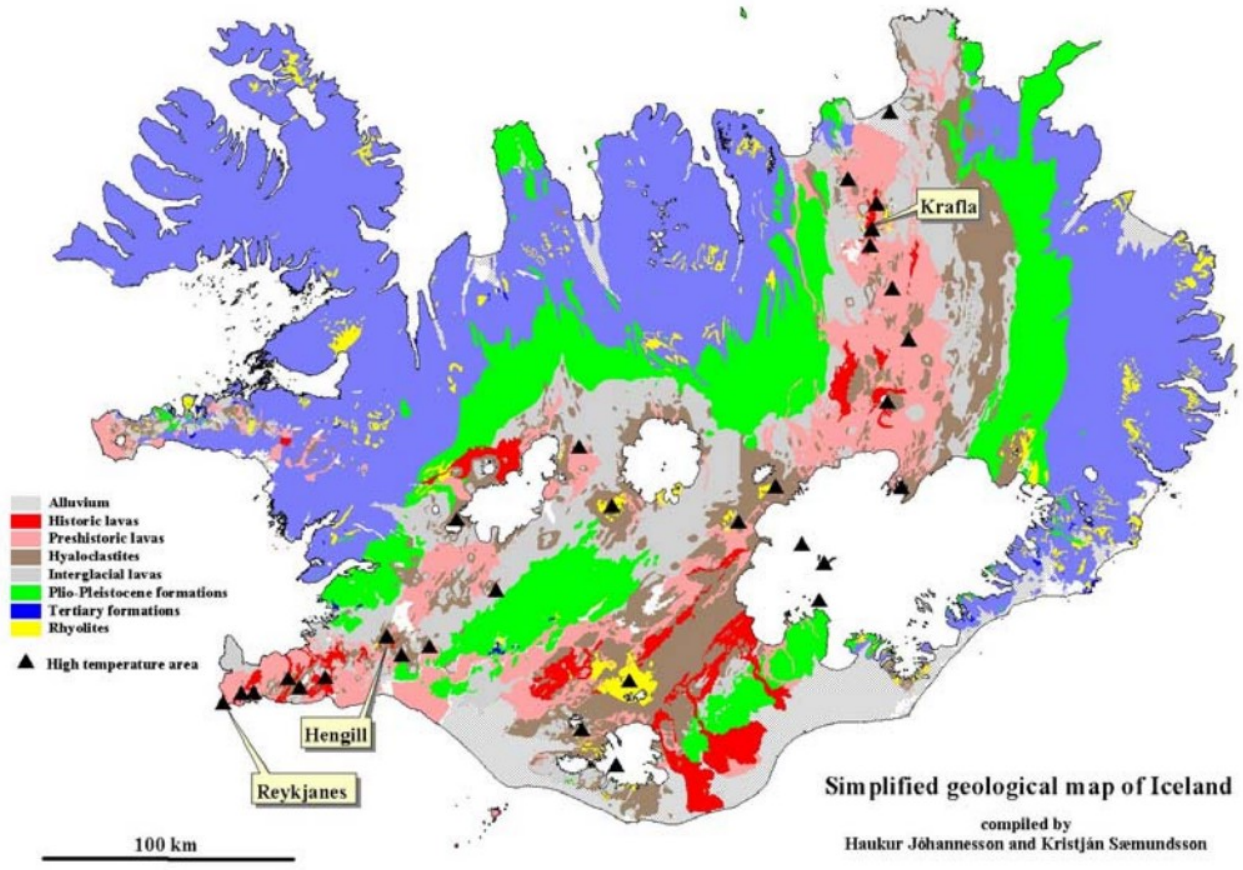

Figure 2.1: Geological map of Iceland showing the location of the Reykjanes, Nesjavellir and Krafla high-temperature geothermal systems (Fridleifsson et al., 2003).

2.2 Fluid Composition and Superctical Water Systems, Iceland

Due to the geological location of Iceland (over a rift in continental plates), the high concentration of volcanoes in the area is often an advantage in the generation of geothermal energy. The following sections aims to prompt the three main geothermal sites on Iceland regarding the exploitation of supercritical water systems and fluid composition. These three sites are Reykjanes, Hengill and Krafla, which display different stages in the tectonic development of the mid-ocean ridge (Fig. 2.1).

2.2.1 Reykjanes

The Reykjanes site represents an immature stage of rifting with a sheeted dike complex as a heat source and is a direct on-land continuation of the submerged Reykjanes ridge. At this site, 2 km deep geothermal wells produce fluids which are evolved seawater.

In obtaining supercritical conditions at this site, relatively deep drilling may be needed as

a consequence of two main factors. Firstly, the heat source is apparently rather deep-seated. Secondly, fluids at this depth are expected to be relatively saline as earlier fluids encountered at shallower depths are saline, and there is no suggested reason for this to change radically at greater depths at the site. Saline fluid requires higher pressure and temperature (and therefore greater depth) to obtain supercritical conditions compared to dilute fluid. (Fridleifsson et al., 2003)

Table 2.1: Composition of total fluid (mg/kg) in drillholes RN-8, RN-9 and of seawater at 35 ‰ salinity (Fridleifsson et al., 2003).

Well No	RN-8	RN-9	Seawater
Ref.Temp	275	290	-
SiO_2	553	647	6.4
Na	9488	9572	10800
K	1438	1419	392
Ca	1591	1632	411
Mg	1.28	0.91	1290
SO_4	21.8	14.1	2712
Cl	18732	18640	19800
F	0.17	0.14	1.3
CO_2	1005	1536	-
H_2S	27	45	-
H_2	0.08	0.13	-
CH_4	0.09	0.07	-
N_2	2.02	3.68	-

Fluids from geothermal systems on the sea-floor are probably the most representative for calculations of possible properties of fluids at supercritical conditions in this system, as the system is known to extend into the ocean and the fluid is modified seawater.

In Table 2.1, the chemical composition of the fluids from wells RN-8 and RN-9 are compared with the composition of seawater at 35 ‰. As expected at high temperatures, the most important deviations from seawater chemistry are the increase of calcium, silica and potassium in addition to depletion of magnesium and sulphate. Regarding gas concentrations, CO_2 show to be the major gas, and compared to fluid from many other geothermal areas, H_2S concentrations are relatively low. Due to the presence of a significant amount of N_2 concentration, it is suggested that flow from the surface contributes to the fluid. (Fridleifsson et al., 2003)

As a result of the chemistry composition presented in Table 2.1, the deep geothermal fluid in the Reykjanes geothermal field is most likely to originate from chloride waters as it matches well the description presented by Nicholson (1993) in addition to being mixed with seawater.

2.2.2 Hengill-Nesjavellir

At this site, the relatively young Hengill central volcano is the heat source for a geothermal reservoir in a graben recharged by meteoric water located in the Nesjavellir system.

Investigations indicate that the area located at the western part of the Hengill volcanic complex, associated with the youngest volcanic structure, is the most promising regarding obtaining supercritical conditions at a shallower depth than 5 km. As it was not possible to quench an aquifer system close to the bottom of well NJ-11 with cold water circulation, it is suggested an initial aquifer pressure above 220 bar with a temperature of at least 380 °C. This would lead to a supercritical fluid state if the fluid at the bottom of the aquifer is dilute of the type observed elsewhere in the system. The fluids in the system are not likely to be viscous, and thus, relatively little danger of serious utilization problems are expected at reaching supercritical conditions at Nesjavellir. (Fridleifsson et al., 2003) Table 2.2 presents the fluid composition of well NJ-16 along with analyses from some other Hengill boreholes.

Table 2.2: Chemical composition (mg/kg) of deep fluid in well NJ-16, Nesjavellir, well G-6, Olfusdalur, Hverageroi, well KhG-1, Hellisheidi and well OJ-1, Olkelduhals. Adapted from Fridleifsson et al. (2003).

Well No.	NJ-16	G-6	KhG-1	ÖJ-1	**Average**
Ref. Temp	290	210	270	198	242
Deep water					
SiO_2	718.5	337	538	337	482.6
Na	83.8	158	127	172	135.2
K	16.9	16.3	18.5	17.1	17.2
Ca	0.53	2.06	0.30	1.37	1.07
Mg	0.021	0	0.002	0.0062	0.0073
SO_4	12.3	30.2	16.7	33.6	23.2
Cl	10.2	166	7.4	170	88.4
F	0.78	0.93	1.11	0.79	0.90
CO_2	57.4	37.4	220	333	161.95
H_2S	0.72	0	0.0011	0.006	0.1818
O_2	0.01	0	0.003	-	0.004
CH_4	0.02	0	0.035	-	0.018
N_2	0.47	0.04	0.679	0.243	0.358
Deep steam					
CO_2	2510	2317	8136	-	4321
H_2S	1538	301	432	-	757
H_2	160	4.9	-4.4	-	53.5
O_2	1.1	2.0	1.2	-	1.4
CH_4	7.2	2.5	16.7	-	8.8
N_2	125	102	409	-	212

The fluid at Nesjavellir contains total dissolved solids in the range of 1000–1500 mg/kg and

is relatively dilute. In the temperature range of 270–290 °C the chemistry indicates equilibrium between water and rock. Initially, the water contained exceptionally low concentrations of chloride in addition to being rich in carbonate (Table 2.2). Due to increased utilization and the accompanying enthalpy changes, it has been observed a decreased dilute water presence, in addition to gradually increasing chloride levels. (Fridleifsson et al., 2003)

2.2.3 Krafla

Located within a caldera in an active, mature, central volcanic complex, developed above a magma chamber, rests the Krafla high-temperature geothermal field. At this site, evolved meteoric water with some addition of volcanic gases are produced.

As the Krafla geothermal field extends over a large area, it is convenient to divide the fluids from Krafla into several groups, according to chemical composition and geography. Ármannsson et al. (1987) divided the fluids from Krafla wells into seven groups: Leirbotnar upper zone (1), Leirbotnar lower zone N (2) and S (3), Hveragil (4), Suðurhlíðar (5), Hvíthólar upper (6) and lower parts (7). All these groups contain dilute waters close to neutral pH and the composition is probably affected by magmatic gas, especially in the areas closest to the magmatic inflow. A study carried out by Ármannsson (2001) attempted to simulate the geothermal fluid composition in the Krafla system by titrating local groundwater with Krafla rock. The study resulted in a suggestion that the geothermal fluid composition cannot be derived from rock and water alone, volcanic gas must have been added. (Fridleifsson et al., 2003)

In Table 2.3, seven selected samples from each of the seven groups are presented for deep water and deep steam composition, calculated by the use of the program WATCH (Arnórsson et al., 1982). In addition, their average values are presented, revealing a near neutral geothermal fluid with some addition of volcanic gases such as SO_4, H_2S and $CO_2 \cdot$ Furthermore, Stefánsson (2014) has carried out a study regarding fluid chemistry composition of aquifers found in the Krafla geothermal system. For this purpose, both the WATCH (Arnórsson et al., 1982) program and PHREEQC (Parkhurst et al., 1999) was used. A selected result is presented in Table A.1 in Appendix A.

Table 2.3: Deep water and deep steam composition (mg/kg) of selected Krafla well fluids and their average values. Adapted from Fridleifsson et al. (2003).

Group No.	1	2	3	4	**5**	6	7	Námafjall	
Well No.	KG-8	KG-26	KJ-13	KJ-20	KJ-14	KJ-22	KJ-21	BJ-12	**Average**
Ref. Temp (°C)	210	310	310	285	295	210	270	259	269
Deep water									
Ph	7.96	7.13	7.83	7.31	7.77	7.7	7.59	7.49	7.60
SiO_2	351.5	793.6	645.6	665.5	726	325.6	505.5	522.7	567
Na	179.5	357.6	165.4	153.2	165.8	116.7	138	120.6	174.6
K	21.08	81.46	26.42	36.05	34.02	11.43	25.02	20.75	32.03
Ca	1.58	28.93	3.16	0.8	0.55	2.32	0.61	0.3	4.78
Mg	0	0.077	0.005	0.004	0.008	0.009	0	0.01	0.014
SO_4	170.5	61.97	134.7	43.73	14.38	83.18	23.68	9.88	67.75
Cl	1.6	610.7	23.37	91.76	78.79	49.67	115.8	79.05	131.34
F	1.02	3.78	0.89	0.69	4.71	0.96	0.78	0.5	1.67
CO_2	94.64	367	397	676	497	52.96	114.6	31.11	278.79
H_2S	53	99.46	111	102.6	42.44	30.71	78.76	142.8	82.60
H_2	0	0.2	0.36	0.16	0	0	0.1	0.47	0.16
O_2	0.02	0.05	0.01	0.05	0	0	0	0.04	0.02
CH_4	0.03	0.01	0	0.01	0	0	0.01	0.03	0.01
N_2	0.43	0.83	0.14	0.54	0	0	0.12	0.22	0.29
Deep steam									
CO_2	4948	13486	11927	39818	19392	4639	7152	2314	12960
H_2S	581	1091	873	1627	411	587	1172	2481	1103
H_2	25.3	44.7	39.9	0	0	37.9	256	-	57.7
O_2	6	0.92	11.86	0	0	1.61	17.1	-	5.36
CH_4	112	2.5	0	6	0	0	7.5	21.4	18.7
N_2	1206	128	22.4	167	0	0	55.4	142	215.1

2.3 Iceland Deep Drilling Project

> The IDDP aims to improve the economics of geothermal resources, minimize the environmental impact of harnessing geothermal reservoirs, evaluate the volume of deep accessible geothermal resources, examine extraction of valuable minerals and metals, and support sustainable energy development in society
>
> Friðleifsson et al. (2014)

The Iceland Deep Drilling Project (IDDP), is a long-term program established in 2000 by a consortium of Icelandic power companies, the Icelandic government, and international partners aimed to investigate the potential of developing geothermal systems under supercritical conditions as a source of energy. In addition, it aims to "improve the economics of geothermal resources, minimize the environmental impact of harnessing geothermal reservoirs, evaluate the volume of deep accessible geothermal resources, examine extraction of valuable minerals and metals, and support sustainable energy development in society" Friðleifsson et al. (2014).

From 2008 to 2009, the drilling of the first deep IDDP well (IDDP-1) was attempted. IDDP-1 is situated at the Krafla geothermal system located in Northeastern Iceland with a geology characterized by an active central volcano containing a caldera and a magma chamber at 5–8 km depth (Ármannsson et al., 2014). The objective of the program was to reach a depth of 4500 m and temperatures and pressures above 450°C and 300 bars (Elders et al., 2014). These conditions of temperature and pressure are close to point F in the supercritical region presented in Figure 2.2, which coincide with the concept behind the Iceland Deep Drilling Project. A supercritical fluid is produced at point F, and the fluid would move up the well adiabatically along path F to G, in such a way that it transitions directly to superheated (but subcritical) steam at point G without intersecting the dew point curve that bound the high enthalpy side of the two-phase liquid-steam region. Path F to J represents the scenario of lower flow rates, causing conductive cooling. In this case, at point J, the fluid will be partition into a mixture of steam and liquid which could dissociate any present acids and result in potentially acidic and corrosive two-phase flow (Boden, 2016). IDDP-1 was aborted when the drill bit intersected 900°C hot rhyolitic magma (Fig. 2.3), at a depth of 2104 m (Zierenberg et al., 2013). However, the IDDP consortium decided to complete the well just above this point at 2072 m, allowing the examination and production from the >500°C contact zone of the intrusion. Resulting in a two-year flow test, involving a

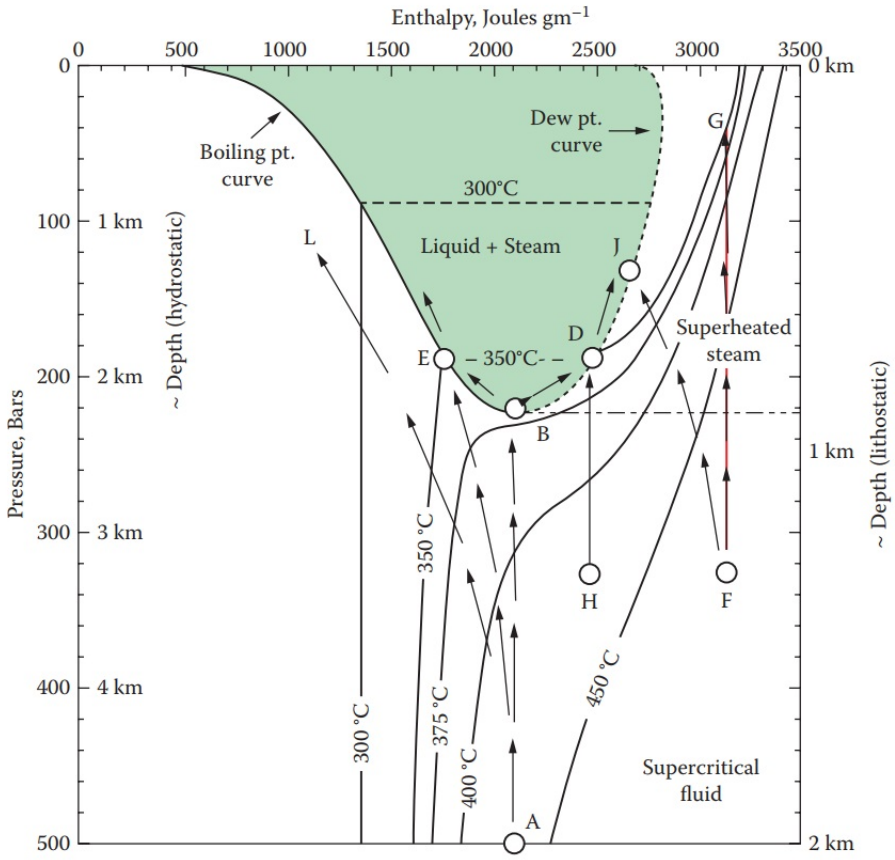

Figure 2.2: Pressure-enthalpy diagram showing sub- and supercritical conditions for pure water. The shaded green area show the conditions under which steam and liquid water co-exist is bounded on the left by the boiling point curve and to the right by the dew point curve. In addition, the depth scales marked at the left and right sides correspond to pressures in hydrothermal systems – respectively controlled by cold water hydrostatic conditions and by lithostatic load. The pressure-enthalpy diagram is inverted for the sake of relating it to geothermal fluid exploration. The arrows show various different cooling paths of ascending fluids; see text. (Boden, 2016)

nearby well that served as an injection well, producing superheated steam at 452°C and 140 bar with a production potential of up to 35 MWe (Elders et al., 2014). Unfortunately, corrosion on the well and its associated surface equipment from acid gases (HCl, H_2S and HF) along with silica scaling and erosion; ultimately resulted in the failure of the wellhead valve which led to the shut-in of the well. Even though the well did not achieve production from supercritical conditions as originally intended, and is not likely to do so, it has provided useful information on the composition of hot fluids in proximity to magma. (Einarsson et al., 2015)

The following phase of the Iceland Deep Drilling Project (IDDP-2) involved the deepening of an existing well (RN-15) from its original depth of 2507 m to a depth of 5 km, located in the Reykjanes geothermal field. On the 25th of January, 2017 the well was completed at a depth of 4659 m, recording a bottomhole temperature of 427°C with a fluid pressure of 340

bars (Friðleifsson and Elders, 2017). As such, the main drilling phase objective of the project; reaching supercritical conditions, has been achieved. Drill cores have been retrieved in addition to encountering several permeable zones below 3000 m.

Still, much remains to be done regarding the well. The current phase includes terms of geochemistry, downhole logging, future reservoir simulation and, in particular, flow testing. Flow tests are currently postponed due to loss of circulation from about 3000 m depth to the end of the drilling at 4659 m depth. (Friðleifsson and Elders, 2017)

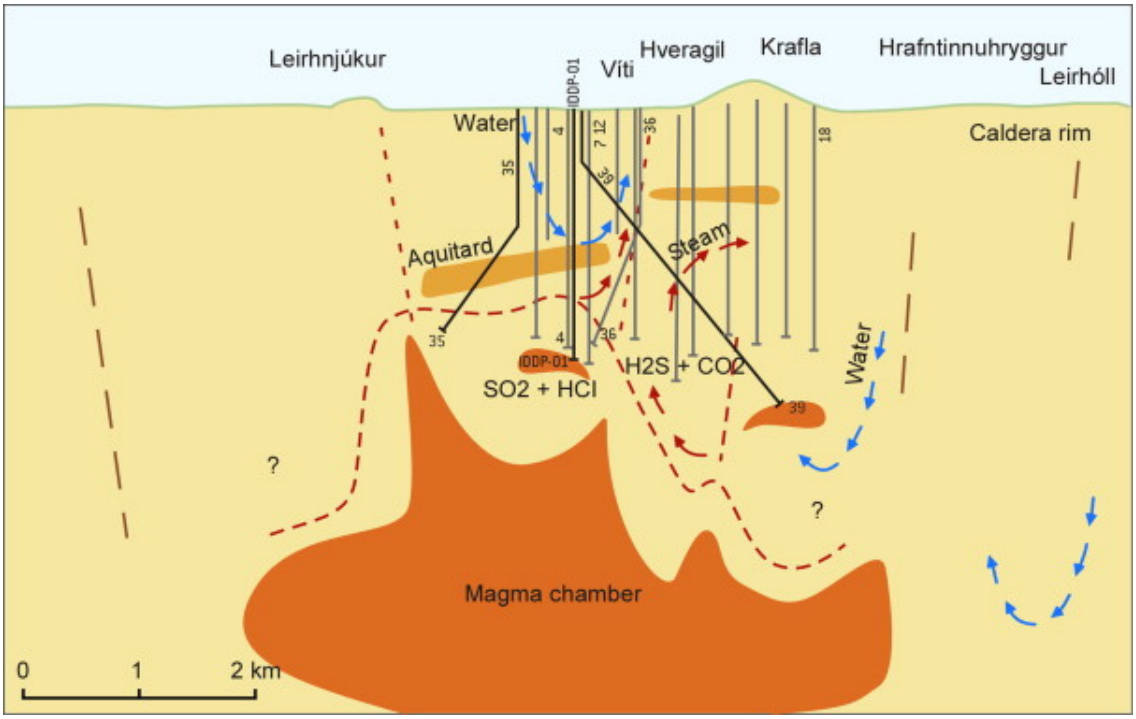

Figure 2.3: East-west cross-section showing a geologic model inferred for the Krafla geothermal field (Ármannsson et al., 2014).

2.3.1 IDDP-1 Chemistry

Ármannsson et al. (2014) has extracted and analyzed well samples from IDDP-1. Chemical composition from one of these samples extracted in January 2012, is presented in Table 2.4. Along with the main features of the chemical composition of dry steam from two earlier superheated wells, KG-12 and KJ-36. It was observed a seemingly trend towards lower condensed vapour pH values with discharged time and the pH is apparently controlled by the generation of H^+ ions from HCL and HF during condensation, modified by dissolution of iron and other metals from pipes. Cl concentrations ranged from 20 to 166 mg/kg in condensed samples of superheated steam, with Cl^- being the major anion which is likely derived from magmatic gas coming into contact with liquid water and forming hydrochloric

Table 2.4: Selected data from analysis of one sample from the IDDP-1 well (mg/kg), taken in January 2012. Along with the main features of the chemical composition (mg/kg) of the dry steam from two earlier superheated wells, KG-12 and KJ-36 (Ármannsson et al., 2014).

Well No.	IDDP-1 08.03.2012	KG-12 1979	KJ-36 2007
Temperature (°C)	440	176.5	-
Pressure (bar g)	138	7.9	9.0
$h_0(kJ/kg)$	3090	2776	2676
Condensate			
pH (°C)	2.44/22.7	3.48/19	3.30/21
Conductivity ($\mu S/cm$/°C)	977/25	290/25	-
B	2.2	0.46	-
SiO_2	6.2	28	-
TDS	70	81.2	-
Na	0.08	0.17	-
K	0.02	-	-
Mg	0.004	0.04	-
Ca	<0.1	0.43	-
F	8.45	0.24	0.24
Cl	89.6	112	400
SO_4	5.78	-	6.5
Gas			
CO_2	560	17,077	6463
H_2S	250	1127	3320
H_2	8.77	44.6	32.8
N_2	16.3	0	175
CH_4	0.27	6.7	2.7
Ar	0.53	-	3.6

acid. F concentrations in the condensed vapour samples were between 2.4 and 8.8 mg/kg, and F^- concentrations appeared to increase with discharged time, probably due to increasing temperature. Cl and F were apparently transported to the surface as molecular HCl and HF but formed an acid upon condensation at the surface and then attacked the steel in the surface equipment where it could be dealt with adequately. The sample was analyzed in March 2012 (Table 2.4) with a silica concentration of 6.2 mg/kg. In some condensate samples from 2011, it varied from 1.5 to 55 mg/kg. Such silica concentrations are low for geothermal steam condensates. It has been observed that the SiO_2 concentration in condensates from IDDP-1 essentially increases with discharge time and increasing wellhead temperature. Further, it is suggested that the explanation for the high concentration of silica found in the condensate is due to the volatility of silica, proposing that it would decrease sharply with lower pressure. The chemical composition and analytical methods are further discussed by Ármannsson et al. (2014) with the overall conclusion from the report being that the chemistry of the superheated

steam appeared manageable and that this fluid could be suitable for use in power production if due precautions were taken. However, the choice of material for surface equipment proved problematic as even the highest quality stainless steels are prone to cracking in the IDDP-1 steam, and titanium which is resistant to this type of composition cannot withstand temperatures much higher than 340 °C. (Ármannsson et al., 2014)

Moreover, the superheated steam contained acid gas which proved to be highly corrosive when condensing, making it unsuitable for utilization without scrubbing. Material tests and scrubbing experiments at the well has been carried out by Hauksson et al. (2014).

2.3.2 IDDP-2 Chemistry

Even though there are no current data regarding the chemistry of the IDDP-2 reservoir, Fridriksson et al. (2015) has carried out a study anticipating the chemical composition of the fluid that may be encountered in the well. The study estimated a well temperature between 380–550 °C and further explored the chemical implications of three potential deep temperature scenarios (Fig. 2.4); low (382 °C), intermediate (441°C), and high (550°C).

The study imposed these scenarios on a phase diagram for H_2O constructed in terms of enthalpy (0 to 3500 kJ/kg) and pressure (0 to 500 bar) shown in Figure 2.5.

Figure 2.5 contain superimposed concentration contours of quartz solubility over the entire pressure-enthalpy range (Fournier and Potter, 1982). Also shown in the diagram are phase relations in a NaCl-H_2O system with 3.5% NaCl, constrained using the sowat_ptx.exe code (Driesner, 2007; Driesner and Heinrich, 2007). In computing the properties of H_2O at elevated pressure and enthalpy (temperature), a software consistent with the IAPWS-IF97 formulation for thermodynamic properties of H_2O, Water97_v12.xla (Spang, 2002) was used.

Figure 2.5 shows how the silica concentration controlled by quartz solubility varies with enthalpy and pressure

i) At lower enthalpies, from 0 to ~ 1500 kJ/kg, quartz solubility is irrespective of pressure.

ii) From ~ 1500 kJ/kg to ~ 2500 kJ/kg, quartz solubility decreases as a result of decreasing density of the fluid phase.

iii) At high enthalpies, above ~ 2500 kJ/kg, quartz solubility is more sensetive to pressure than enthalpy.

The figure also distinguishes between three phases. Up to ~ 2450 kJ/kg the 3.5% NaCl system is a single liquid phase. Further, from ~ 2450 kJ/kg to about 2800–3400 kJ/kg, a wedge where two fluid phases, dilute (low density), and high NaCl brine (high density) fluid, coexist. Above 2800–3400 kJ/kg the system consist of solid NaCl (halite) and vapor.

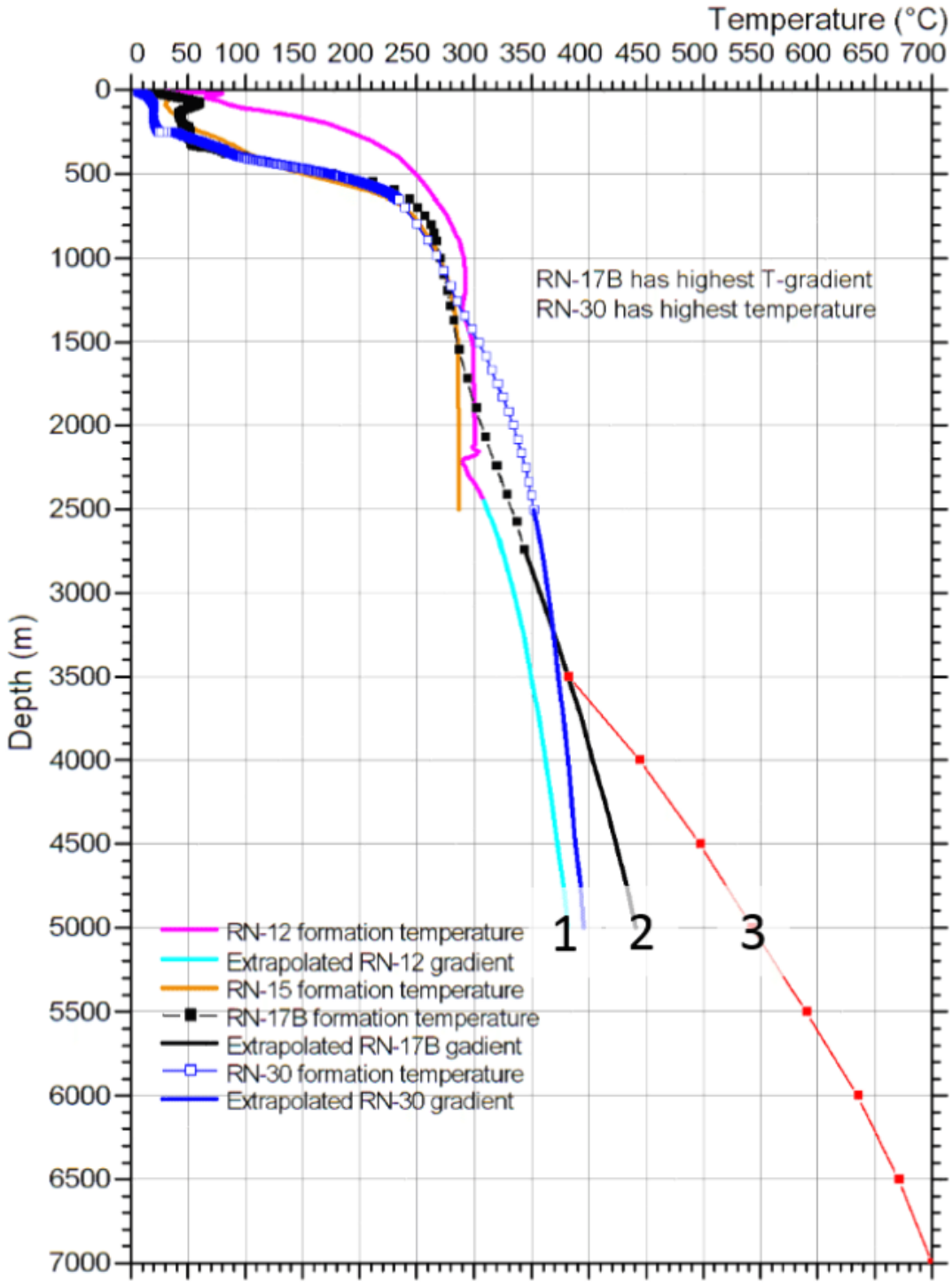

Figure 2.4: Temperature profiles in selected wells in Reykjanes.The numbers 1, 2, and 3 refer to the minimum, intermediate and maximum temperature estimate at 5 km, which were used to constrain the expected chemical scenarios (Fridriksson et al., 2015). Further explanation is carried out by Fridriksson et al. (2015).

Inspection of Figure 2.5 reveals that the three temperature scenarios described previously are located in the three different fields of the NaCl-H_2O phase diagram.

These scenarios are following, from a chemical standpoint, characterized from most to least favourable.

i) Low-temperature scenario: Assuming a temperature of 382°C (1830 kJ/kg) at 5 km depth is located in the single liquid field. Will produce similar fluids as currently are produced from the Reykjanes field, and thus, regarded as the most favourable and manageable scenario in terms of chemical composition. Still, the fluid will contain additional silica concentration and potential for metal sulphide scaling, compared to similar fluids produced in the Reykjanes field.

ii) High-temperature scenario: Superheated steam with a complicated fluid of high silica concentration in the steam at 550°C (3256 kJ/kg) at 5 km depth, located in the vapor-halite field. In this case, the well is expected to produced a fluid with high HCl content and regraded as the seconds most favourable scenario.

iii) Intermediate-temperature scenario: Assuming a temperature of 441°C (2740 kJ/kg) at 5 km depth is located in the brine-dilute fluid field. Regarded as the least favourable scenario as either two fluids, low salinity - low density fluid and high salinity - high density brine, may coexist or only superheated steam at 440 °C (Fig. 2.5). Extraction of this geothermal fluid will presumably lead to acute corrosion problems in the well, as the condensate which forms during decompression will be extremely acidic as HCl. (Friðleifsson, 2017).

As stated in the introduction to this section, the completion of the IDDP-2 well was achieved in 2017, while the study regarding quartz solubility was attained by Fridriksson et al. (2015) in 2015. Thus, some further approximations regarding the reservoir may be achieved. The bottomhole temperature was recorded to a temperature of 427°C with a fluid pressure of 340 bars (Friðleifsson and Elders, 2017). For pure water at 427 °C and 340 bars, the enthalpy is 2400 kJ/kg, which reveals that the silica concentration of the dilute phase will be ~ 400 mg/kg, illustrated with point 4 in Figure 2.5. These conditions are closest to the intermediate temperature scenario (point 2), but still, within the single liquid phase. Even though uncertainties, such as actual temperature in flowing conditions, may result in the least favourable scenario (from a chemical standpoint), the two liquid brine-diluted field, this deduction reveals that it is probably within the more manageable single liquid phase.

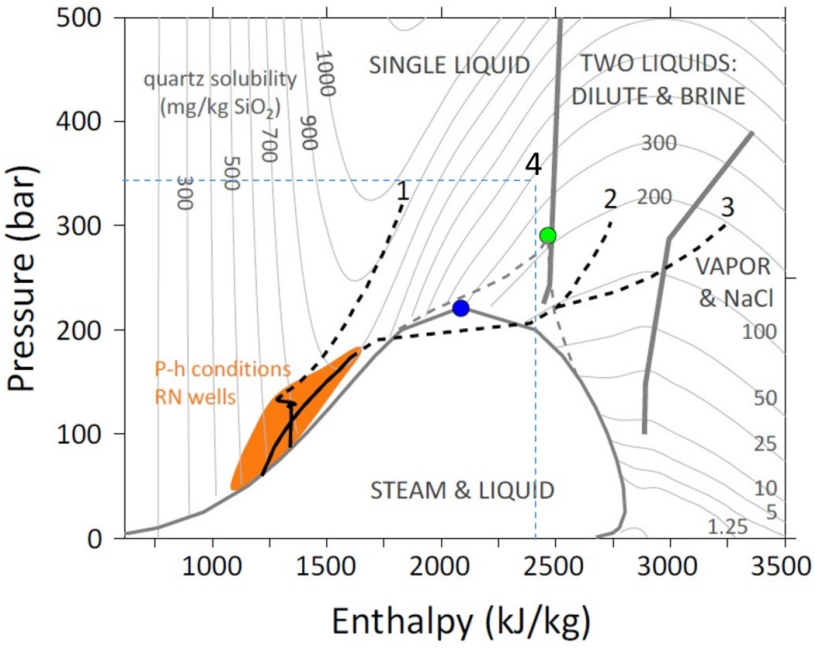

Figure 2.5: Phase diagram for H_2O in terms of pressure and enthalpy with superimposed quartz solubility (gray contour lines) and phase boundaries in a 3.5% NaCl–H_2O system (single liquid, dilute fluid/brine, and vapor/solid NaCl). The critical points for pure water and seawater are shown by blue and green symbols, respectively. The P-h conditions of the current Reykjanes production wells is indicated by an orange field. The hatched curves indicate the extrapolated temperature curves shown on Figure 2.4, representing the three temperature scenarios. (Fridriksson et al., 2015). In addition, point 4 shows approximation on IDDP-2 with subsequently obtained values regarding temperature and pressure of the IDDP-2 reservoir (Friðleifsson and Elders, 2017)

2.4 Discussion & Chemistry Variation Ranges

The composition of geothermal fluids vary significantly due to differences in temperature, gas content, rock type, heat source, permeability, fluid source or mixing (e.g. salt water) and age of the hydrothermal system. However, this section aims to develop some guidelines for the chemistry found in geothermal wells in Iceland based on previously presented data. This includes Tables 2.1–2.4. Table 2.5 includes the fluid composition of some selected wells from Nesjaviller and Krafla geothermal systems as their data is comparable. In the same table, maximum, minimum and average values are presented. It should be emphasized that the average column in Table 2.5 is not a representative general chemistry for Iceland, as such is not feasible due to the variations stated previously. It would be interesting to compare the different geothermal sites on Iceland in one table, including Reykjanes, IDDP and other deep geothermal wells situated elsewhere. However, this proves difficult as methods for determining and presenting chemical compositions are inconsistent. Still, some discussion regarding minimum, maximum and average values in Table 2.5 should prove interesting. The fluid composition for

the case study is presented in Table 2.6 which is derived from the different geothermal sites presented previously. In such, the following discussion also applies to the case study fluid composition (Table 2.6). The chemical compounds of greatest interest in this study are silica, calcite, carbon dioxide, sodium, sulphide and chloride.

In geothermal systems, silica and calcite equilibria are particularly important as they govern the amount of SiO_2 and Ca in solution, which are two of the main causes for scaling in wells.

Silica (SiO_2) concentration in a geothermal fluid is usually <700 mg/kg, typically 100-300 mg/kg, and controlled by the solubility of the different silica minerals. The compound can occur in various forms or polymorphs such as quartz, chalcedony, cristobalite, opal and amorphous silica, each having slight variations in solubility. Quartz and amorphous are the most important, as they determine the dissolution and precipitation of silica. However, chalcedony may prove important in some systems. (Nicholson, 1993) Silica concentrations in Iceland are thus generally within the usual values (with exception of well KG-26), but above average typically values (Table 2.3). Another exception is the IDDP-1 well. A sample from this well from March 2012 had an unusual silica concentration of 6.2 mg/kg (Table 2.4). It is therefore evident that the silica concentrations vary significantly within Iceland and site-specific analysis should be attained to determine the resulting prevention methods.

Calcite solubility is increased by increasing CO_2 partial pressure, decreasing temperature and increasing salinity. Upon boiling, carbon dioxide is lost to the steam phase, increasing the pH of the solution, resulting in a supersaturation and precipitation of calcite. Calcite deposition is thus most intense around the boiling zone and can result in serious scaling problem if boiling occurs in wells during exploitation of a geothermal resource (Nicholson, 1993). Calcium which is present in the chemical compound of calcite varies greatly in the geothermal wells of Iceland, even with a factor of almost 1:100 between wells KhG-1 and KG-26 (Table 2.5).

Carbon dioxide (CO_2) ranges between 2.3–45.2 g/kg of fluid from major geothermal fields and is the most abundant gas in geothermal systems, both by volume and weight. The influence of carbon dioxide on the overall chemistry and hydrology of a geothermal system should not be under-estimated. Water chemistry, density and pH, boiling point-depth relationships and the deposition of secondary minerals and scale are all controlled to some degree by the concentration of carbon dioxide. (Nicholson, 1993) As may be observed, the carbon dioxide concentrations in these wells are within the common range (Table 2.5).

Sodium, sulphide and chloride presence in geothermal steam may result in severe corrosion problems, especially in steam turbine components. Their effect and corresponding challenges are further discussed by (Ommedal, 2017). Regarding their presence in the geothermal wells presented previously, the Reykjanes field proves most difficult regarding these issues with an extensive amount of chloride and sodium (Table 2.1). Sulphide concentrations are of most significant presence in the Krafla geothermal field (Table 2.3).

The Icelandic crust is created in the on land portion of the Mid-Atlantic Ridge. Studies regarding wave speed in the crust of Iceland suggest closer similarities to wave speeds found in the oceanic crust than in the continental crust (Pálmason, 1971; Bjarnason et al., 1993). Which further suggest that the chemical composition of the Icelandic crust is similar to the chemical composition of basaltic type, certainly observed in the surface geology (Fridleifsson et al., 2003). Thus, the chemical composition of geothermal fluids in Iceland may vary compared to geothermal fluids found on the continental crust (mostly granite rock) as a result of differences in rock type. In addition, several of the geothermal fields in Iceland contain geothermal fluid which is mixed with seawater (e.g. Reykjanes), resulting in an extensive amount of chloride and sodium compounds. It is thus evident that the geothermal fields in Iceland contain characteristics which are comparable to those found beneath the ocean. Experiences from geothermal energy utilization on Iceland could thus prove valuable for geothermal energy utilization from the oceanic crust.

Table 2.5: Comparison of a selected set of data (mg/kg) from deep geothermal fluids on Iceland.

Well	NJ-16	KhG-1	KG-26	KJ-13	**Minimum**	**Maximum**	**Average**
Temp (°C)	290	270	310	310	270	310	295
Deep water							
SiO_2	718.5	538	793.6	645.6	538	793.6	673.9
Na	83.8	127	357.6	165.4	83.8	357.6	183.5
K	16.9	18.5	81.46	26.42	16.9	81.46	35.82
Ca	0.53	0.3	28.93	3.16	0.3	28.93	8.23
Mg	0.021	0.002	0.077	0.005	0.002	0.077	0.026
SO_4	12.3	16.7	61.97	134.7	12.3	134.7	56.4
Cl	10.2	7.4	610.7	27.37	7.4	610.7	163.92
F	0.78	1.11	3.78	0.89	0.78	3.78	1.64
CO_2	57.4	2.2	367	396	2.2	396	205.7
H_2S	0.72	56	99.46	111	0.72	111	66.80
H_2	0.72	0.011	0.2	0.36	0.011	0.72	0.323
O_2	0.01	0.003	0.05	0.01	0.01	0.05	0.018
CH_4	0.02	0.035	0.01	0	0	0.035	0.016
N_2	0.47	0.679	0.83	0.14	0.14	0.83	0.530
Deep steam							
CO_2	2510	8136	13486	11927	2510	13486	9015
H_2S	1538	432	1091	873	432	1538	984
H_2	160	4.4	44.7	39.9	4.4	160	62.3
O_2	1.1	1.2	0.92	11.86	0.92	11.86	3.77
CH_4	7.2	16.7	2.5	0	0	16.7	6.6
N_2	125	409	128	22.4	22.4	409	171.1

2.5 Summary - Well and Fluid Properties of Case Study

As no specific data on fluid chemistry composition in supercritical geothermal aquifers could be acquired with the available resources during this study, it was decided along with the supervisors of this thesis to use the most significant values from the different chemical compositions presented previously. By analyzing these extreme values, their contribution and effect should be magnified. In Table 2.6 the total fluid chemistry of the case study is presented along with the respective tables and wells which the different elements are extracted from. The temperature and pressure of the reservoir in the case study are set to 500 °C and 230 bar, respectively. These

conditions are set of interest to obtain similar (not exact) temperature and pressure conditions at the discharge of the well as found in IDDP-2. The conditions regarding temperature and pressure for the case study (Table 2.6), would result in a silica concentration of ~ 100 mg/kg if Figure 2.5 was representative for this composition. However, the silica concentration for this case study is set to 250 mg/kg as silica precipitation and scaling are of important concern in geothermal energy utilization. Pipe parameters for the case study along with calculations regarding temperature, enthalpy and pressure variations during extraction of the geothermal fluid from the reservoir to the surface is presented in Chapter 3.

Table 2.6: Total fluid composition (mg/kg) of Case study bases on chemistry variations on Iceland.

Element	**Case study**	**Retrieved from**	**Location/Comment**
Temperature (°C)	500	Set for Case	See text
Pressure (bar)	230	Set for Case	See text
SiO_2	250	Set for Case	See text
B	2.2	Table 2.4	IDDP-1
Na	9572	Table 2.1	RN-9
K	1438	Table 2.1	RN-8
Ca	1632	Table 2.1	RN-9
Mg	1.28	Table 2.1	RN-8
CO_2	17077	Table 2.4	KG-12 1979
H_2S	1538	Table 2.2	NJ-16
SO_4	170.5	Table 2.3	KG-8
F	8.45	Table 2.4	IDDP-1
Cl	18732	Table 2.1	RN-8
H_2	160.72	Table 2.5	NJ-16

Developing sustainable geothermal power plants has many challenges, including challenges related to chemistry. Each plant design is characterized by the fluid chemistry in the geothermal reservoir supplying the plant, and thus, these characteristics can magnify the challenges related to the chemistry of the plant. By addressing these chemistry challenges, their occurrence can be prevented throughout the design process, avoiding unwanted forced shutdowns and unplanned maintenance, leading to an improved power plant performance. In addition, the chemical composition of the geothermal fluid and the operational conditions vary for most geothermal power plants. Therefore, scaling and corrosion are often site-specific with no unique solution. (Nicholson, 1993)

As described in the introduction to this paper, an appropriate tool for calculating chemical equilibrium at these conditions (high temperature and high pressure) could not be attained during this study. As such, the effects of the fluid composition in Table 2.6 on the geothermal

power plant could not be quantified. A discussion regarding the most important chemical compounds and their variation ranges for deep geothermal waters in Iceland is already presented in Section 2.4, and as the fluid composition for the case study as presented in Table 2.6 is a result of these ranges, the extent of the fluid compounds is not further discussed. The case study fluid composition is a result of the most extreme values from the deep geothermal wells analyzed in this chapter. In such, an analysis of this composition should prove fruitful and interesting when an appropriate tool for calculating chemical equilibrium at these temperatures and pressures is obtained. Furthermore, chemistry challenges in geothermal power production as a result of fluid chemistry composition is already discussed in Ommedal (2017), and thus not repeated here. Still, the fluid pressure and temperature from Table 2.6 is used as the case study conditions for the reservoir, which is further evaluated for electric power production in the remaining chapters.

Chapter 3

Extraction of Geothermal Fluid

The flow rate from, and the performance of a geothermal reservoir are functions of several parameters, such as the volume of the reservoir, type of fluid in the aquifer, the permeability of rock, the rate of discharge (if any) and design of the drilled well and piping.

Characteristics of temperature, pressure and enthalpy are important in developing technologies for utilizing high-temperature geothermal resources for power generation. For this purpose, TEPP (Temperature, Enthalpy & Pressure Program) has been developed. With initial conditions of the reservoir in addition to pipeline parameters, pressure, temperature and enthalpy variations during the extraction of high-temperature geothermal fluids are calculated. TEPP is developed in MATLAB, a multi-paradigm numerical computing environment. The purpose of TEPP is to provide a fast estimate for decision makers. As the developer of TEPP wishes to promote geothermal utilization, the program is provided as an open-source software. Due to the simplicity of the program, several conditions of the reservoir and pipeline can be examined in a very short time. However, it should be emphasized that this only gives a rough estimate, and should be used to give a first indication of if the characteristics of the reservoir are worth proceeding on.

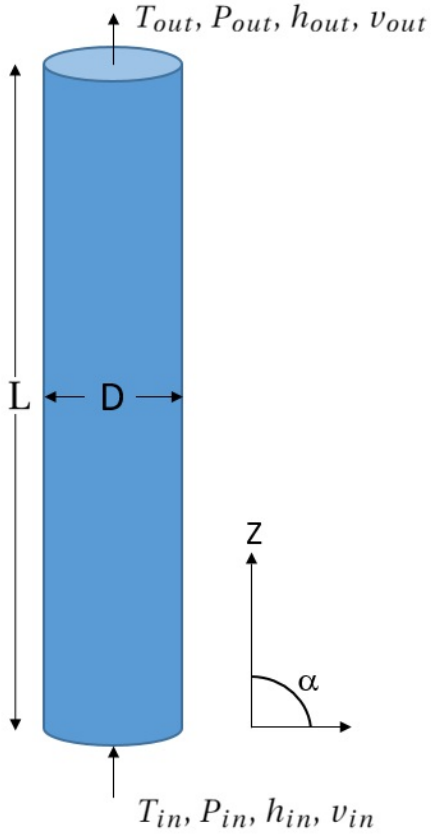

Figure 3.1: Schematic for production pipe for geothermal fluid extraction (not to scale).

As geothermal fluids at high temperature and high pressure mainly contain steam, TEPP presupposes steam as the working fluid and TEPP is limited to the region above the saturated vapour line.

Beyond the critical point (T>373.95 °C, P>22.064 MPa) in the liquid-vapuor space, water is supercritical, where physical properties, such as gas-like or liquid-like behaviour, vary in response to changing temperature, pressure and density and the normal distinction between gas and liquid has disappeared. Due to dramatic variations of water properties near the pseudocritical temperature, heat transfer characteristics are substantially different from those at subcritical pressures. (Bazargan et al., 2005; Pioro and Mokry, 2011) The complexity of supercritical water was determined beyond this study, and the fluid is assumed superheated and obeys the ideal gas law with compressibility set to unity. The consequence of these simplifications is further discussed in Section 3.5. These simplifications are also carried out to obtain a simplified and fast estimation, as previously presented in the purpose of TEPP.

As the purpose of this study is to examine the potential of supercritical geothermal exploitation, a case study containing the properties of a generic supercritical well regarding pressure and temperature previously defined in Section 2.5, is considered. Production pipe parameters are chosen according to the aim of IDDP-2. In addition, losses assumed to have a minor contribution to the system are neglected while still aiming to examine a case study which is realistic for geothermal exploitation of supercritical water. A further presentation regarding the chosen pipe parameters are presented in Section 3.3.1 and a further discussion regarding the accuracy of this approach is presented in Section 3.5.

The content in this chapter is arranged as follows. First, theoretical background for the development of TEPP is derived. Secondly, the two currently developed versions of TEPP are presented, in addition to discussing the results of these version carried out for the chosen case study conditions available in Table 3.2. Finally, suggestions for further development of the program is presented before discussing the validity of the program.

3.1 Development of TEPP - Extraction of Geothermal Fluid - Theory

This section contains the derivation of the equations regarding pressure, temperature and enthalpy implemented in TEEP. Figure 3.1 shows the schematics for the production pipe section.

3.1.1 Pressure

Starting by introducing the total pressure gradient for steady-state flow in a vertical tube

$$\left(\frac{dP}{dz}\right)_{total} = \left(\frac{dP}{dz}\right)_f + \left(\frac{dP}{dz}\right)_s + \left(\frac{dP}{dz}\right)_a \tag{3.1}$$

Where the frictional, static head and accelerational pressure gradient are defined as

$$-\left(\frac{dP}{dz}\right)_f = \lambda \cdot \frac{1}{D} \cdot \frac{1}{2} \cdot \rho \cdot v^2 \tag{3.2}$$

$$-\left(\frac{dP}{dz}\right)_s = \rho \cdot g \tag{3.3}$$

$$-\left(\frac{dP}{dz}\right)_a = \frac{d}{dz}\left(\frac{1}{2}\rho \cdot v^2\right) \tag{3.4}$$

The acceleration pressure gradient may, for convenience, be reformulated as

$$-\left(\frac{dP}{dz}\right)_a = \bar{\lambda} \cdot \frac{1}{D} \cdot \frac{1}{2} \cdot \rho v^2 \quad \text{where} \quad \bar{\lambda} = 2 \cdot \frac{D}{v} \cdot \frac{dv}{dz} \tag{3.5}$$

Combining these into Eq.3.1, we obtain

$$\left(\frac{dP}{dz}\right)_{total} = -(\lambda + \bar{\lambda}) \cdot \frac{1}{2D} \cdot \rho v^2 - \rho g \tag{3.6}$$

For a low-velocity compressible flow assuming that the temperature of the steam changes very slightly as it flows through an insulated pipe section, it is acceptable to treat it as isothermal in calculating the pressure variation in the pipe (Toth, 2017). For an isothermal flow

$$\frac{P_0}{\rho_0} = \frac{P}{\rho} = const. \tag{3.7}$$

And

$$\rho_0 v_0 = \rho v = const. \tag{3.8}$$

Combining these equations we obtain

$$Pv = const. \tag{3.9}$$

Further differentiating

$$\frac{dv}{v} = \frac{dP}{P} \tag{3.10}$$

Now, by combining Eq.3.10 and Eq.3.5, the additional friction factor can be written as

$$\bar{\lambda} = \frac{2D}{P} \cdot \frac{dP}{dz} \tag{3.11}$$

And the Darcy friction factor, λ, expressed as

$$\lambda = \frac{2D}{\rho v^2} \cdot \frac{dP}{dz} \tag{3.12}$$

The ratio of the two friction factors is therefore

$$\frac{\bar{\lambda}}{\lambda} = \frac{\rho v^2}{P} = \frac{v^2}{RT} \tag{3.13}$$

For supercritical steam at 550 °C and 9 m/s, this ratio is $1.9869 \cdot 10^{-4}$. Thus, for a low-velocity compressible flow, e.g. supercritical steam pipelines, the effect of expansion represented by $\bar{\lambda}$ may be neglected. Thus, Eq.3.6 is obtained in a simpler form

$$\left(\frac{dP}{dz}\right)_{total} = -\lambda \cdot \frac{1}{2D} \cdot \rho v^2 - \rho g \tag{3.14}$$

Now, by the use of Eq.3.7, Eq.3.8 and replacing ρ_0, P_0, v_0 by the inlet flow variables ρ_1, P_1, v_1, we obtain

$$\frac{dP}{dz} = -\lambda \cdot \frac{1}{2D} \cdot \frac{P_1 \rho_1 v_1^2}{P} - \frac{P \rho_1 g}{P_1} \tag{3.15}$$

Finally, to account for inclined pipe sections, dz is substituted with dL and $g_L = g * sin(\alpha)$ (Fig.3.2)

$$\frac{dP}{dL} = -\lambda \cdot \frac{1}{2D} \cdot \frac{P_1 \rho_1}{P} v_1^2 - P \cdot \frac{\rho_1}{P_1} \cdot g sin\alpha \tag{3.16}$$

By the use of the forward Euler method and the first order differential equation (Eq.3.16) along with the boundary conditions of the reservoir, the pressure loss during extraction of the geothermal fluid can be calculated

$$P_{n+1} = P_n + dL(-\lambda \cdot \frac{1}{2D} \cdot \frac{P_1 \rho_1 v_1^2}{P_n} - P_n \cdot \frac{\rho_1}{P_1} \cdot g sin\alpha) \tag{3.17}$$

Where ρ_1, P_1, v_1 are the states found in the reservoir.

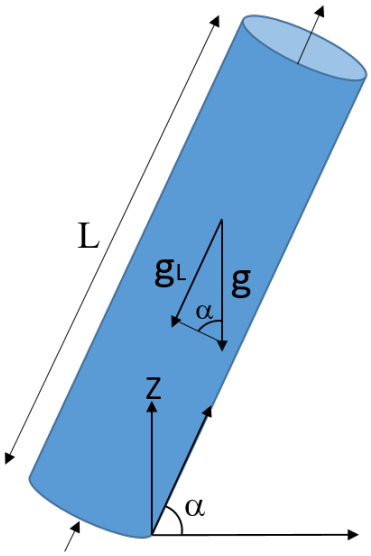

Figure 3.2: Sketch of angled pipe section with gravity vectors to clarify the derivation of Eq.3.16.

3.1.2 Enthalpy and Temperature

The main reason for developing supercritical water systems, compared to subcritical or conventional hydrothermal systems, is that supercritical water systems have much higher enthalpy and mass transfer abilities. The detailed explanation of these abilities are already discussed in Ommedal (2017), and thus not repeated in this paper. In deriving the pressure, the flow in the pipe during extraction was assumed isothermal (Toth, 2017). However, enthalpy is both a function of pressure and temperature, and thus, in calculating enthalpy during extraction the pipe is not assumed isothermal. An equation for calculating the temperature change due to

heat transfer with the surroundings of the pipe is developed. This is obtained by first calculating the enthalpy variation and further using X Steam to calculate the corresponding temperature as a function of pressure and enthalpy. X Steam for MATLAB, programmed as a matlab.m file, is an implementation of the IAPWS IF97 standard formulation. It provides accurate data for water and steam and mixtures of water and steam properties from 0–1000 bar and from 0–2000 °C (Holmgren, 2006).

Starting with the first law of thermodynamics, where $\dot{Q}$ is denoted as heat transfer rate added to the system and work rate denoted as work rate done by the system

$$\dot{Q} - \dot{W} = \dot{m}\left[h + \frac{1}{2}v^2 - gz\right]_{in}^{out} \tag{3.18}$$

The work performed by the system is basically the change in potential energy from the bottom of the well to the top of the well. In addition, there is a small contribution from the expansion of the fluid from the pressure at the bottom of the well to the top of the well. However, this small contribution is neglected and the work is assumed as $\dot{W} = -\dot{m}g(z_{out} - z_{in})$. Furthermore, the minus sign regarding the potential energy change in Eq.3.18 is due to the reference system in Figure.3.1. The heat transfer rate, $\dot{Q}$, is defined into the system even though heat will most likely leave the system due to the greater fluid temperature compared to the surrounded rock. However, this is accounted for in defining the heat transfer rate in Eq.3.20. By rearranging Eq.3.18, we obtain

$$h_{out} = h_{in} - \frac{1}{2}(v_{out}^2 - v_{in}^2) + \frac{\dot{Q}}{\dot{m}} \tag{3.19}$$

Where

$$\dot{Q} = UA_{ht}(T_\infty - T) \quad and \quad A_{ht} = \pi DL \tag{3.20}$$

T_∞ is the temperature in the surrounding rock and T is the temperature of the fluid in the pipe. Further assuming

1. The overall heat transfer coefficient is in the order of 1 (i.e. U=1) (Næss, 2018).

2. The contribution to change in enthalpy due the kinetic energy change is neglected.

   Considering an example with a production diameter of 0.2286 m with a mass flow rate of 50 kg/s, with inlet temperature and pressure of 550°C and 250 bar, respectively, the inlet density is 78.5 kg/m^3. For outlet conditions at 500 °C and 190 bar, the density is 63.1 kg/m^3 (Schmidt, 1969). Mass conservation leads to the following values for the inlet and outlet velocities

$$v_{in} = 18.4\frac{m}{s} \quad and \quad v_{out} = 22.92\frac{m}{s} \tag{3.21}$$

Assuming that the average temperature in the pipe is 525 °C and the surrounding rock temperature is 75 °C. The ratio of the change in kinetic energy to the change of heat energy for a 5000 m long vertical pipe with the stated conditions is

$$\frac{\frac{1}{2}(v_{out}^2 - v_{in}^2)}{\dot{Q}/\dot{m}} = \frac{\frac{1}{2}(v_{out}^2 - v_{in}^2)}{\frac{UA_{ht}(T_\infty - T)}{\dot{m}}} = 2.889 \cdot 10^{-3} \tag{3.22}$$

Thus, the contribution to enthalpy change due to change in kinetic energy is neglected.

Applying these assumption, the following equation for the enthalpy is obtained

$$h_{out} = h_{in} + \frac{\dot{Q}}{\dot{m}} \tag{3.23}$$

When enthalpy and pressure at a specific location are calculated in the integration of TEPP, the temperature is found by the use of X Steam, introduced at the beginning of this section.

3.1.3 Darcy friction factor

In calculating the Darcy friction factor, the Haaland equation is used as the flow is assumed turbulent due to the low viscosity of water at high temperatures. Haaland (1983) developed the equation

$$\frac{1}{\sqrt{\lambda}} = -1.8 log\left[\left(\frac{\epsilon/D}{3.7}\right)^{1.11} + \frac{6.9}{Re}\right] \quad \text{where} \quad Re = \frac{\rho v D}{\mu} \tag{3.24}$$

In the Haaland equation, there is no need to iterate the Darcy friction factor and it is assumed constant along the pipe. The accuracy of the Darcy friction factor solved from this equation is claimed to be within ± 2%, for Reynolds number greater than 3000 (Yunus and Cimbala, 2010), and thus, TEPP is limited to Reynolds numbers above 3000.

3.2 TEPP Versions - Extraction of Geothermal Fluids - Method

Two versions of TEPP has been developed, including a basic version (v1.0) and a modified version for alternating mass flow rates (v2.0).

3.2.1 TEPP (v1.0) - Basic version

The input variables required for calculating enthalpy, pressure and temperature variations in TEPP (v1.0) are presented in Table 3.1. In addition, the hydrostatic and friction contribution to pressure loss is calculated. During the calculations, all the output variables are stored in vectors, making it possible for detailed investigations. Increasing the number of integrations leads to more time-consuming calculations, but gives a better approximation, especially if pipe parameters differs along the pipe section. The flow chart for TEPP (v1.0) is available in Figure.3.3 and the MATLAB script for TEPP (v1.0) is available in Appendix B.1. The method is further demonstrated in the examination of geothermal extraction for the case study in Section 3.3.2.

Table 3.1: Input variables and resulting output data in the basic version of TEPP (v1.0).

Input	**Output**
Reservoir Temperature, T_1 (°C)	Enthalpy variation in Pipe
Reservoir Pressure, P_1 (bar)	Pressure variation in Pipe
Mass flow Rate, $\dot{m}$ (kg/s)	Temperature variation in Pipe
Pipe Lenght, L (m)	Frictional and Hydrostatic Losses
Pipe Diameter, D (m)	
Pipe Angle, α (rad)	
Pipe roughness, ϵ (mm)	
Overall heat transfer coefficient, U (W/(m^2 K))	
Temperature gradient in surrounding rock, dT_∞ (°C/km)	
Number of integrals, N	

3.2.2 TEPP (v2.0) - Alternating mass flow rate version

This version is developed to obtain temperature, enthalpy and pressure variations at different mass flow rates. The flow chart for TEPP(v2.0) is available in Figure.3.4. Input variables are the same as those presented in Table 3.1 with exception of the mass flow rate. The user sets the endpoints and steps of the mass flow rate as needed. As an example, the lower mass flow rate can be set to 5 kg/s with a step of 5 kg/s up to 50 kg/s resulting in plots regarding temperature, enthalpy and pressure variations for ten mass flow rates (5, 10, 15,..., 50 kg/s). A MATLAB

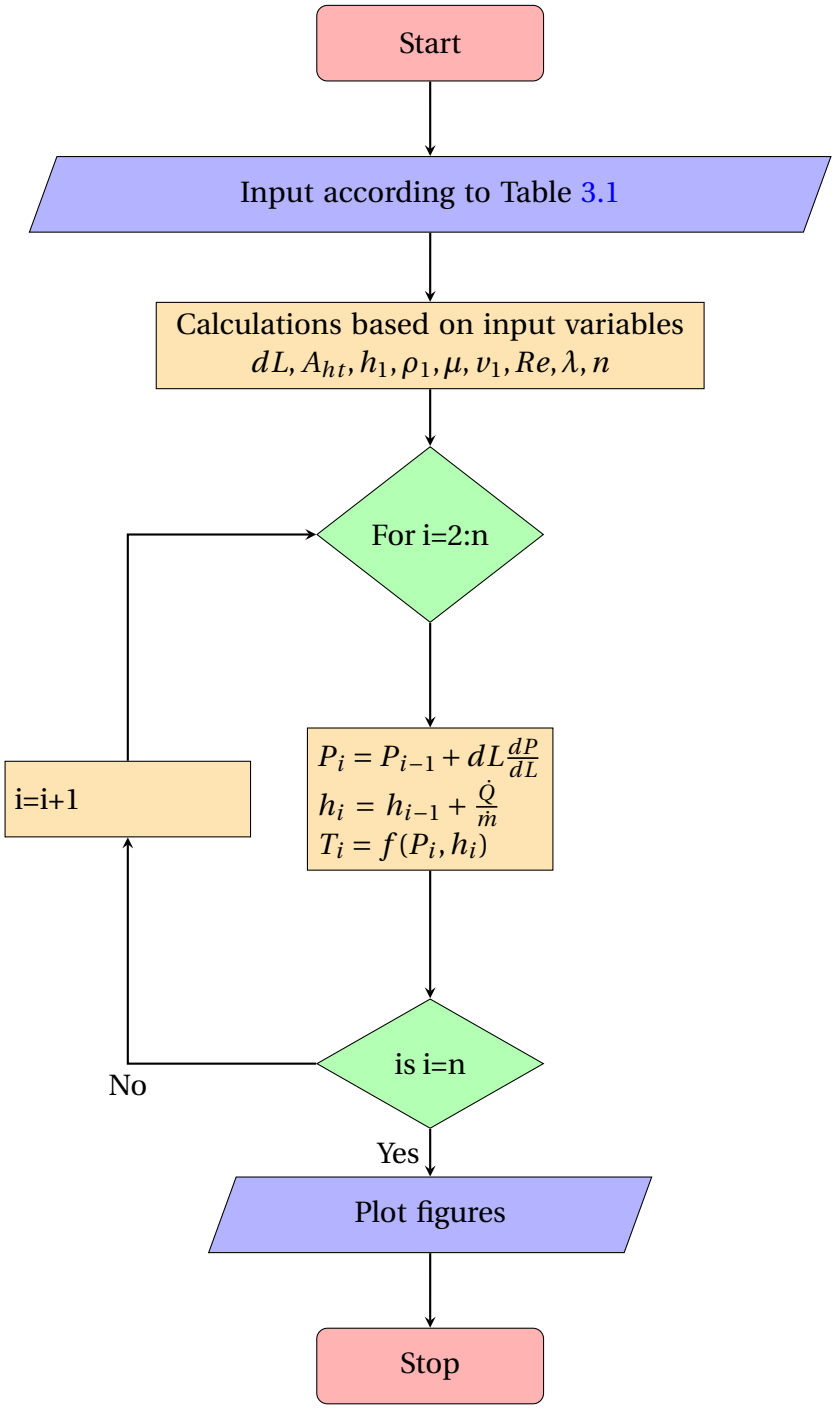

Figure 3.3: Flow chart for TEPP (v1.0). Where $n = N+1$ to include the properties of the well, according to Table 3.2. MATLAB script available in Appendix B.1.

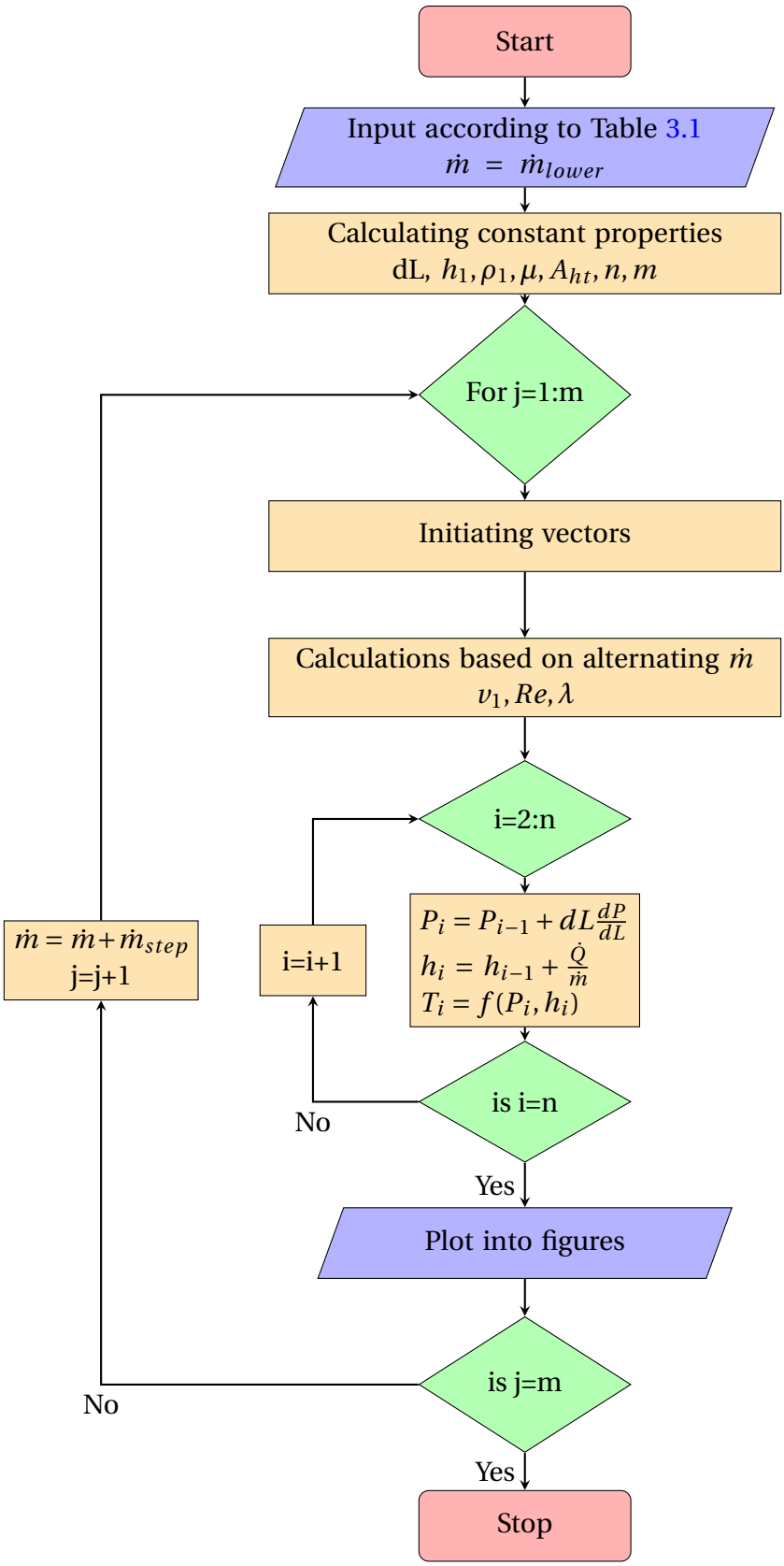

Figure 3.4: Flow chart for TEPP (v2.0) for alternating mass flow rate. Where m is the number of mass flow rates analyzed based on input according to Table 3.4. MATLAB script available in Appendix B.2.

script for this version is available in Appendix B.2 and further demonstrated in examining geothermal extraction for the case study in Section 3.3.3. The program provides the examination of selected mass flow rates which may further be analyzed or further developed to approximate the optimized range of mass flow rate, further discussed in Section 3.5.

3.3 Case study - Extraction of Geothermal Fluid - Results

TEPP is used to consider geothermal extraction from the reservoir to the wellhead for the case study examined in this paper. The inlet variables for TEPP in the case study are presented in Table 3.2.

3.3.1 Case Study conditions

Following is a short presentation regarding the chosen case study conditions. Both the depth of the well and the diameter of the production pipe is set to 5000 m and 21.59 cm, respectively, as a result of the aim of IDDP-2 (Ingason et al., 2015). For the purpose of this study, the pipe is assumed vertical, leading to a pipe length of 5000 m. Pressure and temperature of the reservoir are set to 230 bar and 550 °C as presented in Section 2.5. Pipe roughness is set to 0.015 mm as for stainless steel. The flow rate is set to 50 kg/s as a result of the maximum flow rate discharges from IDDP-1 (Einarsson et al., 2015). Furthermore, the geothermal gradient in the surrounding rock is set to the average geothermal gradient, 30 °C/km, with a top-site temperature of 20 °C (Barbier, 2002). Overall heat transfer coefficient is assumed to be 1 (Næss, 2018). Further discussion regarding these variables is provided in Section 3.5.

3.3.2 TEPP (v1.0) - Basic version - Results

Figure 3.5 show the resulting plots for the case study by the use of the developed TEPP basic version (v1.0) with input values as presented in Table 3.2. Calculated thermodynamic properties of the fluid at the well-head are presented in Table 3.3. A pressure loss of 70 bar and a temperature loss of 55 °C is calculated, which seem realistic for these conditions. The perhaps most interesting observation from Figure 3.5 is the variation regarding frictional and hydrostatic contribution to pressure loss. At the bottom, the hydrostatic contribution is dominant while from 3000 m depth until top-site the frictional contribution dominates. For the purpose of discussion, Eq.3.17 is rearranged to emphasize how hydrostatics, as well as friction, contribute to the equation used to calculate pressure loss

$$P_{n+1} = P_n + dL(-\underbrace{g\frac{\rho_1}{P_1}P_n sin\alpha}_{hydrostatic} - \underbrace{\lambda\frac{P_1\rho_1 v_1^2}{P_n 2D}}_{friction}) \tag{3.25}$$

From Eq.3.25 the pressure at a given point, P_n, is present both in the hydrostatic and frictional contribution to the pressure loss. However, in the hydrostatic contribution, it is present as a multiplier while in the frictional contribution present as a diminisher. As the remaining elements in the equation are previously set by the user, calculated by the program or assumed constant in the basic version of TEPP (v1.0), the pressure at a given point, P_n, is the only variable in the integration procedure. Based on this, the hydrostatic contribution to pressure loss decreases as the fluid ascends in the pipe while the frictional contribution increases as the pressure decrease. However, it should be emphasized that the relation between these factors as presented in Figure 3.5, is not characteristic for other wells, as it highly depends on the characteristics of the well. As an example, if the diameter of the production well is very large or the roughness of the pipe is very small, the hydrostatic contribution will be dominant throughout the entire pipe.

Table 3.2: Input values to TEPP (v1.0) for the case study.

Element	**Case study**
Reservoir Temperature (°C)	500
Reservoir Pressure (bar)	230
Mass flow rate (kg/s)	50
Pipe Length (m)	5000
Pipe Diameter (m)	0.2159
Pipe Angle (rad)	$\pi/2$
Pipe Roughness (mm)	0.015
Overall heat transfer coefficient (W/(m^2 K))	1
Temperature gradient in surrounding rock (degrees/km)	30
Number of integrations, N	100

Table 3.3: Top-site conditions for case study calculated by the use of TEPP (v1.0)

Element	**Top-site conditions for Case study**
Temperature (°C)	459.22
Enthalpy (kJ/kg)	3170.5
Pressure (bar)	159.95

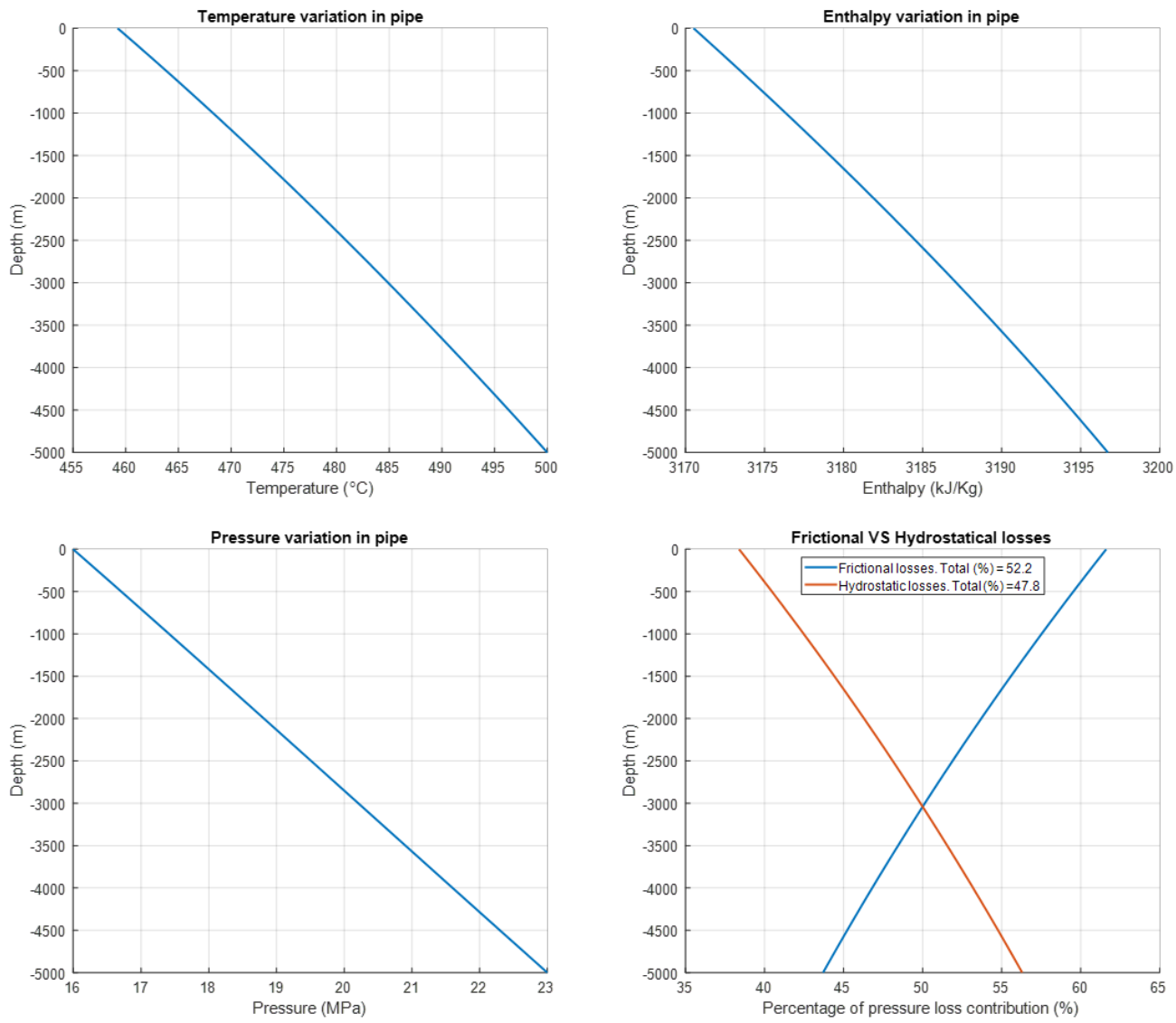

Figure 3.5: Resulting plots from calculations by TEPP (v1.0) with input variables as presented in Table 3.2

3.3.3 TEPP (v2.0) - Alternating mass flow rate version - Results

Figure 3.6 show the resulting plots for the case study by the use of the developed TEPP (v2.0) for alternating flow rates with input values presented in Table 3.4. As may be observed from the plots, increased mass flow rate leads to increased pressure drop and decreased enthalpy loss. Increased pressure drop as a result of increased mass flow rate may be observed from Eq.3.25, the variables which change as a result of increased mass flow rate is the velocity in the pipe inlet, v_1, and the friction factor, λ, leading to an increased pressure drop due to friction. Decreased enthalpy change as a result of increased mass flow rate may be observed from Eq.3.23. The two factors which vary in this equation due to increased mass flow rate are $\dot{Q}$ and $\dot{m}$.

Table 3.4: Input values to TEPP (v2.0) for the case study.

Element	**Case study**
Reservoir Temperature (°C)	500
Reservoir Pressure (bar)	230
Lower Mass flow rate (kg/s)	10
Upper Mass flow rate (kg/s)	50
Mass flow rate step (kg/s)	10
Pipe Length (m)	5000
Pipe Diameter (m)	0.2159
Pipe Angle (rad)	$\pi/2$
Pipe Roughness (mm)	0.015
Overall heat transfer coefficient (W/(m^2 K))	1
Temperature gradient in surrounding rock (degrees/km)	30
Number of integrations, N	100

The heat transfer rate, $\dot{Q}$, increases as a result of increased mass flow rate for this case. Still, the increasing mass flow rate is dominant and diminishes the $(Q/\dot{m})$ factor in Eq.3.23, leading to a decreased enthalpy change as mass flow rate increases in the case study.

From Figure 3.6 there appears to be no obvious correlation between increased mass flow rate and temperature change. Following is a discussion regarding this tendency. Firstly, in the integration procedure of TEPP, the temperature is calculated from steam tables at one point after pressure and enthalpy at that point is calculated. Thus, small errors in pressure and enthalpy calculations may result in miss-leading temperature calculations. Secondly, as may be observed from the red circle in Figure 3.7 (representing the area in the P-h diagram where the case study is considered), the temperature dependency on pressure and enthalpy is non-linear. For pressures below approximately 10 bar and in the region to the right of the saturated vapour line, the temperature is independent of pressure. However, in the region considered in this study, the temperature is both dependent on pressure and enthalpy. Two situations were performed in TEPP to determine this dependency. Firstly, the influence of pressure on temperature due to increasing mass flow rate was analyzed by keeping enthalpy constant (i.e. neglecting heat transfer). The result of this consideration may be observed from the left plot in Figure.3.8, revealing that the temperature change increases as a result of increasing pressure loss when enthalpy is kept constant. Secondly, the influence of enthalpy on temperature due to increased mass flow rate was analyzed by keeping the pressure constant. The result of this consideration may be observed from the right plot in Figure.3.8, revealing that the temperature change decreases as a result of decreasing enthalpy change when pressure is kept constant. From these observations, pressure and enthalpy have an opposite effect on the temperature for increased mass flow rate in the region of consideration (Fig.3.7). Thus, the inconsistent temperature change due to an increased mass flow rate in Figure.3.6 is probably a consequence

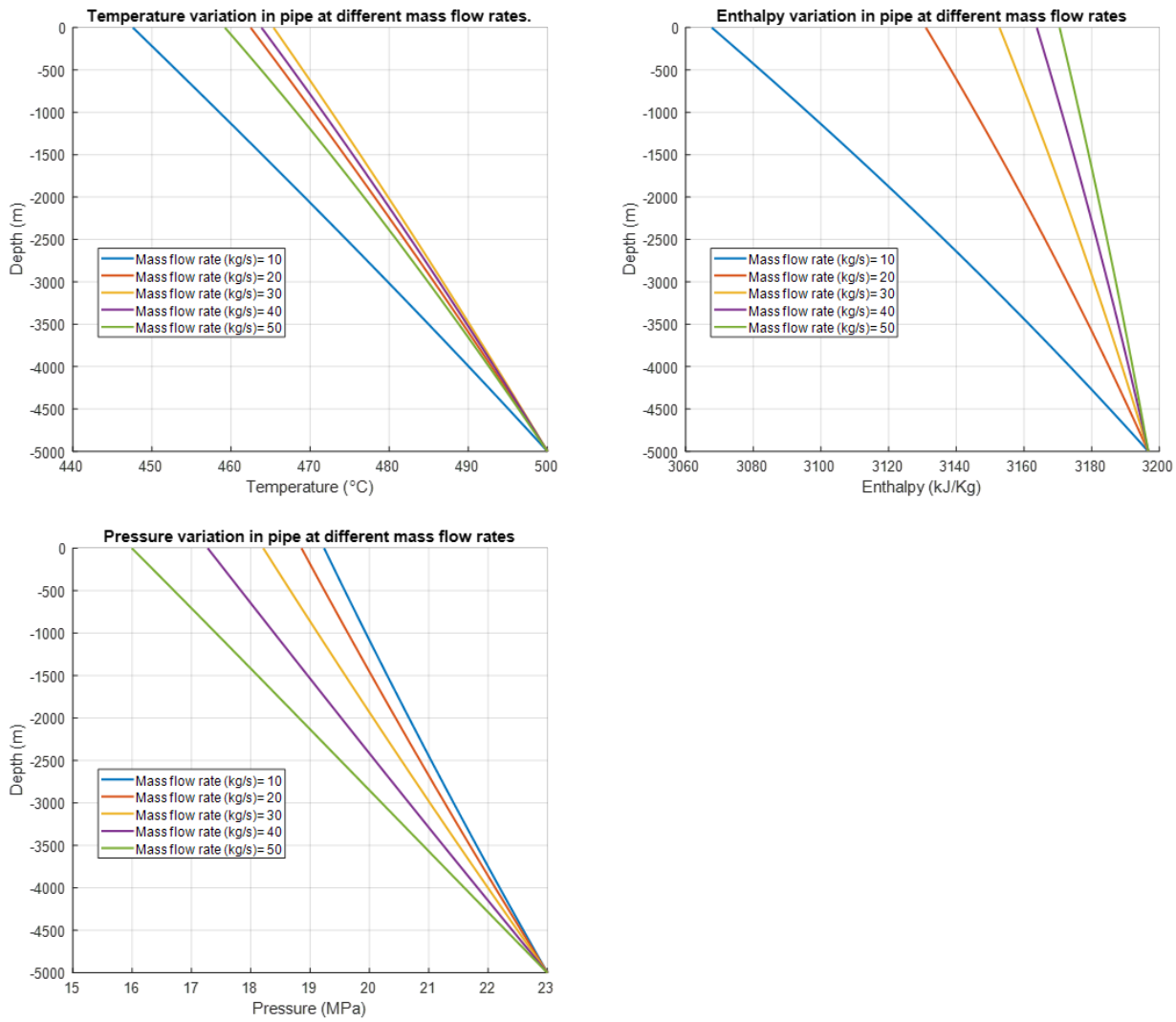

Figure 3.6: Resulting plots from calculations from TEPP (v2.0) with input variables as presented in Table 3.4

of that neither pressure or enthalpy effects on temperature is dominant for the case considered. However, it should be emphasized that this tendency is not valid for all cases in this region, but highly dependent on the input variables. As an example, if the overall heat transfer is increased to 10, the effect of enthalpy on temperature change would be dominant, leading to a decreasing temperature change as a result of increased mass flow rate. The validation of the program is further discussed in Section 3.5.

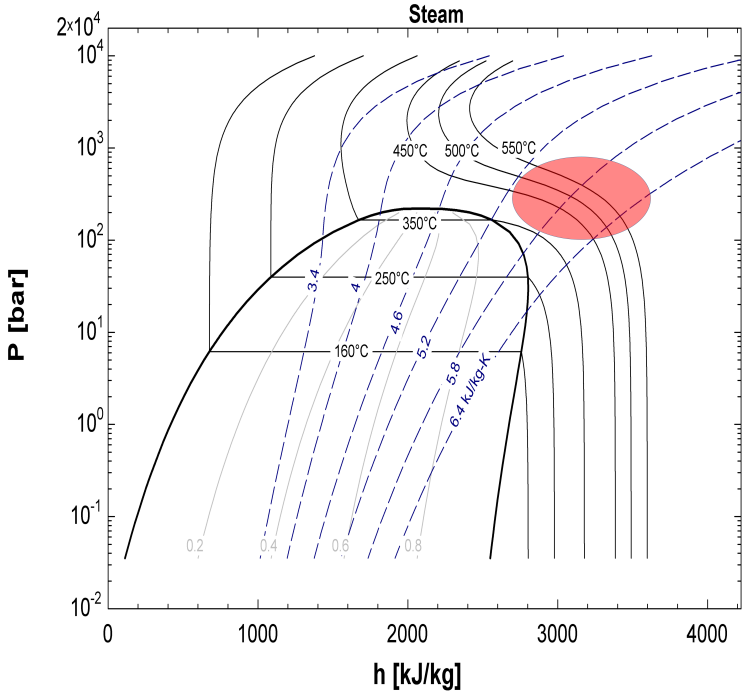

Figure 3.7: Pressure-enthalpy diagram for steam. The red circle represent the region considered in the case study regarding extraction from the reservoir to wellhead.

3.4 Suggestions for Further Development of TEPP

Multiple modifications may be carried out regarding TEPP, a few suggestions follows. As the program integrates throughout the pipe section, pipe parameters may be altered for different sections of the pipe, e.g. pipe diameter and/or pipe angle. This would certainly prove beneficial as most geothermal wells are not completely vertical and often contain altering production pipe diameters throughout the pipe section. Furthermore, TEPP (v2.0) may be modified to analyze the optimal value for the mass flow rate of a system. However, this optimization procedure would require a well-known reservoir as well as include the power generation cycle. Firstly, the conditions of the reservoir (including volume, the rate of recharge and pressure) would reveal which range of mass flow rate the reservoir is able to produce over periods of time without emptying the reservoir. Secondly, the mass flow rate is also of consideration in developing the power generation cycle. Thus, the development of such an optimization procedure would require analyzing the whole geothermal system.

The pipe roughness for the case study was set to 0.015 mm as for stainless steel. Even though stainless steel is expensive compared to other commercial materials used in geothermal production pipes, it is chosen to emphasize the potential of the well. However, this would probably lead to great expenses compared to other pipe material with higher roughness.

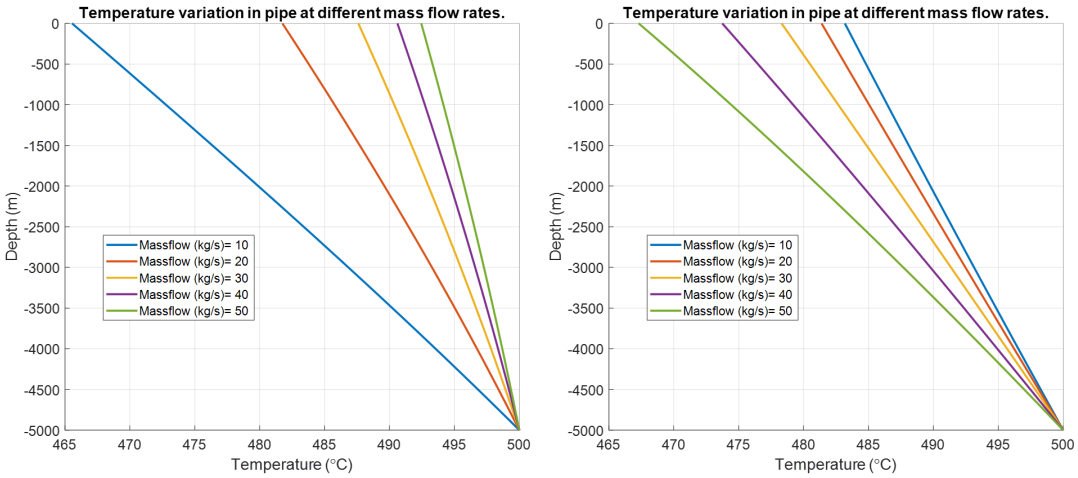

Figure 3.8: Plots to examine the temperature dependency on pressure and enthalpy as a result of increased mass flow rate for TEPP (v2.0). The left plot considers constant enthalpy while the right plot considers constant pressure for the case study.

The selection of pipe material is an optimization procedure between expenses and well performance. TEPP could certainly be further developed for this purpose. By alternating pipe roughness according to specified materials in addition to account for specified material costs, the first approximation of optimized pipe material could be achieved.

Furthermore, it should be pointed out that TEPP does not account for precipitation or scaling of the fluid, or any other flow-preventing phenomenon during extraction as the fluid is approximated as pure steam. This is certainly a weakness of the program, as the presence of some chemical compounds may lead to a severe reduction of power plant performance. Implementing some degree of a foul factor as a result of the occurrence of such chemical compounds could surely lead to a higher accuracy of the program, especially if the presence of these compounds are presented in a great amount in the geothermal water, which is the case for the chemical composition in Table 2.6. The compounds of most significant concern in high-temperature geothermal wells are silica (SiO_2) and hydrogen chloride (HCl), which may cause severe scaling and corrosion issues, respectively. In addition, in some geothermal systems where the temperature gradient in the surrounding rock is specified, this could be implemented into TEPP resulting in a better accuracy of the heat transferred from the pipe.

3.5 Discussion

Even though some discussion is previously carried out both in analyzing the results of the case study in Section 3.3 and in suggestion further development of the program in Section 3.4, this Section aims to discuss the validity of the currently developed program.

Preferably TEPP would be validated by comparison with experimental data. However, such data for supercritical water or superheated steam could not be acquired during this study. First of all, temperature and pressure logs at these conditions are expensive and difficult as it requires equipment which could resist high pressure and temperatures as well as the chemical composition of the fluid. Secondly, an attempt at retrieving such information from some large geothermal energy companies was attempted, resulting in a conclusion that such information is of sensitive concern.

As stated in the introduction to this Chapter, the fluid was assumed superheated and to obey the ideal gas law, and the implications of these assumptions remain to be determined. Mainly due to the fact that supercritical water pipe flow is not well defined, as water at these conditions contains distinct physical properties to subcritical conditions. These simplifications may certainly diminish the accuracy of the program. However, as the fluid ascends in the pipe section, the pressure of the working fluid decreases and transitions from the supercritical to the superheated region at ~ 4600 m for the case study examined in Section 3.3.2. Thus, for this case, most of the calculations are carried out in the superheated region. Still, the effects of this approximation is not well known, and the program should be validated through comparison with experimental data to reveal the accuracy of this approximation.

Still, Thórhallsson et al. (2014) has provided calculations regarding temperature and pressure variations in relation to the aim of the IDDP-1 well. Figure 3.9 demonstrate the corresponding comparison plots. The conditions set in TEPP for this comparison was set as similar to the conditions examined by Thórhallsson et al. (2014) as possible. One exception which should be emphasized is the values for the temperature gradient in the surrounding rock. For this comparison TEPP was calculated with a temperature gradient of 30 °C/km while a non-linear temperature gradient is assumed in the calculations provided by Thórhallsson et al. (2014). Based on the results, a 10% error occurs regarding the outlet pressure between the methods in comparison and an error of 32% regarding the outlet temperature with an assumed overall heat transfer coefficient of one (i.e. U=1). The error regarding temperature seems excessive, however, the calculations of temperature are highly dependent on the assumed overall heat transfer coefficient (Amongst other elements). As may be observed from Figure 3.9, an assumed overall heat transfer coefficient of three (i.e. U=3) reveals a greater approximation for this case, revealing an error of 7.35%.

However, this comparison is not an accurate validation of the program for several reasons.

First of all, the data retrieved from the work done by Thórhallsson et al. (2014) were manually extracted from plots, certainly resulting in some degree of human error. Secondly, as the data which TEPP is compared to is also based on calculations, this should prove as another source of uncertainty. Nonetheless, this comparison should prove some degree of validation for TEPP, even though comparison with experimental data should be accomplished to give a better approximation of the accuracy of the program.

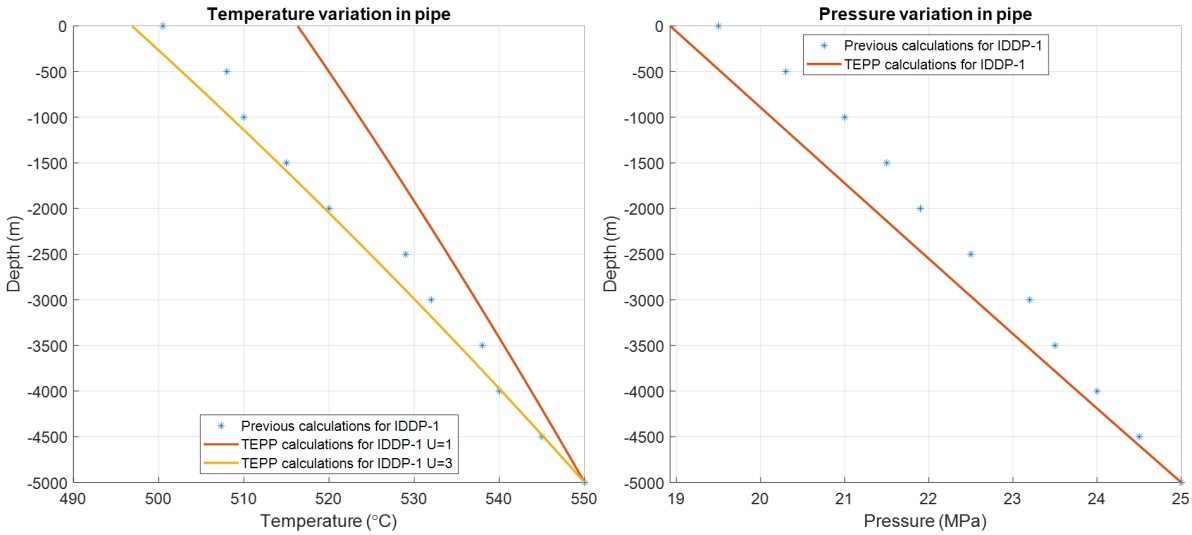

Figure 3.9: Comparison between previously calculated data conducted by Thórhallsson et al. (2014) and TEPP, regarding pressure and temperature variations in the predicted IDDP-1 well. In the temperature plot, TEPP calculations with overall heat transfer coefficient of one and three are presented (i.e. $U = 1$ and $U = 3$), to emphasize the dependency on this coefficient for the system.

Chapter 4

Electric Power Production

High-temperature geothermal power plants convert high-temperature geothermal energy to electricity. By the use of steam turbines, heat and pressure energies in the steam are converted to mechanical energy, which is further converted to electrical energy in generators. This chapter commences by presenting the most common geothermal power plant designs. Furthermore, the development of the case study which evaluates five models for geothermal energy utilizing, with the wellhead calculations achieved in Chapter 3, is presented, including theoretical background and method. Results from the simulations of the models are presented and evaluated as well as discussing their characteristics and effectiveness. Finally, some considerations for further development is presented.

4.1 Technology for Conversion to Electrical Energy

In designing geothermal plants for conversion to electrical energy, several parameters have to be considered, including pressure, temperature, contamination and precipitation potential of the steam. High-temperature resources commonly produce either steam or a mixture of steam and water from the production wells. Resources which deliver steam to the power plant may be led directly to the turbines if the contamination and precipitation potential are acceptable. If the steam is mixed with water, the mixture is commonly separated in a pressure vessel, also known as a separator or a flash tank. The separated steam is subsequently led to the power station where it drives one or more steam turbines to produce electric power. The remaining separated geothermal water (brine) is either utilized in a binary cycle type plant, or disposed of back into the reservoir through reinjection wells. The following is a brief description of each of the technologies most commonly used to utilize high-temperature resources for power generation, including Dry steam-, Flash steam-, and Binary cycle power plants (Fig. 4.1). The structure of the geothermal power plant depends highly on the properties of the available geothermal fluid, and thus, geothermal power plants solutions are often site-specific. In addition, the reader is

encouraged to examine the geothermal power plant designs presented by Tester et al. (2006) on power utilization from enhanced geothermal systems.

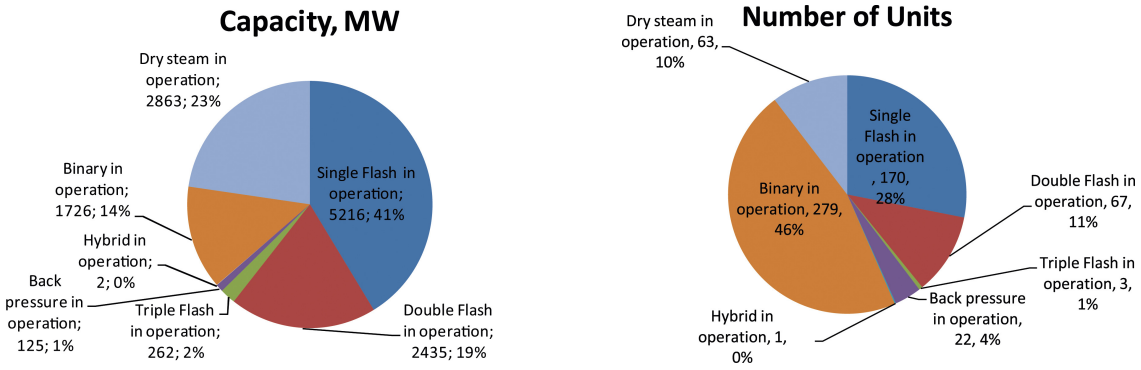

(a) Installed capacity in MWe (and%) for each plant typology (total 12,6 GWe) (Bertani, 2016)

(b) Number of units (and%) for each typology (total 613) (Bertani, 2016)

Figure 4.1: Plant category distribution

4.1.1 Dry Steam Power Plants

Dry-steam power plants systems were the first type of geothermal power generation plants built. They use steam from the geothermal reservoir as it comes from wells and routes it directly through turbine/generator units to produce electricity (Fig. 4.2). At the well, there are the usual valves plus a steam purifier. The latter is merely an in-line, axial-centrifugal separator designed to remove particulate matter from the steam before it enters the piping system. Dry-steam plants tend to be simpler and less expensive than flash-steam power in that there is no geothermal brine to contend with. Conventional dry steam turbines are available with either atmospheric (backpressure) or condensing exhaust and require fluids of at least 150°C. In the backpressure system, the steam exiting the turbine is vented directly to the atmosphere. In the condensing cycle, the outlet steam is converted into the liquid phase, reducing the outlet pressure of the turbine ensuring an increase of the pressure difference between the inlet and outlet of the turbine. A larger enthalpy drop and increased work delivered to the turbine is thus obtained in the condensing cycle compared to the backpressure system. In addition, at identical turbine inlet pressure conditions, the backpressure system requires twice as much steam per produced kilowatt-hour (kWh) compared to a condensing cycle. Therefore, backpressure turbines are often only used as pilot or/and standby plants in case of small supplies from remotely isolated wells and for generating electricity in the early stages of field development. (DiPippo, 2012)

Steam technology is still effective and currently in use at The Geysers in northern California, the world's largest single source of geothermal power (DiPippo, 2012). As of 2015, dry steam

power plants contribute to 23% of the total installed capacity regarding geothermal energy, with 63 units in operation (Fig. 4.13).

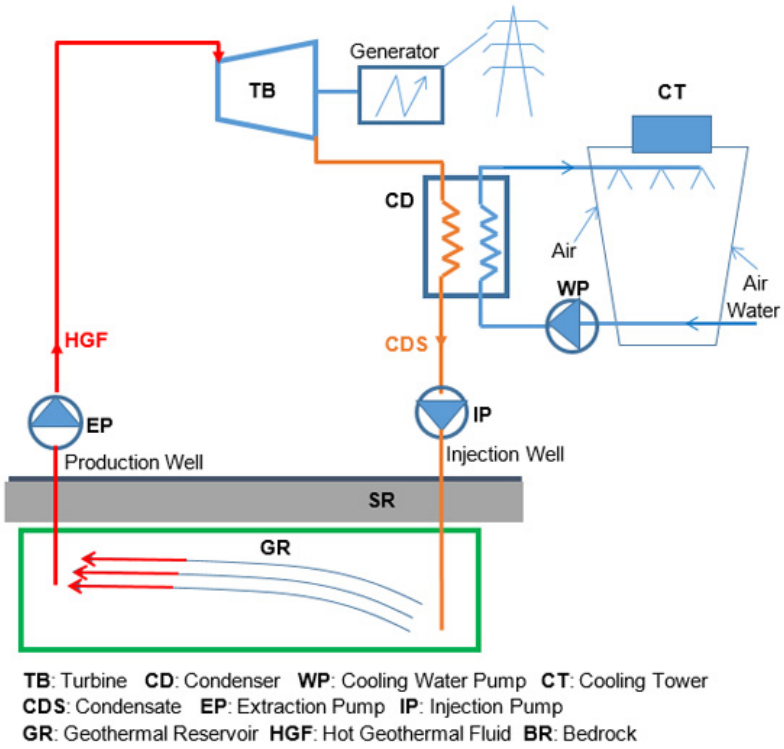

Figure 4.2: Schematic of a Dry steam power plant (Zinsalo and Lamarche, 2017)

4.1.2 Flash-Steam Power Plants

Some *Advantages* of flash-steam geothermal power plants

- Very low emissions, safe and reliable, immune to varying weather conditions, cost effective over life of plant, sustainable, small footprint and no fuel cost.

Some *Disadvantages* of flash-steam geothermal power plants

- High initial cost, increased risk of seismic activity, location sensitive and risk of overexploiting resources.

Single-Flash Steam Power Plants

The single-flash steam plant is the pillar of the geothermal industry. It is frequently the first power plant installed in newly developed liquid-dominated fields (DiPippo, 2015). As of 2015,

there are 170 units of this type in operation around the world with an installed capacity of 5216 MW (about 30 MW/unit) contributing to 41% of all geothermal plants (Fig. 4.1b).

Single-flash plants are mainly provided with a mixture of steam and liquid, and is a relatively simple process of converting geothermal energy into electricity. Firstly, the mixture is separated into distinct steam and liquid phases through a separator (flash tank) with a minimum loss of pressure (Fig. 4.3). For this purpose, a cylindrical cyclonic pressure vessel is used, often oriented with its axis vertical where the two phases disengage owing to their inherently large density differences. Secondly, the steam is brought through a turbine where it produces electrical energy before it is brought to a condenser, with the main purpose of condensing the steam into the liquid phase. Water towers are often used to enhance the condensing process. Finally, the liquid exiting from the separator and the condenser is brought back into the geothermal field through reinjection wells or used in direct use systems. It should be mentioned that the process presented in Figure 4.3 is a common design of a single-flash power plant, though several arrangements for the separators and design of the plants is possible, depending on the geothermal system. (DiPippo, 2015)

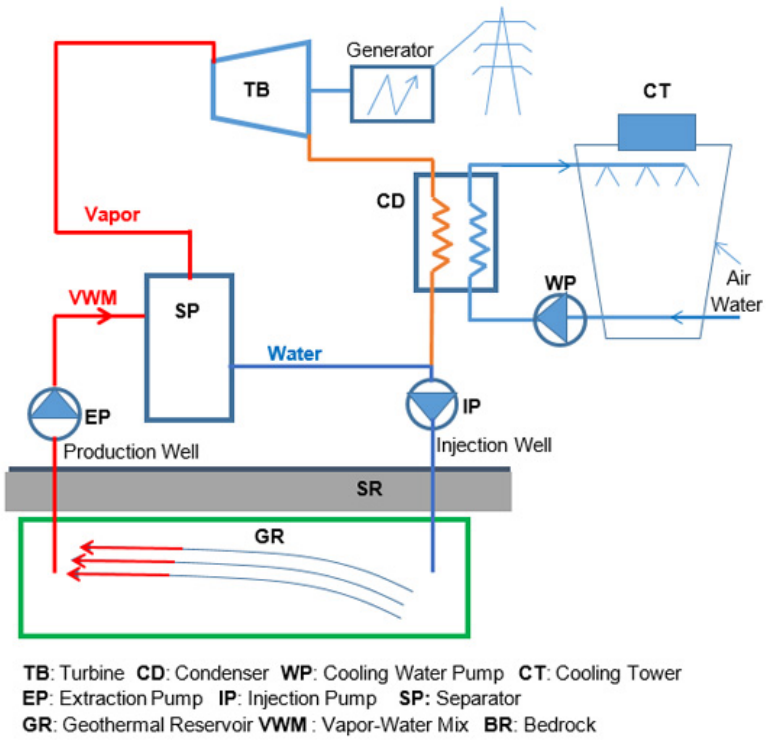

Figure 4.3: Schematic of a single-flash power plant (Zinsalo and Lamarche, 2017)

Double- Triple-Flash Steam Power Plants

The single-, double- and triple-flash systems are distinguished by the further implementation of respectively one and two flash processes imposed on the separated liquid leaving the primary separator. Which has the purpose of generating additional steam, even though at lower pressures than the primary steam.

A design of a double-flash steam plant is presented in Figure 4.4, the low-pressure steam leaving the first flash tank is further used in a secondary flash tank, the additional steam extracted in this process is brought into a secondary turbine with the purpose of increasing the power output. For the same geothermal fluid conditions, a double-flash steam plant can increase the power output with 15–20% compared to a single-flash steam system. This modification results in a system of greater complexity, higher cost, and higher maintenance requirements. However, the extra power output often justifies the installation of such plants. (DiPippo, 2015)

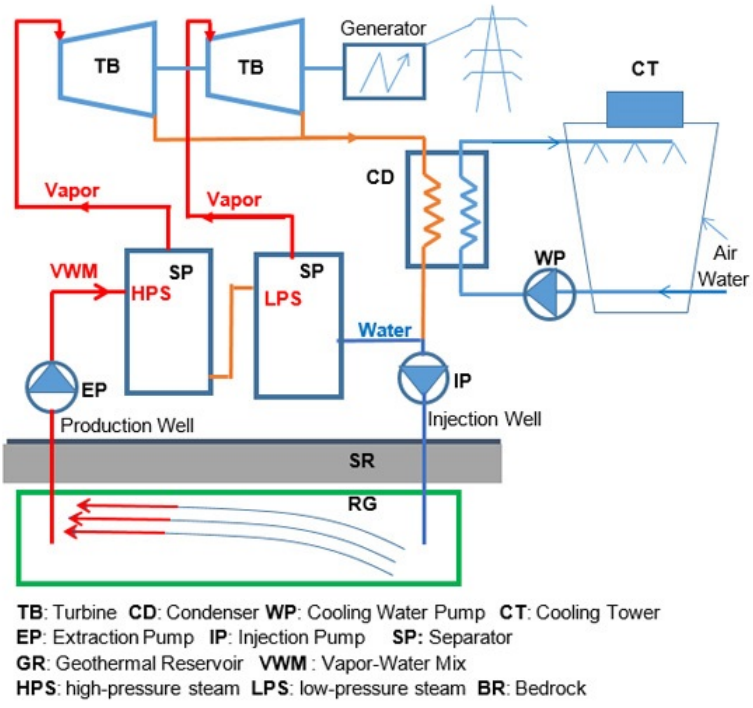

Figure 4.4: Schematics of a double-flash power plant (Zinsalo and Lamarche, 2017).

Even further increase on the power output can be achieved through the use of a triple-flash steam plant, characterized by an even more complex and costly system compared to double-flash systems, which is often not justified by the increased power output. In addition, flashing of the fluid down to lower pressures may result in precipitation of e.g. silica, either in the

plant equipment or in the piping/well system. Thus, triple-flash steam plants are only installed in cases of very high-temperature resources. (DiPippo, 2015) As of 2015, these plants contribute to 19% (Double-flash) and 2% (Triple-flash) of the installed capacity in the world (Fig.4.13).

4.1.3 Binary Cycle Power Plants

Binary cycle plants are typically utilized where reservoirs contain a temperature greater than 100°C and less than 220°C. The principal elements of this type of plant is illustrated in Figure 4.5. The binary cycle includes a heat exchanger, where the reservoir fluid (either steam and/or water) is passed through, while heating a secondary working fluid that is typically an organic fluid with a boiling point lower than 100°C, such as isopentane. The secondary fluid is vapourized and further used to run a turbine before it is condensed and re-enters the heat exchanger, forming a closed loop. Binary cycle power plants vary in size from 500 kW to 10 MW with a typical efficiency of 7–12%, depending on the temperature of the primary (geothermal) fluid. (DiPippo, 2015)

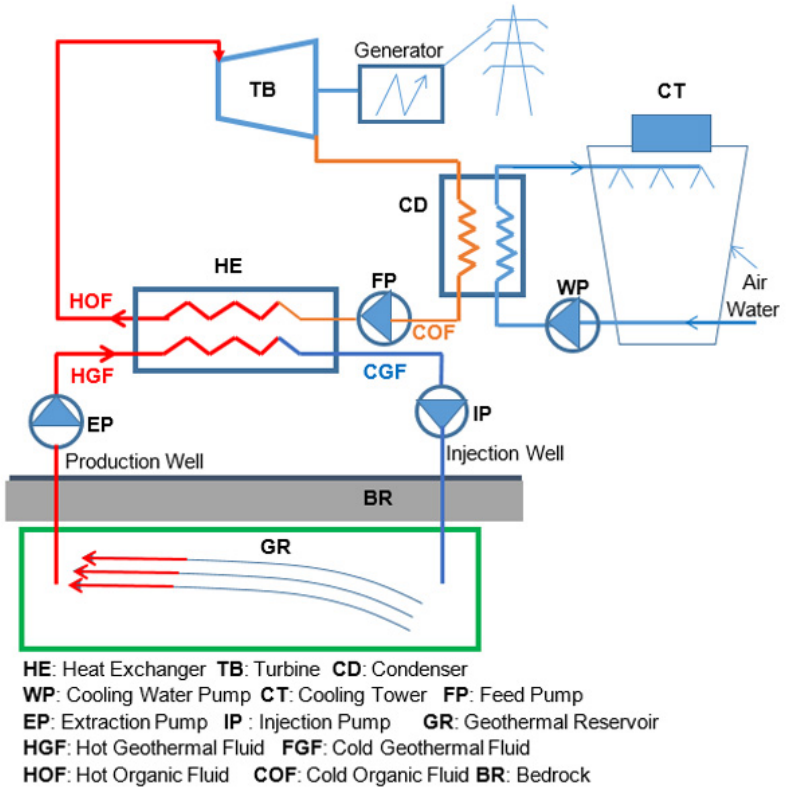

Figure 4.5: Schematics of a Binary cycle power plant (Zinsalo and Lamarche, 2017).

4.2 Case Study - Power Production - Theory

Following is a derivation of the equations used to simulate the devices present in the models of the case study. Including valve, turbine and heat exchanger.

4.2.1 Throtteling Valve

A throttling valve is a device that is used to restrict flow to cause a considerable pressure drop (Fig. 4.6).

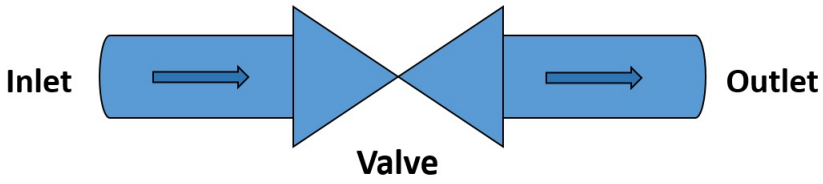

Figure 4.6: Schematic diagram for a valve.

Starting with the first law of thermodynamics at steady state for the valve

$$\dot{Q} - \dot{W} = \dot{m}\left[h + \frac{1}{2}v^2 + gz\right]_{in}^{out} \tag{4.1}$$

Further, the valve is assumed to be well-insulated with no moving parts, and thus, heat and work effects are neglected. In addition, gravitational losses, as well as head losses, are assumed to have a minor effect. Equation 4.1 becomes

$$\dot{m}_{out}(h_{out} + \frac{1}{2}v_{out}^2) = \dot{m}_{in}(h_{in} + \frac{1}{2}v_{in}^2) \tag{4.2}$$

Changes due to velocity are neglected and mass conservation is assumed (i.e. $\dot{m}_{out} = \dot{m}_{in}$). Thus, the flow through the valve is assumed isenthalpic

$$h_{out} = h_{in} \tag{4.3}$$

4.2.2 Turbine

The turbine is a device in which fluid expands (Fig. 4.7). During the expansion work will be done by the fluid to drive, for example, an electric generator, resulting in power output.

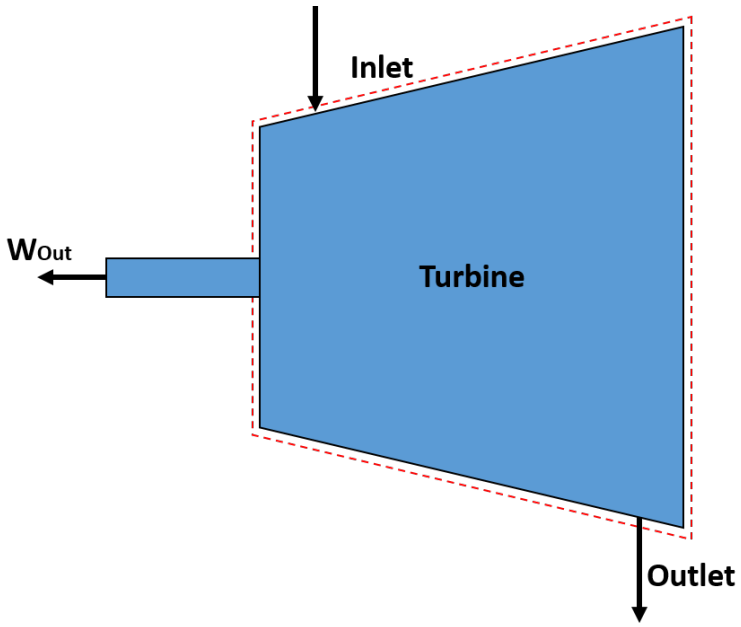

Figure 4.7: Schematic diagram for a turbine, the control volume isrepresented by the red dashed lines.

Starting with the first law of thermodynamics at steady state for the turbine in Figure 4.7

$$\dot{Q} - \dot{W} = \dot{m}\left[h + \frac{1}{2}v^2 + gz\right]_{in}^{out} \tag{4.4}$$

The change of kinetic energy an potential energy for fluid flowing into and out of a turbine are very small compared to the enthalpy change, and can usually be neglected

$$\left[\frac{1}{2}v^2 + gz\right]_{in}^{out} = 0 \tag{4.5}$$

Furthermore, the turbine is assumed well insulated (i.e. $\dot{Q} = 0$) and mass flow rate is conserved (i.e. $\dot{m}_{in} = \dot{m}_{out}$). For a turbine, work is delivered out of the control volume, explaining the minus sign in Eq. 4.4. With these assumptions and simplifications, the power done by the turbine can be expressed as

$$\dot{W} = \dot{m}(h_{in} - h_{out}) \tag{4.6}$$

Most steady-flow devices (turbines, compressors, nozzles) operate under adiabatic conditions, but they are not truly isentropic but are rather idealized as isentropic for calculation

purposes (Fig. 4.8). For this purpose, η_T is defined as the ratio of real work done by the turbine to work by the turbine when operated under isentropic conditions

$$\eta_T = \frac{\text{Real Turbine Work}}{\text{Isentropic Turbine Work}} = \frac{W_{real}}{W_s} = \frac{h_2 - h_{3r}}{h_2 - h_{3s}} \tag{4.7}$$

This is further illustrated in the h-s diagram in Figure 4.8. By rearranging Eq.4.7, the real enthalpy exiting the turbine may be expressed as

$$h_{3r} = h_2 - \eta_T(h_2 - h_{3s}) \tag{4.8}$$

When the inlet and outlet pressures of the turbine is set (P_2 and P_3 in Fig.4.8), the process is first assumed isentropic and the enthalpy at the point 3_s is calculated. Subsequently, the real outlet enthalpy is calculated (i.e. h_{3r}) by assuming an isentropic efficiency, η_T, and the use of Eq.4.8.

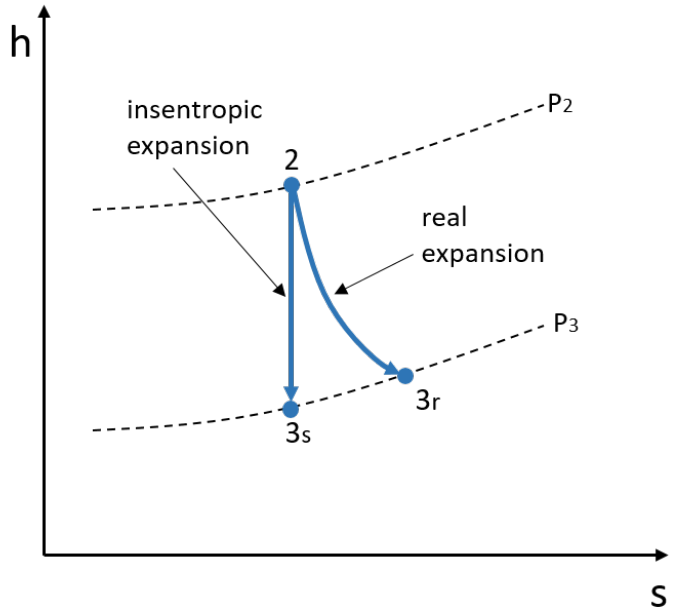

Figure 4.8: Enthalpy-entropy diagram with constant pressure lines showing the difference between an isentropic and real expansion through a turbine.

4.2.3 Heat Exchanger

Heat exchangers are devices for transferring heat between two fluids at different temperatures. In most cases, the two fluids are not in contact, and the transfer is through an exchange area (Fig. 4.9).

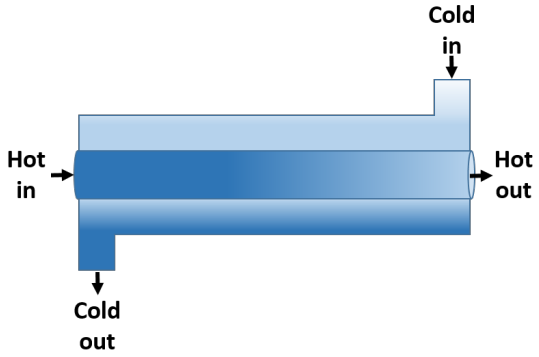

Figure 4.9: Concentric tube heat exchanger with counterflow. Presented to clarify the derivation of Eq.4.10.

Starting with the first law of thermodynamics

$$\sum_{i=1}^{\infty} \dot{Q}_i + \sum_{j=1}^{\infty} \dot{W}_j = \sum_{k=1}^{\infty} \dot{m}_k \left[h_k + \frac{1}{2} V_k^2 + g z_k \right]_{in}^{out} \tag{4.9}$$

Furthermore, three assumptions are generally used in modelling heat exchangers

1. As a first approximation, it can be considered isobaric ($P_{out} = P_{in}$).
2. It is globally adiabatic, i.e. no heat exchange with surroundings ($\dot{Q}_i = 0$)
3. Heat transfer coefficients and thermophysical properties of fluids are assumed constant at any time in the entire heat exchanger.

In addition, there is no work delivered to or from the heat exchanger ($\dot{W}_j = 0$) and kinetic and potential energy changes are neglected. As a result of these simplifications, Eq.4.9 may be expressed as

$$\dot{m}_{hot}(h_{hot,in} - h_{hot,out}) = \dot{m}_{cold}(h_{cold,out} - h_{cold,in}) \tag{4.10}$$

Figure 4.9 is a sketch for a concentric tube heat exchanger with counterflow. However, the heat exchanger is basically idealized for the case study of this paper, as described in Section 4.3.1, and the type of heat exchanger is not considered. Still, the sketch is presented to further clarify the derivation of Eq.4.10.

4.3 Case Study - Power Production - Method

Five power plant designs have been simulated and evaluated, represented in Table 4.1 by their characteristics and respective sections of analysis. These power plant designs are for further reference referred to as Model I–V. This Section presents the method developed for evaluation of these models. During this study, an appropriate tool for calculating chemistry equilibrium at these conditions (high temperature and pressure) could not be attained. It was therefore decided to avoid the two-phase envelope in the power generation cycle while examining the models in this study, aiming to avoid precipitation of hazardous chemical compounds as these impacts could not be addressed at this point. This was achieved by allowing the turbines to expand isentropically down to the vapour saturation line. Thus, due to the isentropic efficiency, the real thermodynamic properties at the turbine exhaust would be in the superheated region (Fig. 4.12, see also Fig. 4.8), which is obtained as a measure of security. If the turbine expands the fluid in such a manner that the real outlet conditions (State 4 in Fig.4.12) of the turbine is at the vapour saturation line, small errors or faults in the power plant design could result in condensing of the geothermal fluid, and depending on the composition, possibly lead to severe corrosion of steam turbine components. However, to examine the potential of allowing the steam to condense, two further studies on Model I was obtained.

Based on the content of the geothermal fluid in the reservoir (Table 2.6) some form of wet scrubbing prior to the geothermal power cycle will be necessary, due to the presence of especially silica and chloride. In such, it was decided to not include such a process in the analysis, as this would diminish the efficiency of the systems, and the purpose of the evaluation is to explore the potential of the well.

For the purpose of calculation, EES was used, further described in Section 4.3.2. The limitations regarding the calculations are described in Section 4.3.1 and the method for process optimization for the models is presented in Section 4.3.3. In developing these systems, it was convenient to divide the different stages in the systems into different states (or points) as presented in Figures 4.11 – 4.19. Two states are previously set and constant for all models, including state 1 and 2, presented with their thermodynamic properties in Table 4.2. State 1 is the state of the reservoir developed in Chapter 2, while state 2 is the state of the steam at the wellhead, calculated by the use of TEPP in Chapter 3. Furthermore, the models evaluated increase in complexity, starting with a single-turbine expansion in Model I and ending up with a configuration including two heat exchangers and three turbines in Model V. In such, the purpose of this study is to examine the corresponding power output potential for each of the models. Even though an even more complex design could prove more efficient, the models obtained are the only designs which could be achieved during this study. Still, an evaluation of these models should prove fruitful regarding electric power production from deep geothermal

resources. By the use of equations previously developed for the components present in the power plant designs (Section 4.2), along with properties of steam incorporated in EES, a script has been developed in EES for each of the five designs. The scripts are available in Appendix C. The method is further discussed throughout the chapter and especially in Section 4.6.

Table 4.1: Five power plant designs have been analyzed in this study. This overview distributes the designs into case numbers (Model I – IV) and their respective number of turbines, valves and heat exchangers present in each design. In addition, their respective sections of analysis, which includes schematics for each model, is provided.

Model	Turbines	Valves	Heat Exchangers	Section
I	1	1	0	4.4.1
II	2	2	0	4.4.2
III	3	3	0	4.4.3
IV	2	1	1	4.4.4
V	3	1	2	4.4.5

Table 4.2: Properties of state 1 and state 2 in the geothermal energy power plant design process. State 1 is the state of the reservoir developed in Chapter 2, while state 2 is the state of the steam at the wellhead, calculated by the use of TEPP in Chapter 3.

State	h (kJ/kg)	$\dot{m}$ (kg/s)	P (bar)	s (kJ/kg-K)	T (°C)
1	3197	50	230	6.04	500
2	3171	50	160	6.14	459.2

4.3.1 Limitations and specifications

This study aims to analyze the potential of the respective supercritical reservoir (Table 2.6) while aiming to obtain reasonable similarities to actual geothermal power utilization processes. As such, some limitations and simplifications are made while still aiming to include the most important elements

1. First of all, the size of plant components, including pipe, turbine, valve and heat exchanger are not taken into account, and thus, not optimized. As a result, losses such as heat and friction in the pipes are neglected.

2. Furthermore, the superheated steam entering the power generation cycle is limited to be in the superheated region above the vapour saturation line, which is achieved to avoid the main issues related to hazardous chemical compounds which could occur if the steam condenses (Further discussed by (Ommedal, 2017)). This is due to the fact that

most geothermal fluids at these conditions contain compounds which may cause severe corrosion and scaling issues upon condensing. Fluid components having significant influence on corrosion and salt deposition include Na^+, $Ca^{\equiv+}$, Cl^-, and SiO_2 (Povarov et al., 2000). The fluid composition in Table 2.6 contains a significant amount of these compounds, in such, condensation is avoided in this study. Furthermore, the solubility of several compounds depends independently on temperature and pressure, and in such, challenges related to precipitation may occur even in the superheated region (Morey and Hesselgesser, 1951). Relating issues are not considered in this method.

3. The heat exchanger is idealized with a pinch of 5 °C between the exiting heat exchanger flows. Thus, it is assumed that the heat exchanger manages to obtain a temperature on the cold exiting flow which is 5 °C below the exiting hot stream temperature (Næss, 2018).

4. The isentropic efficiency, η_T, is set to 85% in all turbines present in the models.

5. The final stage considered in the designs in this study is the outlet condition after the last turbine. Commonly, the steam is lead to a condenser, with the main purpose of condensing the steam into the liquid phase. The steam is subsequently either brought back into the geothermal field through reinjection wells or used in direct use systems. The purpose of condensing the steam at the turbine exhaust is to create a vacuum, maximizing the pressure drop across the turbine, and thus, power output. In this study, the pressure of the last turbine exhaust is set to 0.2 bar, as condensers commonly perform at such conditions (Næss, 2018).

4.3.2 Development of devices in EES

EES is an acronym for Engineering Equation Solver. The basic function provided by EES is the numerical solution of linear and non-linear algebraic and differential equations. EES solves systems of equations (i.e., relationships between variables) automatically, which frees the user from having to develop their own iterative technique for solving a set of non-linear equations (Klein and Nellis, 2013).

EES was chosen for this study as it provides features for optimization, high-quality property data and a simple feature for obtaining thermodynamic diagrams. Following is a presentation regarding how the devices present in the designs evaluated in this study are developed in EES, including valve, turbine and heat exchanger.

Throttling Valve

As the steam is led to the power plant, valves become critical to the safe and efficient operation of the turbines and reservoir control. In this case, extreme measures must be taken to protect

the turbine, pumps and people working in the area. Poor valve selection or maintenance could result in damages to the plant, including turbine blades and heat exchanger tubes.

In calculating the characteristics of the valve, it is idealized from Eq.4.3, which assumes an isenthalpic process across the device. When the inlet conditions of the valve are known, the outlet conditions may be calculated for a given outlet pressure. In Figure 4.10 the characteristic for the valve with the given inlet condition (State 2, Table 4.2) is presented, showing the resulting outlet temperature for a given outlet pressure. How much the valve throttles, and thus, to which outlet pressure is of optimization concern. In fact, as further discussed in Section 4.3.3, the outlet pressures from the valves are the only variables which are to be determined in the optimization of the models in this paper. As the valve is assumed isenthalpic and the outlet valve pressure is optimized, the remaining thermodynamic properties at the outlet of the valve are calculated by the use of steam tables implemented in EES.

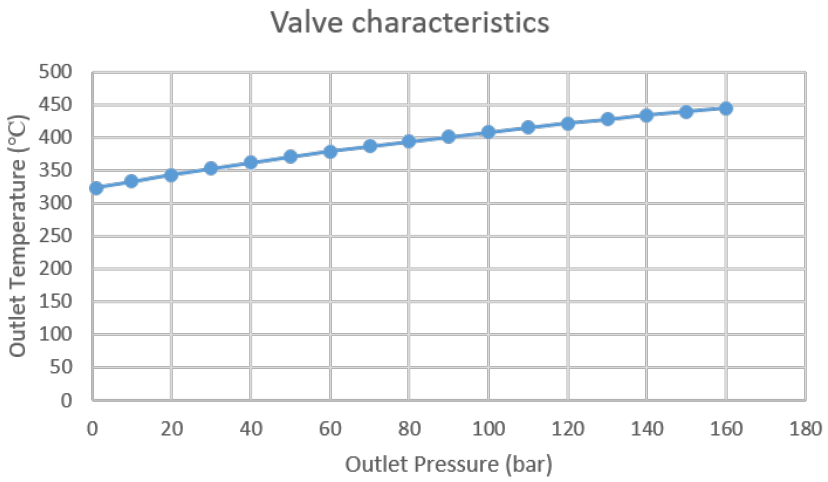

Figure 4.10: Characteristics of Valve in Case Study.

Turbine

Based on the theory for the turbine presented in Section 4.2.2, the outlet conditions may be calculated if the inlet conditions are known as well as the isentropic efficiency (η_T). All the turbines present in the models have an assumed isentropic efficiency of 85%. As the geothermal fluid at the wellhead of the geothermal power plant contain compounds which may cause severe corrosion and scaling issues upon condensing, the script developed for the turbine aims to avoid saturation of the steam. As such, the steam entering the turbine is expanded isentropically down to the vapour saturation line at constant entropy with an iterative function developed in EES. The function decreases the outlet pressure with a given step and examines the vapour quality of the steam. When the vapour quality reaches unity, the function is terminated and provides the

resulting isentropic outlet pressure. Furthermore, the outlet pressure from the real expansion is assumed equal to the outlet pressure from the isentropic expansion. The enthalpy from the real expansion is calculated with Eq.4.8 and the temperature and entropy at the outlet of the turbine are further calculated by the use of tables containing properties of steam incorporated in EES. Finally, the work delivered by the turbine may be calculated by the use of Eq.4.6.

Heat Exchanger

In the designs of Models IV and V, the steam at the wellhead (State 2) is divided and led into one and two heat exchangers, respectively. Consider the schematics of the single heat exchanger-turbine system available in Figure 4.17, the steam leaving the first turbine (State 5) is re-heated in the heat exchanger by the warmer steam (State 8). The amount of mass flow rate led into flows 3 and 8 are determined by the limitations and simplifications previously presented as well as the degree of throttle through the valve. By the optimization procedure presented in Section 4.3.3, the enthalpy change across the heat exchanger is determined by assuming that the outlet temperature of the cold stream (State 6) is 5 °C below the exiting hot stream temperature (State 9), in addition to assuming that the heat exchanger undergoes an isobaric process. When these conditions are determined, the necessary fraction of mass flow rate led into the heat exchanger may be determined from Eq.4.10 along with assuming mass conservation throughout the system. Subsequently, the mass flow rates through the different sections of the system are determined and the power output from the turbine may be calculated by the use of Eq.4.6.

4.3.3 Process Optimization

To optimize the plant performance of the five geothermal plant designs evaluated in this thesis (Model I–V, see Section 4.4), the integrated Min/Max feature in EES was used (Klein and Nellis, 2013). As Model I–III are similar, the optimization procedure for these models will be presented first. Following, the optimization procedure for Model IV-V is presented as these contain an additional device, the heat exchanger. It may be argued that this is not an actual optimization procedure, but rather a calculation procedure as the inlet conditions are previously set, the characteristics of the devices present are established and the minimum outlet pressure from the last turbine is fixed. However, the term optimization is used as two optimization methods in EES are used to determine the values for the degrees of freedom in the models. A further analysis is obtained in evaluating the models in Section 4.4.

Process Optimization - Model I–III

First of all, this explanation of the optimization procedure should be seen in context with the schematics (Figures 4.11–4.15) and scripts (Appendices C.1–C.3) for Model I–III . As a result of

the limitations and simplifications set for the case study in Section 4.3.1, Model I–III contain respectively one, two and three degrees of freedom, which are the outlet pressures from the valves. For Model I, The Quadratic Approximations optimization method was used, which is a method provided by EES to find a minimum or maximum when there is one degree of freedom. For Model II–III, containing more than one degree of freedom, The Genetic method was utilized, which is a robust optimization algorithm that is designed to reliably locate a global optimum even in the presence of local optima (Klein and Nellis, 2013). The process of optimization of these models is as following. First of all, the limited range of the outlet pressure from the valves is set, as these cannot exceed the available inlet pressure. Furthermore, a guessed value should be provided to EES to accelerate the optimization. When these conditions are set, the optimization procedure starts by calculating the process with the guessed values, and depending on the method, alternates the degrees of freedom to obtain the values which result in a maximum total power output for the system.

Process Optimization - Model IV–V

This explanation should be seen in context with the schematics (Figure 4.17 and 4.19) and scripts (Appendix C.4 and C.5) for Model IV–V. Due to the limitations and simplifications set for the case study in Section 4.3.1, Model IV–V contain one degree of freedom, which is the outlet pressure from the valve. As these two models include at least one heat exchanger, the fraction of mass flow rate led to the corresponding numbers of heat exchangers has to be determined. To explain the optimization procedure, the schematic for Model IV (Fig.4.17) is considered. Firstly, as the hot steam through the heat exchanger (State 8–9) is assumed to condensate and the device is assumed isobaric, the temperature at state 9 is calculated to be the saturation temperature at the given pressure (i.e. 160 bar). As both the temperature and pressure of state 9 is determined, the enthalpy may be calculated from steam tables incorporated in EES. Subsequently, the temperature at state 6 is set to be 5 °C below the temperature of state 9 (see Section 4.3.1). As a result of the outlet valve pressure, the thermodynamic properties at states 4 and 5 are calculated, and thus, also the pressure at state 6 and subsequently the thermodynamic properties of state 7. Now, as the thermodynamic properties at all states are calculated, the necessary fraction of mass flow rate through branch 8 may be calculated by the use of Eq.4.10 along with assuming mass conservation throughout the system. After these calculations are made, the total power output from the system is calculated for the given outlet valve pressure. By the use of The Quadratic Approximation optimization method, the value for the outlet valve pressure which leads to the maximum power output for the system is determined. A similar procedure applies for Model V, although further complicated.

4.4 Case Study - Power Production - Results & Evaluation

For the purpose of comparison, five geothermal power plant designs have been evaluated. The devices present in each system is available in Table 4.1 and their schematics and results are presented in their corresponding section of evaluation. The evaluation of these systems is obtained to compare their potential for utilization from the condition of the geothermal fluid at the wellhead (State 2). It should be emphasized that an even more complex design would surely lead to a better utilization of the energy contained in the steam, leading to a better energy efficient system. Still, the designs in this study are evaluated to determine how such simple systems would perform with the initial wellhead condition previously determined. Model I–V are calculated with an isentropic expansion down to the vapour saturation line due to the concerns presented in the introduction to this chapter. However, to evaluate the potential of allowing the steam in the turbine to condense, two further analysis are made on Model I, where the vapour quality of the steam from the real expansion (As state 3r in Fig.4.8), is set to 1 and 0.85.

4.4.1 Model I: Single valve-turbine system

The schematics for the design of Model I is presented in Figure 4.11 along with the calculated thermodynamic properties at each stage in Table 4.3. A thermodynamic plot of the process in a T-s diagram is available in Figure 4.12.

Table 4.3: Thermodynamic properties at each state for Model I with superheated steam exiting the turbine exhaust as shown in Figure.4.12. Schematic available in Figure 4.11. Calculated with the developed EES script, available in Appendix C.1.

State	h (kJ/kg)	$\dot{m}$ (kg/s)	P (bar)	s (kJ/kg-K)	T (°C)	P_{is} (bar)	T_{is} (°C)
1	3197	50	230	6.04	500		
2	3171	50	160	6.14	459.2		
3	3171	50	2.84	7.90	349.2		
4	2694	50	0.21	8.14	104.1	0.21	60.6

The steam from the wellhead (State 2) is led through a throttling valve and further into a turbine for utilization of the energy contained in the steam. As a result of the optimization procedure in EES, the pressure of the steam at the outlet of the valve (State 3) is calculated to 2.84 bar, a throttling from 160 bar to 2.84 bar is thus achieved through the valve. The main reason for this calculation may be observed in Figure D.1, where the vapour saturation line is curved and a decreasing pressure leads to a decreased enthalpy at the vapour saturation line. In such, as the process through the valve is assumed isenthalpic, a greater throttling through the valve leads to a greater enthalpy difference between the isenthalp (State 1–3) and the vapour saturation line.

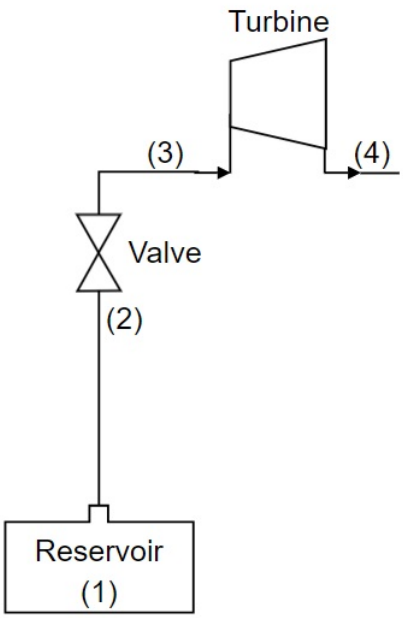

Figure 4.11: Schematic for Model I, containing one valve and one turbine. States 3–4 are determined by a developed script in EES which considers the limitations and specifications stated in Section 4.3.1. State 1 is the condition of the reservoir (Table 2.6) and state 2 is the state at the wellhead previously determined by the use of the developed TEPP program.

Thus, as the turbine is set to expand isentropically down to the vapour saturation line, a further throttling leads to a greater power output as a greater enthalpy difference through the valve is achieved (Eq.4.6). As such, the optimized value is achieved when the valve operates in such a manner that the outlet pressure from the turbine achieves the lower limit of 0.2 bar.

Still, this would be a very inefficient utilization of the energy contained in the steam, as the steam is throttled by approximately 157 bar which is not used to extract energy. First of all, such a large throttling process could prove difficult, but most importantly, the pressure energy should certainly be exploited more efficiently. However, considering the Model, a power output from the turbine of 23.83 (MW) is achieved, as presented in Table 4.4. It should be pointed out that the lines in Figure 4.12 are plotted linearly between the calculated points, which also applies to the corresponding plots for the other models. During the expansion through the turbine, the correct plot would involve a curved line between the inlet and outlet (State 3–4), as demonstrated in Figure 4.8.

Expanding beyond the vapour saturation line

To explore the potential of allowing the steam go beyond the saturated vapour curve, two further calculations were performed in EES, letting the real exiting steam from the turbine (i.e. state 4) obtain a vapour quality of 1.0 and 0.85. Vapour quality is the mass fraction in a saturated mixture

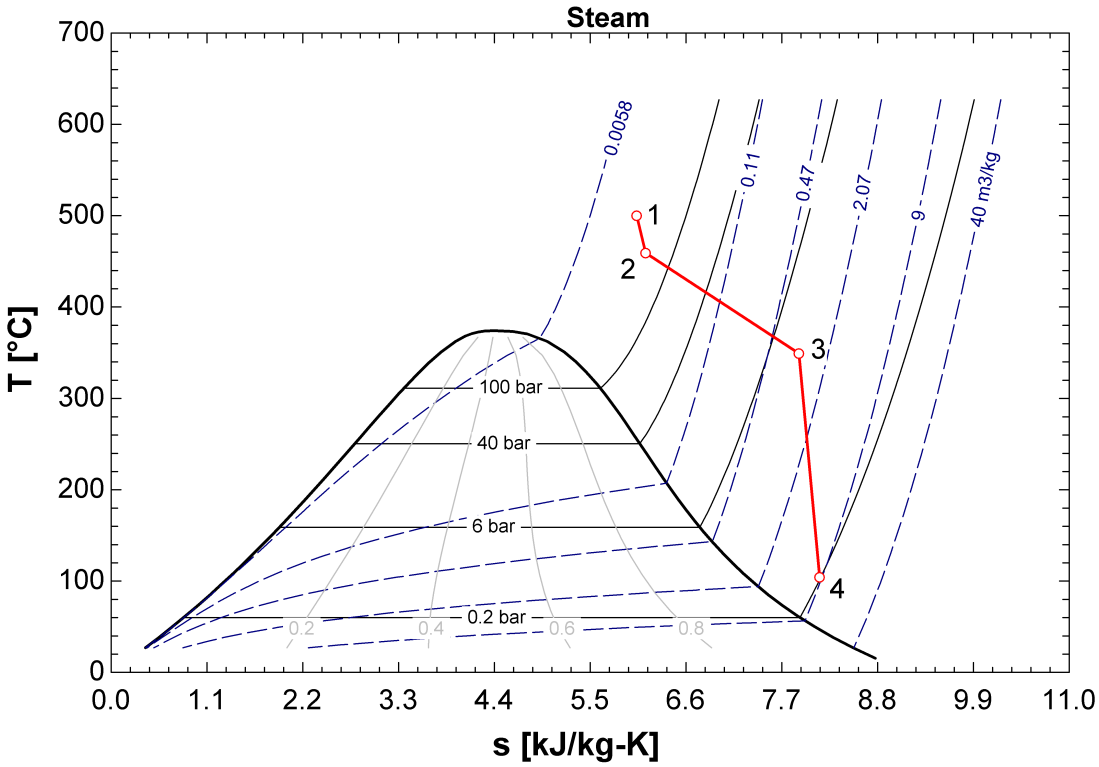

Figure 4.12: Temperature-entropy diagram for Model I as sketched in Figure 4.11 with calculated thermodynamic properties in Table 4.3.

that is vapour, i.e. saturated vapour has a quality of 1.0, and saturated liquid has a quality of 0.

The results from letting the steam expand to the vapour saturation line (i.e. χ_4=1.0), including Table of properties, T-s diagram and P-h diagram are available in Table D.1, Figure D.2 and Figure D.3, respectively. As may be observed from these figures, the outlet steam from the turbine is at the saturated vapour curve, and thus, chemical compounds which may be contained in the steam could condensate and result in corrosion to steam turbine components. If the composition of the fluid is similar to that obtained in Table 2.6, even small amount of condensation could lead to severe corrosion issues as the composition contain great amounts of corrodents, including chloride, sodium and sulphate. Still, by allowing the steam to expand to the vapour saturation line, the total power output is increased to 28.06 MW, an increase of 4.23 MW compared to isentropic expansion down to to the vapour saturation line as previously presented.

Results from allowing the steam to expand beyond the vapour saturation line (i.e. χ_4=0.85), including Table of properties, T-s diagram and P-h diagram, are available in Table D.2, Figure D.4 and Figure D.5, respectively. This process would lead to condensation of the steam inside the turbine, and such a process should only be carried out if the steam entering the turbine contain very small or zero amounts of corrodents. If the composition of the steam is similar

to that obtained in Table 2.6, the turbine would be exposed to corrosion mechanisms such as corrosion fatigue, pitting, stress corrosion cracking and erosion-corrosion. Thus, allowing the steam to go beyond the vapour saturation line with the fluid composition in Table 2.6 should not be performed without an effective separation system. However, the potential of achieving a vapour quality of 0.85 at the turbine exhaust for Model I provides a total power output of 45.65 MW (Table 4.4). Which is an increase of 21.82 MW, almost doubling, the power output compared to the isentropic expansion down to the vapour saturation line, as first presented for Model I.

For future reference, Model I is the model in Figure 4.12, as the subsequent models are analyzed in the same manner.

Table 4.4: Total power output from Model I with different vapour quality for the steam at the turbine exhaust.

Vapour quality (State 4) Model I	**Total Power Output (MW)**
Superheated	23.83
$\chi = 1$	28.06
$\chi = 0.85$	45.65

4.4.2 Model II: Double valve-turbine system

The schematics for the design of Model II is presented in Figure 4.13, which includes two valves and two turbines. In this design, the two variables which are to be determined are the outlet pressures from the 1st and 2nd valve. A plot of the resulting process in a T-s diagram is available in Figure.4.14 and thermodynamic properties at the different states of the process are available in Table 4.5.

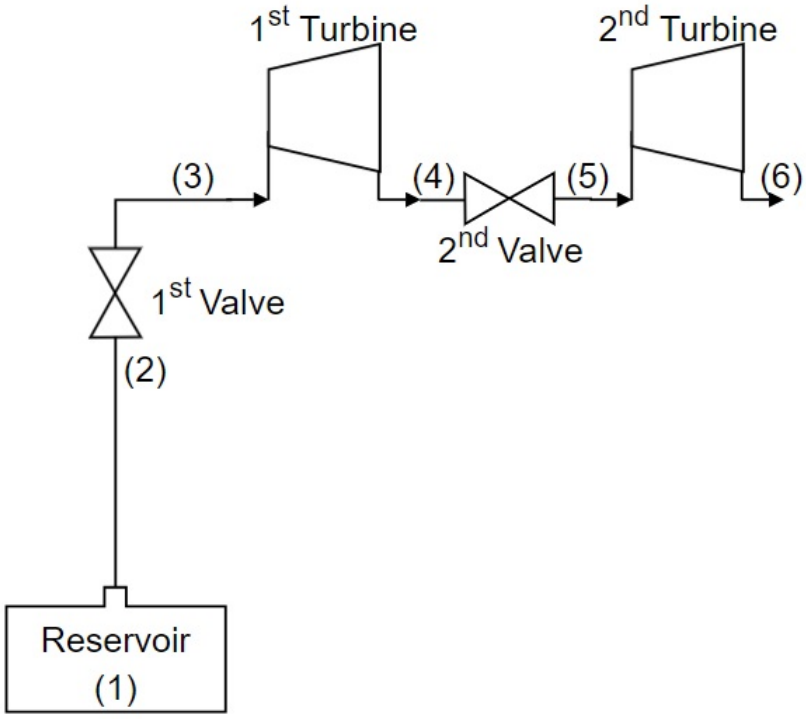

Figure 4.13: Schematic for Model II, containing two valves and two turbines. States 3–6 are determined by a developed script in EES which considers the limitations and specifications described in Section 4.3.1. State 1 is the condition of the reservoir (Table 2.6) and state 2 is the state at the wellhead previously determined by the use of the developed TEPP program.

Model II has a total power output of 26.33 MW (Table 4.6), which is 2.5 MW greater than Model I. By the use of EES, the exiting pressures from the first and second valve are calculated to 50 (State 3) and 0.73 bar (State 5), respectively. This implies a pressure difference of 110 bar through the first valve, which as in Model I, is a great reduction of pressure which could be utilized more efficiently, further discussed in Section 4.6. However, the steam is throttled less than in Model I, which indicates that Model II utilizes the pressure energy contained in the wellhead steam in a more efficient manner, compared to Model I. Still, this would prove an additional cost of installing and maintaining an additional turbine, which is a concern of power plant optimization, further discussed in Section 4.6.

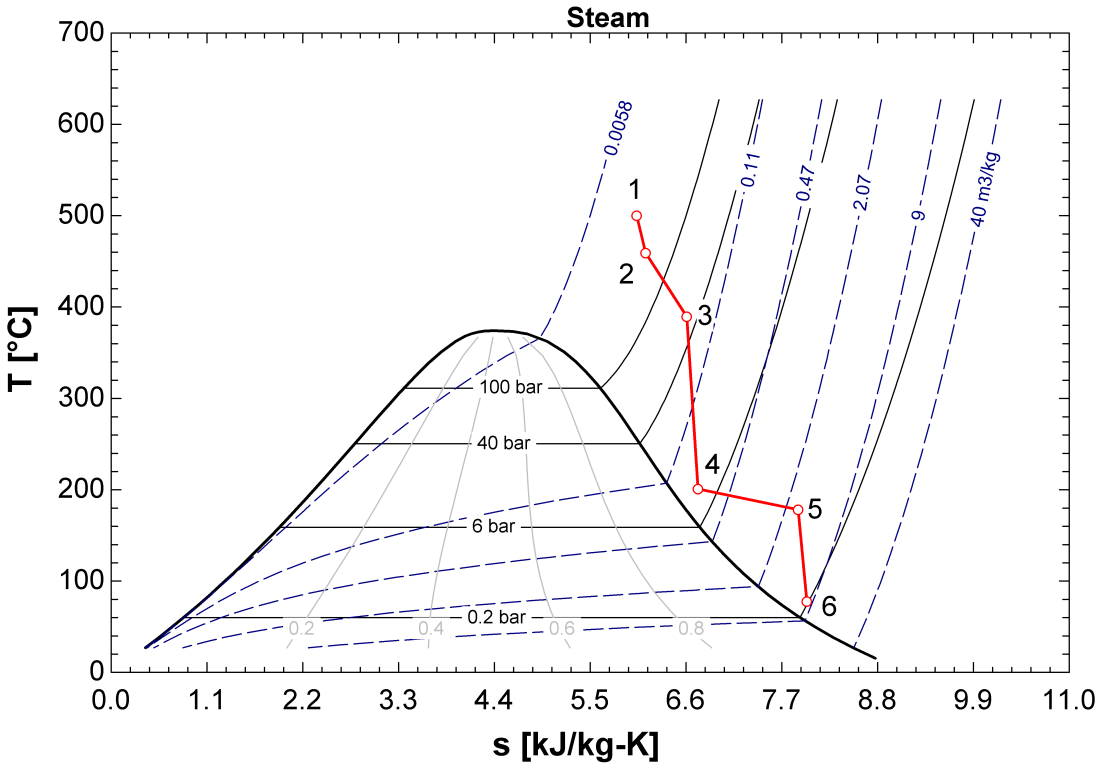

Figure 4.14: Temperature-entropy diagram for Model II as sketched in Figure 4.13 with calculated thermodynamic properties in Table 4.5

Table 4.5: Thermodynamic properties at each state of Model II, calculated with the developed EES script, available in Appendix C.2. Schematic available in Figure 4.13.

State	h (kJ/kg)	$\dot{m}$ (kg/s)	P (bar)	s (kJ/kg-K)	T (°C)	P_{is} (bar)	T_{is} (°C)
1	3197	50	230	6.04	500		
2	3171	50	160	6.14	459.2		
3	3171	50	50	6.61	389.5		
4	2834	50	9.34	6.74	200.7	9.34	176.9
5	2834	50	0.73	7.89	178.2		
6	2644	50	0.21	7.99	78.2	0.21	61.2

Table 4.6: Power output from each of the turbines present in Model II (Fig. 4.13) along with the total power output from the system.

Turbine nr.	Power Output(MW)
1	16.84
2	9.49
Total	**26.33**

4.4.3 Model III: Triple valve-turbine system

The schematics for the design of Model III which includes three valves and three turbines is presented in Figure 4.15, the calculated thermodynamic properties at each stage are presented in Table 4.8 and a thermodynamic plot of the process in a T-s diagram is available in Figure 4.16.

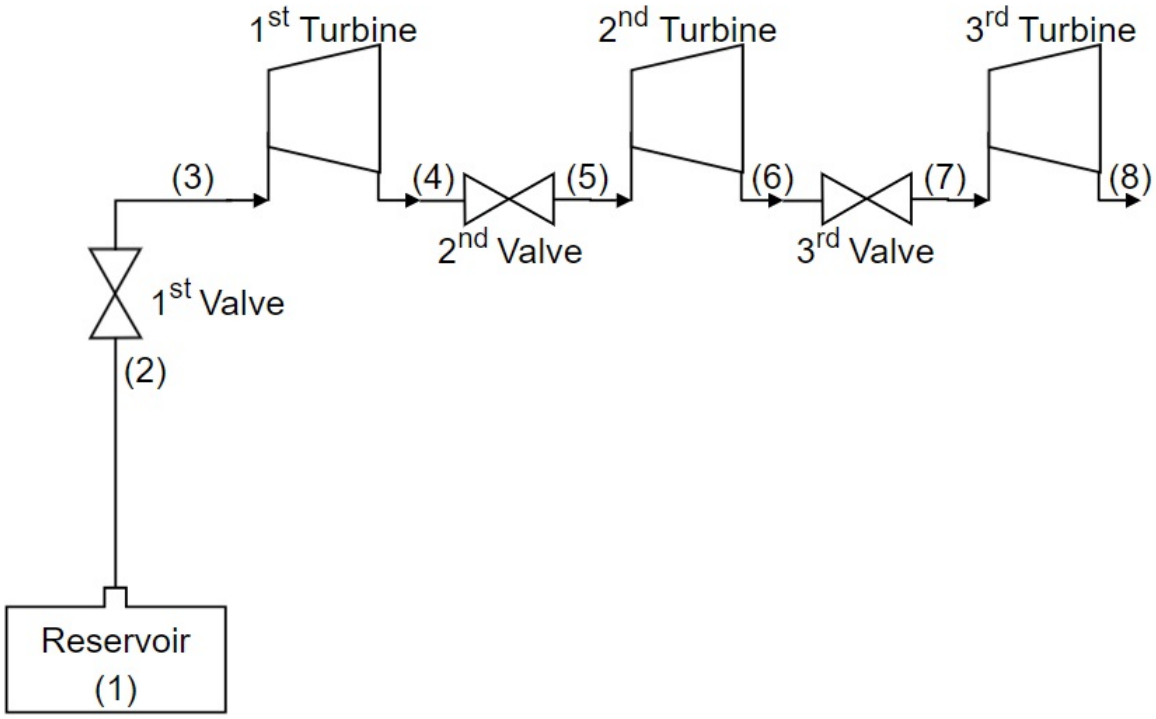

Figure 4.15: Schematic for Model III, containing three valves and three turbines. States 3–8 are determined by a developed script in EES (Appendix C.3) which considers the limitations and specifications described in Section 4.3.1. State 1 is the condition of the reservoir (Table 2.6) and state 2 is the state at the wellhead previously determined by the use of the developed TEPP program.

The outlet pressures from the valves is calculated to 63.28, 1.366 and 0.3 bar for the 1st, 2nd and 3rd valve, respectively. Power output from each of the turbines present in this design is available in Table 4.7, resulting in a total power output of 26.47 MW. It may seem odd that even at the presence of three turbines, the steam is throttled by 96.27 bar through the first valve and that the third turbine is almost unused. This may be a result of two factors. First of all, it may be that the script developed in EES was not able to find the optimal values for the exiting valve pressures and corresponding maximum power output from the system. However, this seems unlikely as Model III was analyzed thoroughly. As such, the calculated optimized values is justified as following. Consider Figure D.7, which is a P-h diagram for Model III, the two-phase envelope is curved and nonlinear at pressures greater than approximately 10 bar. As discussed for Model I, this characteristics leads to a greater enthalpy difference through the turbine, and

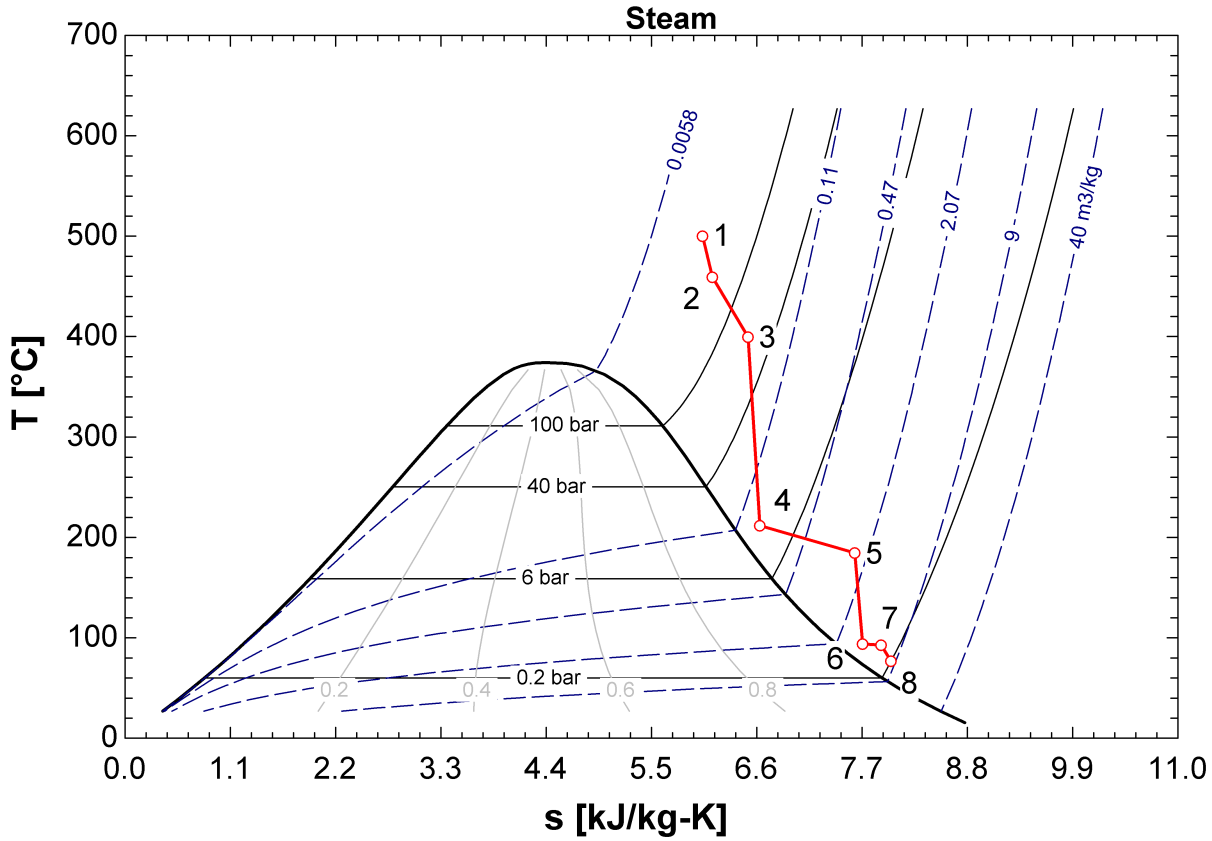

Figure 4.16: Temperature-entropy diagram for Model III as sketched in Figure 4.15 with calculated thermodynamic properties in Table 4.8.

thus a greater power output, as the valve throttle to a lower pressure. The script in EES calculated the characteristic for Model III as presented in Table 4.8 to be optimal. Even though the third turbine only delivers 1.49 MW of power (Table 4.7), it causes Model III to have a total power output which is 0.14 MW greater than Model II. The throttling of 96.27 bar through the first valve seems excessive and further discussed in Section 4.6.

Table 4.7: Power output from each of the turbines present in Model III (Fig. 4.15) along with the total power output from the system.

Turbine nr.	**Power Output (MW)**
1	16.39
2	8.59
3	1.49
Total	**26.47**

Table 4.8: Thermodynamic properties at each state of Model III, calculated with the developed EES script, available in Appendix C.3. Schematic available in Figure 4.15.

State	h (kJ/kg)	$\dot{m}$ (kg/s)	P (bar)	s (kJ/kg-K)	T (°C)	P_{is} (bar)	T_{is} (°C)
1	3197	50	230	6.04	500		
2	3171	50	160	6.14	459.2		
3	3171	50	63	6.51	399.4		
4	2843	50	12.43	6.63	211.5	12.43	189.6
5	2843	50	1.37	7.62	184.4		
6	2671	50	0.46	7.71	93.9	0.46	79.0
7	2671	50	0.30	7.90	92.8		
8	2641	50	0.20	8.00	76.6	0.20	60.1

4.4.4 Model IV: Single heat exchanger - Double turbine system

The schematics for the design of Model IV is presented in Figure 4.17, which includes one valve, one heat exchanger and two turbines. In this system, the only degree of freedom which is to be determined by the script developed in EES (Appendix C.4), is the outlet valve pressure. The optimization process is presented in Section 4.3.3. A plot of the resulting process in a T-s diagram is available in Figure.4.18 and thermodynamic properties at the different states available in Table 4.9.

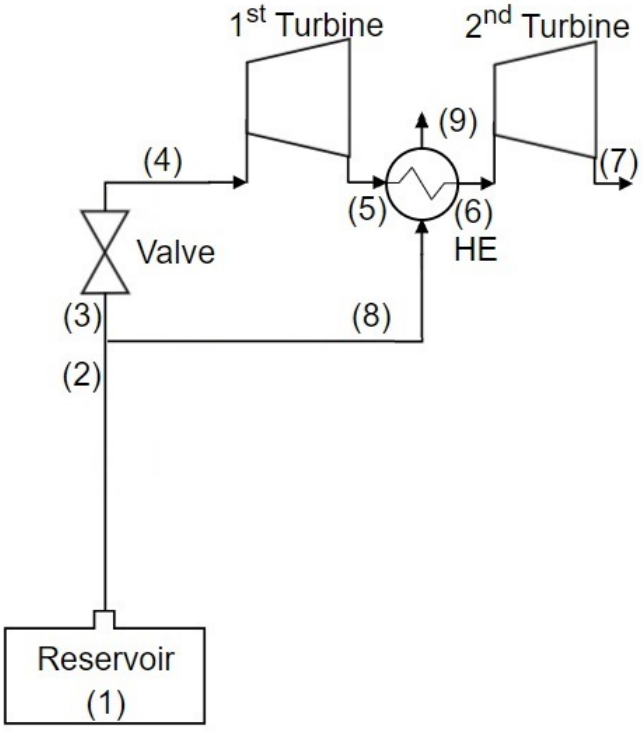

Figure 4.17: Schematic for Model IV, containing one valve, one heat exchanger and two turbines. States 3–9 are determined by a developed script in EES in addition to the limitations and specifications previously described. State 1 is the condition of the reservoir and state 2 is the state at the wellhead, previously determined by the use of the developed TEPP program.

The calculated power output from this system is 34.09 MW (Table 4.10) which is 7.62 MW greater than that achieved by Model III. It should be pointed out that the plotted line between state 8 and state 9 in the T-s diagram in Figure 4.18 is not accurate. As state 8 is the inlet of the hot steam going through the heat exchanger and State 9 is the corresponding outlet, and the fact that the process through the device is assumed isobaric, the process should follow the isobar of 160 bar from state 8 to state 9. As such, the heat exchanger in this system is exposed to 160 bar, and thus, a heat exchanger which can handle such pressures has to be utilized. The main reason that this Model proves a greater efficiency compared to the previously presented models, is the condensation process through the heat exchanger. Consider the process in the

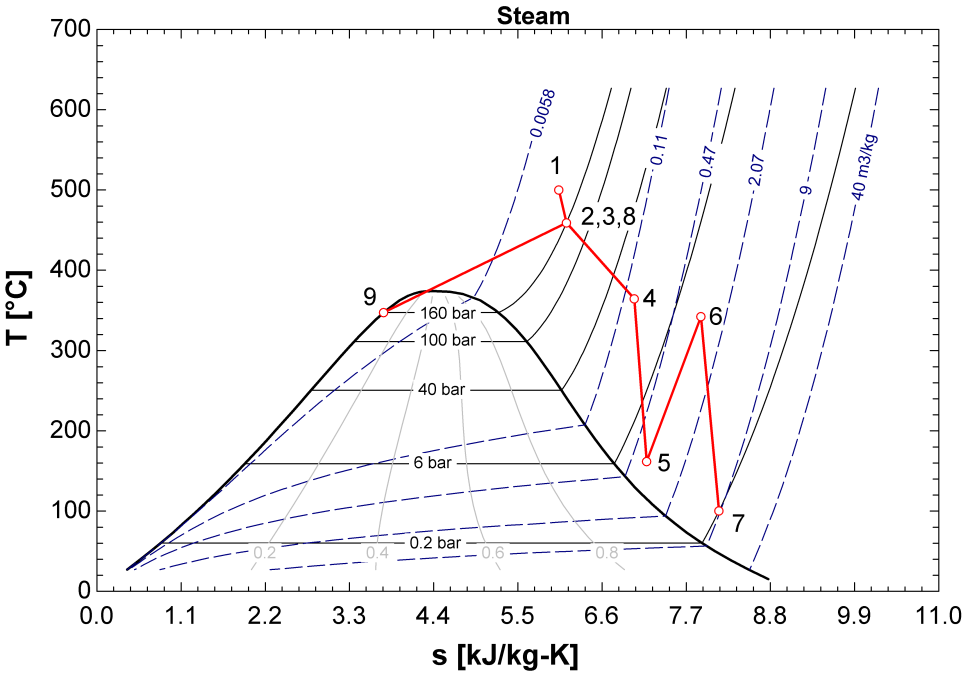

Figure 4.18: Temperature-entropy diagram for Model IV as sketched in Figure 4.17 with calculated thermodynamic properties in Table 4.9

P-h diagram in Figure D.8, the energy from the hot steam is extracted by condensing the steam from state 8 to state 9 and transferred to the power generation steam (State 5 to state 6) in the heat exchanger. Thus, by the use of the heat exchanger, the energy contained in the steam is utilized more efficiently. However, this assumes that the heat exchanger is able to comprehend the condensation which occurs. This would surely not be the case if the steam contained in the reservoir is similar to that presented in Table 2.6, which contain a significant number of minerals which could be subjected to deposition and scaling as temperature decreases, where silica, antimony- and arsenic sulphides are the most common in heat exchangers (Brown and Rock, 2010). Deposition and scaling problems within heat exchangers in geothermal power plants is mainly prevented in the design stage of the plant, where a limitation is set on the outlet temperature of the heat exchangers, limiting deposition to manageable levels. Still, this limit would result in a lower efficiency of the heat exchanger. Therefore, some binary geothermal power plant systems use antiscalant chemicals to minimise deposits, allowing further reduction of temperature, and thus, a greater heat exchanger efficiency (Richardson et al., 2015). However, problems related to deposition, scaling and corrosion in the heat exchanger is not addressed in this paper, as the main purpose is to examine the potential of the different models and a tool for addressing these issues could not be attained. Still, there is no doubt that these effects should be considered in further development of the models.

As may be observed from Table 4.9, the calculations in EES resulted in a mass flow rate

through the hot flow in the heat exchanger (State 8) to be 6.94 kg/s. Thus, by allowing 13.88% of the initial steam to reheat the steam after the first turbine, an increased power output of 7.76 MW is obtained compared to the direct system in Model II with two turbines.

Table 4.9: Thermodynamic properties at each state of Model IV, calculated with the developed EES script, available in Appendix C.4. Schematic available in Figure 4.17.

State	h (kJ/kg)	$\dot{m}$ (kg/s)	P (bar)	s (kJ/kg-K)	T (°C)	P_{is} (bar)	T_{is} (°C)
1	3197	50.00	230	6.04	500		
2	3171	50.00	160	6.14	459.2		
3	3171	40.25	160	6.14	459.2		
4	3171	40.25	19.54	7.02	364.4		
5	2788	40.25	2.75	7.18	161.8	2.75	130.6
6	3157	40.25	2.75	7.89	342.3		
7	2692	40.25	0.21	8.12	103.1	0.21	61.01
8	3171	9.75	160	6.14	459.2		
9	1649	9.75	160	3.75	347.3		

Table 4.10: Power output from each of the turbines present in Model IV (Fig. 4.17) along with the total power output from the system.

Turbine nr.	Power Output (MW)
1	15.39
2	18.70
Total	**34.09**

4.4.5 Model V: Double heat exchanger - Triple turbine system

The schematics for the design of Model V is presented in Figure 4.19, which includes one valve, two heat exchangers and three turbines. In this system, the only degree of freedom which is to be determined by the script developed in EES (Appendix C.4), is the outlet valve pressure. A plot of the resulting process in a T-s diagram is available in Figure.4.20 and thermodynamic properties at the different states, available in Table 4.12.

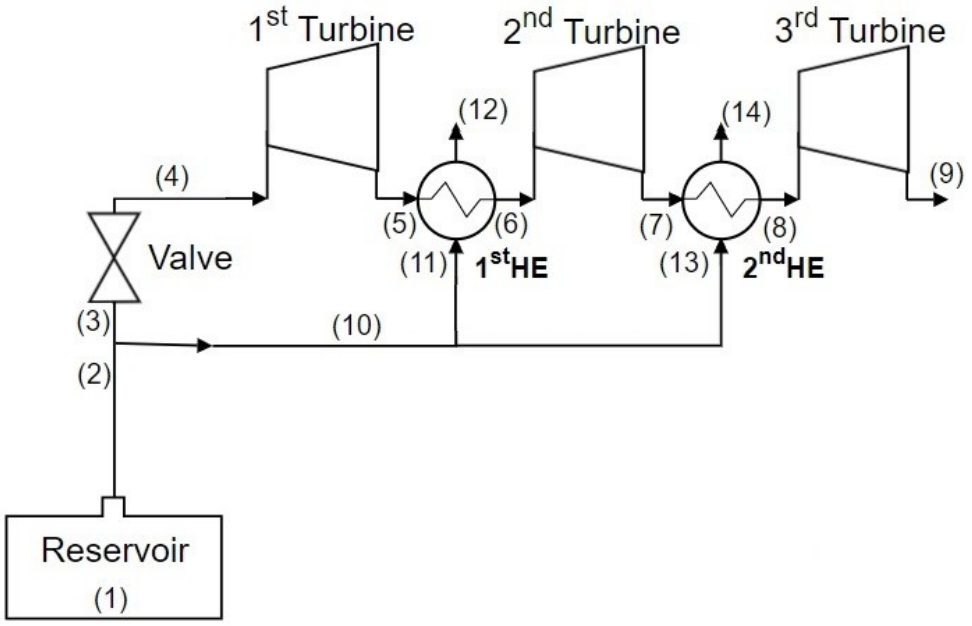

Figure 4.19: Schematic for Model V, containing two valves, two heat exchangers and three turbines. States 3–14 are determined by a developed script in EES in addition to the limitations and specifications previously described. State 1 is the condition of the reservoir and state 2 is the state at the wellhead, previously determined by the use of the developed TEPP program.

The total power output for this system is calculate to 39.56 MW, which is 5.47 MW greater than that of Model IV. In this Model, the steam at the wellhead (State 2) is first split into two, the steam going through the power production cycle (State 3) and the steam going to the two heat exchangers (State 10). The steam going through state 10 is subsequently split to the two heat exchangers. The fraction of mass flow rate going through each section is calculated by an optimization procedure, as described in Section 4.3.3. As may be observed from Table 4.12, 6.38 kg/s and 8.63 kg/s is led through the first and second heat exchanger, respectively. Thus, 35 kg/s goes through the power production cycle (State 3 to state 9). As stated in the limitations and specifications in Section 4.3.1, it is assumed that the heat exchanger manage to obtain a temperature on the cold exiting steam (State 12 and state 14) which is 5 °C below the exiting hot steam temperature (State 11 and state 13). This may be observed from the T-s diagram in

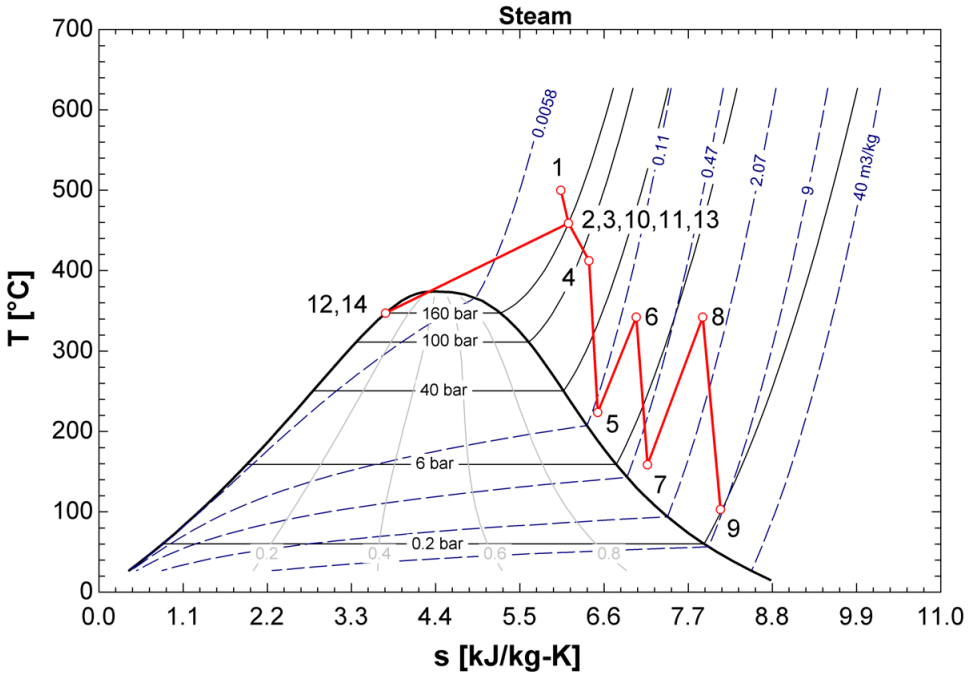

Figure 4.20: Temperature-entropy diagram for Model V as sketched in Figure 4.19 with calculated thermodynamic properties in Table 4.12

Figure.4.20, where the steam going through the power cycle is lifted to 343.3 °C at the exit of both heat exchangers. Due to this condition, the mass flow rate at state 13 is larger than at state 11 (Fig.4.19), as the second heat exchanger needs to transfer more energy to obtain the set temperature. As discussed for Model IV, the heat exchangers are subjected to condensate from the reheating steam as may be observed from the P-h diagram of the process in Figure D.9. As the same concern applies to this model, the discussion previously presented for Model IV will not be repeated here (See Section 4.4.4).

Table 4.11: Power output from each of the turbines present in Model IV (Fig. 4.19) along with the total power output from the system.

Turbine nr.	**Power Output (MW)**
1	11.20
2	12.10
3	16.26
Total	**39.56**

Table 4.12: Thermodynamic properties at each state of Model V, calculated with the developed EES script, available in Appendix C.5. Schematic available in Figure 4.19.

State	h (kJ/kg)	$\dot{m}$ (kg/s)	P (bar)	s (kJ/kg-K)	T (°C)	P_{is} (bar)	T_{is} (°C)
1	3197	50	230	6.035	500		
2	3171	50	160	6.136	459.2		
3	3171	35	160	6.136	459.2		
4	3171	35	81.64	6.403	412.4		
5	2851	35	16.75	6.519	223.7	16.75	203.6
6	3128	35	16.75	7.021	342.3		
7	2782	35	2.75	7.167	158.8	2.75	130.5
8	3157	35	2.75	7.891	342.3		
9	2692	35	0.21	8.122	103.2	0.21	61.0
10	3171	15	160	6.136	459.2		
11	3171	6.38	160	6.136	459.2		
12	1649	6.38	160	3.745	347.3		
13	3171	8.63	160	6.136	459.2		
14	1649	8.63	160	3.745	347.3		

4.5 Case Study - Power Production - Characteristics

The energy conversion efficiency is of significant importance for resource estimation studies during the early pre-feasibility and feasibility stages of the development and when calculating the power potential of newly drilled geothermal wells. The energy conversion efficiency in this paper is defined as the ratio of net electric power generated (MW_e) to the geothermal heat energy input from the reservoir (MW_{th})

$$\eta(\%) = \frac{\dot{W}_e}{\dot{m} \cdot h} \cdot 100 \tag{4.11}$$

where $\dot{W}_e$ is the running capacity (kW_e), $\dot{m}$ is the total mass flow rate (kg/s), and h is the reservoir enthalpy (kJ/kg).

As the power output from the models is presented as the power output from the turbines, a generator efficiency is determined the electric power generated by the models. Generally, the generator efficiency increase with the size of the generator and for the size of the geothermal plant. For geothermal power plants, the generator efficiency commonly ranges from 95.7 to 98.7% (Zarrouk and Moon, 2014). For the case study in this paper, the generator efficiency, η_g, is set to 97%. The electrical power output may be expressed as

Table 4.13: Efficiencies of the geothermal power plant systems evaluated in this study. Along with turbine power output ($\dot{W}$) and electrical power output ($\dot{W}_e$) from the models.

Model	$\dot{W}(MW)$	$\dot{W}_e(MWe)$	Efficiency total system(%)	Efficiency Power Plant (%)
I	23.83	23.11	14.46	14.58
I ($\chi = 1.0$)	28.06	27.22	17.03	17.17
I ($\chi = 0.85$)	45.65	44.28	27.70	27.93
II	26.33	25.54	15.98	16.11
III	26.47	25.68	16.06	16.19
IV	34.09	33.07	20.69	20.86
V	39.56	38.37	24	24.20

$$\dot{W}_e = \eta_g \cdot \dot{W} \tag{4.12}$$

Where $\dot{W}$ is the power delivered from the turbines for the models, as presented in Tables.4.4–4.11.

By the use of Eq.4.11 and Eq.4.12, the efficiency for the models in the case study may be calculated, and are presented in Table 4.13. To examine the efficiency of only the electric power plant, the enthalpy at the wellhead was used in Eq.4.12, while in evaluating the whole system from the reservoir to electrical production, the enthalpy in the reservoir was used. As may be observed, the largest total efficiency was obtained for Model I with an outlet vapour quality from the turbine of 0.85 (i.e. $\chi = 0.85$). However, as discussed in Section 4.4.1, this would imply that the fluid entering the turbine has to be pure, which is not the case if the chemical composition in Table 2.6 is considered. Thus, the model which is not exposed to the vapour saturation line which proves the highest efficiency, is Model V, containing two heat exchangers and two turbines, with a total efficiency of 24%.

The efficiencies of the geothermal power plant systems evaluated in this paper as shown in Table 4.13 may seem low for being a thermal power plant. However, geothermal power plants generally have lower efficiency relative to other thermal power plants, such as coal, natural gas, oil, and nuclear power stations (Fig. 4.21). The main reason that geothermal power plants have a lower efficiency compared to other thermal power plants, is that geothermal fluids do not reach the high temperatures of steam from boilers. Still, system efficiency does not materially affect operational costs as it would for plants that use fuel, but it does affect return on the capital used to build the plant (Zarrouk and Moon, 2014).

As of 2014, the highest reported conversion efficiency for a geothermal power plant was approximately 21% at the Darajat vapour-dominated system, with a worldwide efficiency average of approximately 12% (Zarrouk and Moon, 2014).

Considering the commonly low efficiency for geothermal power plants, the reservoir in the case study of this paper shows promising. However, at least two considerations may be

argued that the efficiencies presented are misleading. First of all, this case study idealizes the geothermal power production in several ways, as presented throughout the chapter. This idealization would certainly demonstrate that the real geothermal power plant for these conditions would result in a lower efficiency, as the energy conversion efficiencies are affected by many parameters which are not considered in this study, including gas content, size, parasitic load, ambient conditions and dissolved minerals content (Zarrouk and Moon, 2014). However, the models presented are quite simple and could certainly be developed to utilize the available energy in a more efficient process.

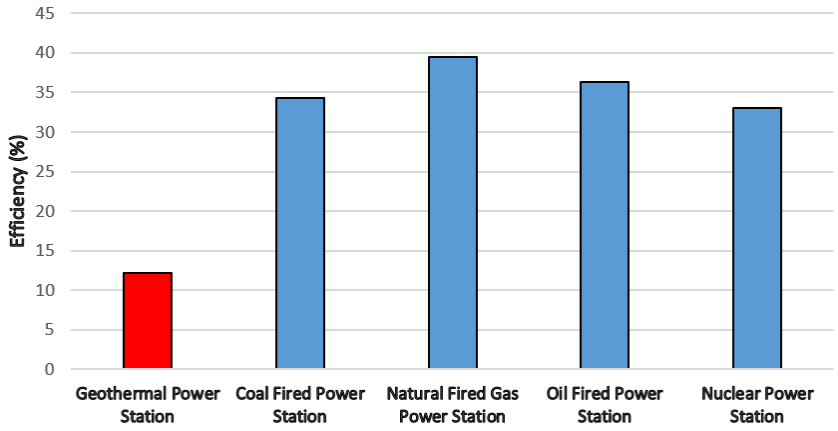

Figure 4.21: Thermal power plant efficiency by category. Adapted from Zarrouk and Moon (2014).

The electrical power output from Model V is calculated to 38.37 MW_e which is considerable considering geothermal energy extraction. Geothermal power plant systems are usually complex and commonly characterized by the total power output from the geothermal power complex. As an example, The Geysers Complex situated north of San Fransisco in the United States contain 22 plants that draw steam from over 350 wells, producing a combined 1 517 megawatts of power (Atwell, 2018). In such, comparing the results of this paper with geothermal power plants which draw steam from up to several wells did not seem accurate, as the models presented only draws fluid from one reservoir. However, during the flow tests of IDDP-1 as described in Section 2, the well showed a potential to generate between 25 and 35 MWe of electricity (Elders et al., 2014). As such, by comparing the results from Model V, it shows a potential of 3.37 MWe greater than the anticipated maximum for IDDP-1. Still, as mentioned previously, the potential of the conditions examined may be larger or smaller, depending on the losses not taken into account and the further development of the plant.

$$\text{Capacity Factor} = \frac{\text{Actual Energy Generated (MWh)}}{\text{Installed Capacity (MW)} \cdot \text{Time Period (h)}} \tag{4.13}$$

Following is a prediction on the predicted energy production for Model V, in such, the capacity factor for the plant needs to be estimated. The capacity factor of geothermal power

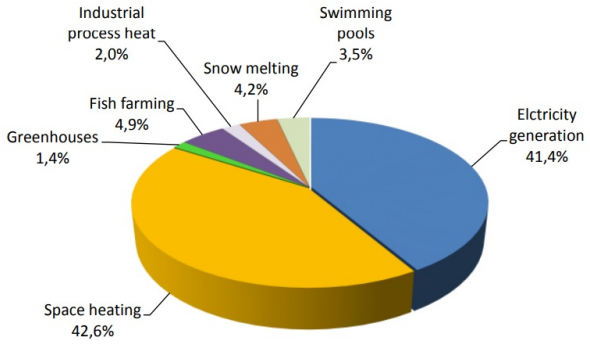

	Installed power	Energy consumption	
	MW	TJ/year	GWh/year
Space heating	1,550	19,400	5,389
Greenhouses	45	660	183
Fish farming	85	2,230	619
Industrial process heat	70	910	253
Snow melting	195	1,900	528
Swimming pools	90	1,600	444
Direct uses total	2,035	26,700	7,417
Elctricity generation	663	18,882	5,245
Geothermal utilization total	2,698	45,582	12,662

Figure 4.22: Geothermal utilization in Iceland 2014 (Ragnarsson, 2015)

plants depends on the mix of power plants serving the electricity grid. Where geothermal power plants can be operated as base load, the capacity factor is usually in excess of 0.9 (Stefansson, 2002). In 2014, Iceland had an installed power of 663 MW_e from geothermal resources for electricity generation, with a corresponding energy consumption from the electrical generation of 5 245 Gwh/year (Fig. 4.22). By the use of Eq.4.13, the capacity factor for electricity generation in Iceland in 2014 is calculated to 90.3%. Thus, by assuming a capacity factor of 90.3% for Model V, where the installed capacity is 38.37 MWe (Table 4.13), the predicted energy production from the power plant is 302.5 GWh/year. This would be 5.77% of the geothermal energy produced in Iceland in 2014 (Fig.4.22).

4.6 Case Study - Power Production - Discussion

This chapter presents some discussion on the calculations regarding geothermal electricity generation from the available steam conditions at the wellhead, previously calculated with the developed TEPP program. The method used for examining the geothermal power plants in this study assumes that the models operate at close to ideal conditions to explore the potential of geothermal exploitation from a supercritical reservoir. As a result, this chapter aims to discuss the most important aspects which should be considered to evaluate the system in a more realistic manner, beyond what is previously discussed.

As evaluated in Section.4.4.4, the heat exchangers analyzed in this study are exposed to condensation, and the corresponding effect of the geothermal fluid on the device should be addressed in the design process. The heat exchanger is essentially assumed ideal, and an optimization between efficiency and size regarding the device should be evaluated. In addition, the heat exchangers are assumed to be capable of handling the high-pressure fluid of 160 bar available at the wellhead, which proves another factor of consideration.

As this study aims to explore the potential of energy utilization from the available resource, mineral depositions and corrosion issues are not considered. The fluid composition of the reservoir (Table 2.6) contains several significant compounds which are subjected to precipitation. In such, a purification of the fluid is necessary prior to the power generation cycle, which will diminish the efficiency of the plant.

The models should be developed to utilize the available pressure more efficiently, as the throttling through the first valve in all the models evaluated is excessive. A better development of the models could result in a better utilization of the geothermal energy contained in the fluid. However, further detailed engineering could result in design issues which are not considered in this study. In addition, the cost of development is not considered, which will play a major part in choosing a solution. The temperature of the fluid exiting the models from the last turbine contains a temperature between 78.2 °C and 104.1 °C which could be used for direct uses, including space heating, industrial process heat and snow melting to increase the efficiency of the system (Fig. 4.22). As observed from the further implementation of devices in the case study, from the simplest system (Model I) to the most complex system (Model V), the energy contained in the steam is utilized more efficiently. Thus, by further developing the systems, the energy utilization should prove more efficient. It should be pointed out that the increasing amount of turbines implemented in the models, does not necessarily lead to a more costly system. This is rather an optimization between the numbers and sizes of the units. As an example, even though Model I only has one turbine, this turbine is expected to deliver 23.83 MW, while the turbines present in Model II are expected to deliver 16.84 and 9.49 MW. Thus, the turbine in Model I has to be larger than the turbines in Model II, hence, a further analysis has to be achieved to determine which Model will prove the highest investment cost.

In the development of the models presented in this paper, several losses are neglected, including losses due to friction in pipes, size of components and heat loss. These losses would certainly prove as a diminisher for the efficiency of the geothermal power plant, and their effect remains to be determined. In developing the design of a geothermal power plant, an optimization between expenses and power output from the plant has to be determined to minimize the Levelized Cost of Electricity (LCOE).

4.7 Case Study - Power Production - Conclusion

Taking into account all the assumptions made for the case study, Model V (Section 4.4.5) proves most efficient, which includes two heat exchangers and three turbines. The total electrical power output from Model V was calculated to 38.37 MW_e with a total efficiency of 24% and a predicted energy production of 302.5 GWh/year. As an appropriate tool for calculating chemical phenomenon during extraction, which could diminish the efficiency of the power plant, could not be attained, these phenomenon should be addressed in further developments. As a result, the energy contained in the geothermal steam was exploited in such a manner that it was not exposed to condensation in the power generation cycle. Still, the heat exchangers are exposed for condensation, and the corresponding chemistry effect should be considered. Two considerations with opposite effect on the efficiency of the geothermal power plant have been presented. An increase in efficiency is expected in further development with adequate devices and a decrease in efficiency is expected if neglected losses are considered.

Chapter 5

Conclusions & Recommendations for Further Work

5.1 Conclusions

During this study, energy utilization from a deep geothermal source has been analyzed, including the establishment of the properties of a generic hydrothermal well, development of a methodology for calculating top-site conditions during extraction of the geothermal fluid and evaluating possible power cycle designs for electric power production.

A literature study on the geothermal fluid composition of deep geothermal wells situated in Iceland has carried out, demonstrating that the chemical composition of the fluid varies greatly at the different geothermal sites on Iceland. Based on these observations, the fluid composition of a generic hydrothermal well (referred to as the case study) has been obtained. The temperature and pressure of the case study were set to 500 °C and 230 bar based on the research.

In obtaining a methodology for calculating thermodynamic properties during extraction of geothermal fluids from deep geothermal wells to the geothermal power plant, two scripts, TEPP (v1.0) and TEPP (v2.0), have been developed in MATLAB. TEPP (v1.0) is the basic version which calculates temperature, enthalpy and pressure variations as a result of reservoir conditions and pipe parameters. The script was further developed to TEPP (v2.0) which calculates the same properties for a given range of mass flow rate. Both versions of TEPP is developed to provide fast calculations, allowing fast evaluations of extraction of geothermal fluids. Based on the conditions of the reservoir of the case study, a pressure drop of 70 bar and a temperature loss of 55 °C was calculated. In addition, it was observed that the condition of the case study was in the region where the temperature is dependent on both pressure and enthalpy of the fluid. As a result, for increasing mass flow rates, calculated temperature variations had a non-linear response. TEPP remains to be verified as experimental data could not be acquired

during this study, mainly due to the fact that temperature and pressure logs at these conditions are expensive and difficult as it requires equipment which could resist high pressures and temperatures as well as the chemical composition of the fluid. However, TEPP was compared to previously calculated data for a deep geothermal well. The comparison resulted in a 10% error regarding the outlet pressure between the methods in comparison and a 7.35% error regarding outlet temperature with an assumed overall heat transfer coefficient of three. Still, this comparison is not an accurate validation, concluding in that TEPP should be validated with experimental data when such information is obtained.

As a result of the calculations carried out by TEPP, five different models for electrical power production from the fluid available at the wellhead were evaluated by the development of five scripts in EES. An appropriate tool for calculating chemical equilibrium at the conditions in evaluation could not be acquired during this study. It was thus decided to avoid the two-phase envelope in the power generation cycle while analyzing the models. This was achieved by isentropic expansion of the steam to the vapour saturation line. However, two further analyzes were performed on Model I (which contained one valve and one turbine) to explore the potential of allowing the steam at the turbine exhaust to achieve a vapour quality of 1 and 0.85. Allowing a vapour steam quality of 0.85 for the fluid composition of the case study could result in severe damages to the turbine as it would be exposed to corrosion mechanisms such as corrosion fatigue, pitting, stress corrosion cracking and erosion-corrosion. Still, allowing such a process resulted in a total power output from the turbine of 45.65 MW, an increase of 21.82 MW compared to an isentropic expansion to the vapour saturation line. It is thus evident from this analysis that allowing power generation by condensing the steam in the turbine, for the conditions evaluated, has a great potential. However, the effect of condensation could no be addressed. The model which proved the highest potential for electric power generation where the steam at the exhaust of the turbine was slightly superheated, was Model V. This model was characterized by containing three turbines, two heat exchangers and three valves, resulting in a calculated electrical power output of 38.37 MW, a total efficiency of 24% and a predicted energy production of 302.5 GWh/year. As of 2014, the highest reported conversion efficiency for a geothermal power plant was approximately 21%, with a worldwide efficiency average of approximately 12%. As a result, the efficiency of Model V proves promising. Two considerations with opposite effect on the efficiency of the geothermal power plant have been discussed. An increase in efficiency is expected in further development with adequate devices and a decrease in efficiency is expected if neglected losses are considered.

Based on the research carried out in this paper along with the assumptions made, energy utilization from the deep geothermal source analyzed shows promising. If the geothermal power cycle in Model V could be realized with the given assumptions, it would be the most efficient geothermal power plant worldwide.

5.2 Recommendations for Further Work

This study aimed to explore the potential of electric power production from a deep geothermal source. It is probably evident from the report that exploitation of supercritical water proves some great challenges. With great challenges come great opportunities. Some suggestions for further work an research to overcome at least some of these follows.

5.2.1 Reservoir Chemistry

Developing technology that can with good estimate predict reservoir fluid chemistry, will allow geothermal power plant designers to significantly reduce the risk of scaling and corrosion in geothermal systems. These risks can further be minimized by developing simulation tools which predict precipitation of corrosive and depositing compounds, allowing the implementation of adequate measures.

5.2.2 Detailed Engineering

In evaluating the potential of the geothermal source in this study, several elements have been idealized. Accounting for more details in the system configuration would lead to a better approximation of the performance of the system. Including evaluation of different methods to utilize pressure (Like screw expanders instead of throttling valves), alternative methods for power utilization, addressing chemistry challenges and usage in district heating systems.

5.2.3 Chemical Equilibrium Calculations

Developing or attaining a method for calculating chemical equilibrium at superheated and supercritical conditions would ensure that issues related to precipitation and corrosion could be addressed. This would provide a wider foundation for decision makers to choose suitable geothermal power generation systems and prevent related issues in the design process. Further evaluations could be carried out regarding material selection and measures of treating the steam to avoid corrosive compounds. In addition, chemical equilibrium calculation could be utilized to determine supersaturation with regard to mineral precipitation in the different parts of the system. An evaluation of available data on reaction kinetics could determine where in the system precipitation would cause issues.

5.2.4 Cost Analysis

Performing a cost analysis of the suggested solutions should be performed to determine the LCOE of the systems, which would reveal if they are competitive with other sources of energy.

Bibliography

Ármannsson, H. (2001). Reaction of groundwater with rock from the krafla area, ne iceland and volcanic gas. *Water-Rock Interaction, Balkema, Swets & Zeitlinger, Lisse, The Netherlands*, pages 779–782.

Ármannsson, H., Fridriksson, T., Gudfinnsson, G. H., Ólafsson, M., Óskarsson, F., and Thorbjörnsson, D. (2014). Iddp—the chemistry of the iddp-01 well fluids in relation to the geochemistry of the krafla geothermal system. *Geothermics*, 49:66–75.

Ármannsson, H., Gudmundsson, A., and Steingrímsson, B. (1987). Exploration and development of the krafla geothermal area. *Jökull*, 37:13–30.

Arnórsson, S., Sigurdsson, S., and Svavarsson, H. (1982). The chemistry of geothermal waters in iceland. i. calculation of aqueous speciation from 0 to 370 c. *Geochimica et Cosmochimica Acta*, 46(9):1513–1532.

Atwell, C. (2018). The world's largest geothermal field: 22 power plants, more than 350 wells.

Barbier, E. (2002). Geothermal energy technology and current status: an overview. *Renewable and sustainable energy reviews*, 6(1-2):3–65.

Bazargan, M., Fraser, D., and Chatoorgan, V. (2005). Effect of buoyancy on heat transfer in supercritical water flow in a horizontal round tube. *Journal of heat transfer*, 127(8):897–902.

Bertani, R. (2016). Geothermal power generation in the world 2010–2014 update report. *Geothermics*, 60:31–43.

Bjarnason, I. T., Menke, W., Flóvenz, Ó. G., and Caress, D. (1993). Tomographic image of the mid-atlantic plate boundary in southwestern iceland. *Journal of Geophysical Research: Solid Earth*, 98(B4):6607–6622.

Boden, D. R. (2016). *Geologic Fundamentals of Geothermal Energy*. CRC Press.

Brown, K. and Rock, M. (2010). Test rig experiments for silica scaling inhibition. In *Proc. World Geothermal Congress*.

DiPippo, R. (2012). *Geothermal power plants: principles, applications, case studies and environmental impact*. Butterworth-Heinemann.

DiPippo, R. (2015). *Geothermal power plants: principles, applications, case studies and environmental impact*. Butterworth-Heinemann.

Driesner, T. (2007). The system h2o–nacl. part ii: Correlations for molar volume, enthalpy, and isobaric heat capacity from 0 to 1000 c, 1 to 5000 bar, and 0 to 1 xnacl. *Geochimica et Cosmochimica Acta*, 71(20):4902–4919.

Driesner, T. and Heinrich, C. A. (2007). The system h2o–nacl. part i: Correlation formulae for phase relations in temperature–pressure–composition space from 0 to 1000 c, 0 to 5000 bar, and 0 to 1 xnacl. *Geochimica et Cosmochimica Acta*, 71(20):4880–4901.

Einarsson, K., Sveinsson, K., Ingason, K., Kristjansson, V., and Holmgeirsson, S. (2015). Discharge testing of magma well iddp-1. In *Proceedings World Geothermal Congress*.

Elders, W., Friðleifsson, G., and Albertsson, A. (2014). Drilling into magma and the implications of the iceland deep drilling project (iddp) for high-temperature geothermal systems worldwide. *Geothermics*, 49:111–118.

Fournier, R. and Potter, R. (1982). Revised and expanded silica (quartz) geothermometer. *Bull., Geotherm. Resour. Counc.(Davis, Calif.);(United States)*, 11(10).

Fridleifsson, G. Ó., Ármannsson, H., Árnason, K., Bjarnason, I. Þ., and Gíslason, G. (2003). Part i: Geosciences and site selection. *Iceland Deep Drilling Project, Feasibility Report*, 2003:007.

Fridriksson, T., Stefánsson, A., Óskarsson, F., Eyjólfsdóttir, E., and Sigurdsson, Ó. (2015). Fluid chemistry scenarios anticipated for iddp-2 to be drilled in reykjanes, iceland. In *Melbourne: World Geothermal Congress*.

Friðleifsson, G., Elders, W., and Albertsson, A. (2014). The concept of the iceland deep drilling project. *Geothermics*, 49:2–8.

Friðleifsson, G. and Elders, W. A. (2017). The iceland deep drilling project geothermal well at reykjanes successfully reaches its supercritical target. *Geotherm Resour Counc Bull*, 46:30–33.

Friðleifsson, G. Ó. (2017). Grant agreement number 608553 image. *IMAGE*, 5:04.

Haaland, S. E. (1983). Simple and explicit formulas for the friction factor in turbulent pipe flow. *Journal of Fluids Engineering*, 105(1):89–90.

Hauksson, T., Markusson, S., Einarsson, K., Karlsdóttir, S. N., Einarsson, Á., Möller, A., and Sigmarsson, Þ. (2014). Pilot testing of handling the fluids from the iddp-1 exploratory geothermal well, krafla, ne iceland. *Geothermics*, 49:76–82.

Holmgren, M. (2006). X steam for matlab.

Ingason, K., Árnason, A. B., Bóasson, H. Á., Sverrisson, H., Sigurjónsson, K. Ö., and Gislason, Ţ. (2015). Iddp-2, well design. In *Proceedings World Geothermal Congress*.

Klein, S. A. and Nellis, G. (2013). *Mastering EES*. F-Chart Software.

Morey, G. W. and Hesselgesser, J. M. (1951). The solubility of some minerals in superheated steam at high pressures. *Economic Geology*, 46(8):821–835.

Nicholson, K. (1993). Geothermal fluids : chemistry and exploration techniques.

Næss, E. (2018). Personal communication.

Ommedal, D. (2017). Energy utilization from deep geothermal sources - project work.

Pálmason, G. (1971). *Crustal structure of Iceland from explosion seismology*, volume 40. Prentsmiðjan Leiftur.

Parkhurst, D. L., Appelo, C., et al. (1999). User's guide to phreeqc (version 2): A computer program for speciation, batch-reaction, one-dimensional transport, and inverse geochemical calculations.

Pioro, I. and Mokry, S. (2011). Thermophysical properties at critical and supercritical pressures. In *Heat Transfer-Theoretical Analysis, Experimental Investigations and Industrial Systems*. InTech.

Povarov, O., Tomarov, G., and Semenov, V. (2000). Physical and chemical processes of geothermal fluid impact on metal of geothermal power plant equipment. In *Proceedings of World Geothermal Congress 2000*.

Ragnarsson, Á. (2015). Geothermal development in iceland 2010-2014. 4(9).

Richardson, I., Addison, S., and Lawson, R. (2015). Chemistry challenges in geothermal power generation. *Power Plant Chem*, 1:1–17.

Schmidt, E. (1969). *Properties of Water and Steam in SI-units: KJ, Bar. 0-800° C. 0-1000 Bar*. Springer.

Spang, B. (2002). Water97_v13. xla–excel add-in for properties of water and steam in si-units. *Hamburg, Germany*.

Stefansson, V. (2002). Investment cost for geothermal power plants. *Geothermics*, 31(2):263–272.

Stefánsson, A. (2014). Geochemical assessment of the utilization of iddp1, krafla. http://gogn.lv.is/files/2014/2014-007.pdf. [Online; accessed 4-April-2018].

Tester, J. W., Anderson, B. J., Batchelor, A. S., Blackwell, D. D., DiPippo, R., Drake, E., Garnish, J., Livesay, B., Moore, M. C., Nichols, K., et al. (2006). The future of geothermal energy: Impact of enhanced geothermal systems (egs) on the united states in the 21st century. *Massachusetts Institute of Technology*, 209.

Thórhallsson, S., Pálsson, B., Hólmgeirsson, S., Ingason, K., Matthíasson, M., Bóasson, H., and Sverrisson, H. (2014). Well design for the iceland deep drilling project (iddp). *Geothermics*, 49:16–22.

Toth, A. (2017). Flow and heat transfer in geothermal systems : basic equations for describing and modeling geothermal phenomena and technologies.

Vision, G. and Mission, E. (2009). Geothermal tomorrow 08.

Yunus, A. C. and Cimbala, J. M. (2010). Fluid mechanics fundamentals and applications. *2nd ed. in SI units. ed., McGraw Hill Publication*.

Zarrouk, S. J. and Moon, H. (2014). Efficiency of geothermal power plants: A worldwide review. *Geothermics*, 51:142–153.

Zierenberg, R., Schiffman, P., Barfod, G., Lesher, C., Marks, N., Lowenstern, J. B., Mortensen, A., Pope, E. C., Bird, D., Reed, M., et al. (2013). Composition and origin of rhyolite melt intersected by drilling in the krafla geothermal field, iceland. *Contributions to Mineralogy and Petrology*, 165(2):327–347.

Zinsalo, J. M. and Lamarche, L. (2017). Electricity generation from deep geothermal energy. https://substance.etsmtl.ca/en/electricity-generation-from-deep-geothermal-energy [Online; accessed 20-January-2018].

Appendix A

Fluid Composition at Krafla

Table A.1: Calculated Aquifer fluid composition at Krafla (Stefánsson, 2014). Units are in ppm.

Well No.	KRA-01	KRA-02	KRA-04	KRA-05	KRA-06	KRA-08	KRA-09	KRA-10	KRA-11	KRA-12
t_{quartz}	267	264	245	277	295	212	233	243	209	234
Liquid phase										
pHT	7.13	6.49	6.97	7.03	6.84	6.97	6.78	6.86	6.97	7.17
SiO2	546	529	448	588	655	311	392	439	300	405
B	1.17	1.62	0.53	2.22	2.4	0.51	0.85	0.63	0.5	0.52
Na	110	157	220	122	203	172	196	148	173	183
K	17.45	25.66	34.32	21.79	36.4	13.99	21.74	19.69	15.2	24.19
Mg	0.008	0.003	0.005	0.003	0.006	0.033	0.005	0.002	0.02	0.015
Ca	0.23	0.69	2.59	0.57	1.12	2.31	2.97	1.14	2.6	2.32
Al	1.27	0.86	1.24	0.33	0.16	0.64	0.99	1.14	0.73	1.3
Fe	0.023	0.023	0.006	0.019	0.011	0.01	0.014	0.009	0.01	0.161
F	1.53	1.46	1.02	1.44	1.24	0.68	0.95	0.77	0.85	0.89
Cl	15.2	111	35.6	74.1	171	37.5	33.2	115	35.4	33.8
SO4	4.6	8.74	237	5.54	3.72	189	226	46.8	186	224
Vapour phase										
CO2	742	4226	433	927	4781	333	457	475	174	261
H2S	209	311	210	466	443	31	145	94	49	64
H2	6.86	13.49	3.88	13.12	18.91	0.07	4.87	1.9	0.32	0.72
CH4	0.42	1.01	0.19	0.13	0.74	0.69	0.14	1.97	0.48	0.45
N2	6.7	5.44	4.61	7.65	10.63	13.63	3.93	11.86	11.96	8.84

Appendix B

TEPP - Extraction of Geothermal Fluid - MATLAB Script

Following is the MatLab script developed to calculate temperature, enthalpy and pressure variations during extraction of hot geothermal fluids. The script is developed by Daniel Ommedal in co-operation with the Norwegian University of Science and Technology (NTNU). Purpose, limitations and validation regarding the program is discussed in chapter 3.

B.1 TEPP Basic Version v1.0 MatLab Script

```
%TEPP Basic Version (v1.0)
%% Input variables
T1_C=;          %Temperature in reservoir (degrees C)
P1=;            %Pressure in reservoir (Pa)
m_dot=;         %Massflow rate (kg/s)
L=;             %Length og pipe
D=;             %Diameter of production pipe section (m)
alfa=;          %Angle of pipe relative to horizontal direction (rad)
epsilon=;       %Pipe roughness (mm)
U=;             %Overall heat transfer coefficient (W/(m^2 K))
Temp_grad=;     %Temperature gradient(degrees/km)
N=;             %Number of iterations

%% Data
g=9.81;             %Gravitational constant(m/s^2)
M=18.015;           %Molecular weight water vapour(kg/kmol)
```

```
Ru=8314.472;        %Universal gas constant(J/(kmol*K))
R=Ru/M;             %Specific gas constant (J/(kg*K))
```

```
%% Calculations
dL=L/N;                                     %Iteration lenght (m)
epsilon=epsilon/1000;                       %Pipe roughness (m)
P1_bar=P1/(10.^5);                          %Pressure of reservoir (bar)
enthalpy_Res=XSteam('h_pt',P1_bar,T1_C);    %Enthalpy of reservoir (kJ/kg)
Rho1=XSteam('rho_ph',P1_bar,enthalpy_Res);%Density of reservoir (kg/m^3)
my=XSteam('my_pT',P1_bar,T1_C);             %Viscosity of reservoir (Pa*s)
V1=m_dot/(Rho1*(D/2).^2*pi);                %Velocity (m/s)
Re=Rho1*V1*D/my;                            %Reynolds number
fd2  = -1.8*log10((epsilon/(3.7*D))^1.11+6.9/Re);
fd=1/fd2^2;              %Darcy friction factor from Haaland fd2=1/sqrt(fd)
A_ht=pi*D*dL;            %Heat transfer surface (m^2)
Temp_grad_meter= Temp_grad/(1000);%Temperature gradient (degrees celcius/m)
```

```
%% Creating initial vectors
n=N+1;                      %(+1) to include start point in vectors
Temp=zeros(n,1);            %Temperature (degrees C)
Enthalpy=zeros(n,1);        %Enthalpy (kJ/kg)
P=zeros(n,1);               %Pressure (Pa)
Q=zeros(n,1);               %Heat transfer (W)
Rho=zeros(n,1);             %Density (kg/m^3)
P_friction=zeros(n,1);      %Pressure loss due to friction (Pa/m)
P_hydrostatic=zeros(n,1);   %Pressure loss due to hydrostatic (Pa/m)
Z=zeros(n,1);               %Height from reservoir (m)
P_fricPerc=zeros(n,1);      %friction contribution to pressure loss (%)
P_hsPerc=zeros(n,1);        %hydrostatic contribution to pressure loss (%)
T_sur=zeros(n,1);           %Surrounding Temperature (degrees C)
```

```
%% Setting Initial conditions into vectors
P(1)=P1;
P_hydrostatic(1)=(-g*(Rho1/P(1))*P(1).^2*sin(alfa))/P(1);
P_friction(1)=(-fd*((P(1)*Rho1*V1.^2)/(2*D)))/P(1);
Z(1)=0;
```

```
Rho(1)=XSteam('rho_ph',P1_bar,enthalpy_Res);
Temp(1)=T1_C;
T_sur(1)=20 + Temp_grad_meter*L;
Q(1)=U*A_ht*(Temp(1)-T_sur(1));
Enthalpy(1)=XSteam('h_pt',P(1)/(10.^5),Temp(1));
Cp(1)=XSteam('Cp_pT',P1_bar, T1_C);
P_fricPerc(1)=P_friction(1)/(P_friction(1)+P_hydrostatic(1))*100;
P_hsPerc(1)=P_hydrostatic(1)/(P_friction(1)+P_hydrostatic(1))*100;
Sum_hydrostatical=P_hydrostatic(1); %Used to sum hydrostatic contribution
Sum_frictional=P_friction(1);       %Used to sum frictional contribution

%% Euler Method Iteration
for i=2:n
    T_sur(i)=T_sur(i-1)-Temp_grad_meter*dL;
    P(i)=P(i-1)+dL*((-g*(Rho1/P(1))*P(i-1).^2*sin(alfa)- ...
    fd*((P(1)*Rho1*V1.^2)/(2*D)))/P(i-1));
    Z(i)=Z(i-1)+dL*sin(alfa);
    Q(i)=U*A_ht*(Temp(i-1)-T_sur(i));
    Enthalpy(i)=Enthalpy(i-1)-Q(i)/(m_dot*1000) -g/(1000)*(Z(i)-Z(i-1));
    Temp(i)=XSteam('T_ph',P(i)/(10.^5),Enthalpy(i));

    P_hydrostatic(i)=(-g*(Rho1/P(1))*P(i).^2*sin(alfa))/P(i);
    P_friction(i)=(-fd*((P(1)*Rho1*V1.^2)/(2*D)))/P(i);
    P_fricPerc(i)=P_friction(i)/(P_friction(i)+P_hydrostatic(i))*100;
    P_hsPerc(i)=P_hydrostatic(i)/(P_friction(i)+P_hydrostatic(i))*100;
    Sum_hydrostatical=Sum_hydrostatical+P_hydrostatic(i);
    Sum_frictional=Sum_frictional+P_friction(i);
end

%% Ploting figures
figure(1) %Plot of Pressure(MPa) vs Depth(m)
hold on
plot(P/(10.^6),Z-L*sin(alfa));
title('Pressure variation in pipe')
xlabel('Pressure (MPa)');
ylabel('Depth (m)');
axis([min(P)/(10.^6) max(P)/(10.^6) -L*sin(alfa) 0])
```

```
grid on
hold off

figure(2) %Plot of Enthalpy(kJ/kg) vs Depth(m)
hold on
plot(Enthalpy, Z-L*sin(alfa));
title('Enthalpy variation in pipe');
xlabel('Enthalpy (kJ/Kg)');
ylabel('Depth (m)');
grid on
hold off

figure(3) %plot of Temperature (degrees C) vs Depth (m)
hold on
plot(Temp, Z-L*sin(alfa));
title('Temperature variation in pipe')
xlabel('Temperature (\circC)');
ylabel('Depth (m)');
grid on
hold off

figure(4) %plot of frictional- vs hydrostatical pressure loss
hold on
plot(P_fricPerc,Z-L,P_hsPerc,Z-L);
legend(['Frictional losses. Total (%) = ' num2str(100*Sum_frictional/ ...
(Sum_frictional+Sum_hydrostatical))],['Hydrostatic losses. Total (%) ='...
num2str(100*Sum_hydrostatical/(Sum_frictional+Sum_hydrostatical))],...
'location','best');
title('Frictional VS Hydrostatical losses')
xlabel('Percentage of pressure loss contribution (%)');
ylabel('Depth (m)');
grid on
hold off
```

B.2 TEPP Alternating Mass Flow Rates Version v2.0 MatLab Script

```
%TEPP Alternating Mass Flow Rates (v2.0)
%% Input variables
T1_C=;          %Temperature in reservoir (degrees C)
P1=;            %Pressure in reservoir (Pa)
m_dot_start=;   %Lower mass flow rate (kg/s)
m_dot_end=;     %Upper mass flow rate (kg/s)
m_dot_step=;    %Increasing step of mass flow rate (kg/s)
L=;             %Length og pipe
D=;             %Diameter of production pipe section (m)
alfa=;          %Angle of pipe relative to horizontal direction (rad)
epsilon=;       %Pipe roughness (mm)
U=;             %Overall heat transfer coefficient (W/(m^2 K))
Temp_grad=;     %Temperature gradient(degrees/km)
N=;             %Number of iterations

%% Data
g=9.81;             %Gravitational constant(m/s^2)
M=18.015;           %Molecular weight water vapour(kg/kmol)
Ru=8314.472;        %Universal gas constant(J/(kmol*K))
R=Ru/M;             %Specific gas constant (J/(kg*K))


%% Calculations
dL=L/N;                                 %Iteration lenght (m)
epsilon=epsilon/1000;                   %Pipe roughness (m)
P1_bar=P1/(10.^5);                      %Pressure of reservoir (bar)
enthalpy_Res=XSteam('h_pt',P1_bar,T1_C);  %Enthalpy of reservoir (kJ/kg)
Rho1=XSteam('rho_ph',P1_bar,enthalpy_Res);%Density of reservoir (kg/m^3)
my=XSteam('my_pT',P1_bar,T1_C);           %Viscosity of reservoir (Pa*s)
A_ht=pi*D*dL;                           %Heat transfer surface (m^2)
Temp_grad_meter= Temp_grad/(1000);%Temperature gradient (degrees celcius/m)
n=N+1;                          %(+1) to include start point in vectors
```

```
%% Initiating Figures
figure(1)
hold on

figure(2)
hold on

figure(3)
hold on

%% Iterations
k=0;                        %Variable for storing legends
m_dot=m_dot_start;          %Variable for alternating mass flow rate
m=(m_dot_end-m_dot_start)/m_dot_step +1; %Iterations in first for-loop

%Outer for-loop for alternating mass flow rate and setting new conditions
for j=1:m
    k=k+1;
%Reseting vectors due to alternating mass flow rates
Temp=zeros(n,1);            %Temperature (degrees C)
Enthalpy=zeros(n,1);        %Enthalpy (kJ/kg)
P=zeros(n,1);               %Pressure (Pa)
Q=zeros(n,1);               %Heat transfer (W)
Rho=zeros(n,1);             %Density (kg/m^3)
Z=zeros(n,1);               %Height from reservoir (m)
T_sur=zeros(n,1);           %Surrounding Temperature (degrees C)

V1=m_dot/(Rho1*(D/2).^2*pi);    %Velocity (m/s)
Re=Rho1*V1*D/my;                %Reynolds number
fd2  = -1.8*log10((epsilon/(3.7*D))^1.11+6.9/Re);
fd=1/fd2^2;              %Darcy friction factor from Haaland fd2=1/sqrt(fd)

%Setting new initial conditions into vectors
P(1)=P1;
Z(1)=0;
Rho(1)=XSteam('rho_ph',P1_bar,enthalpy_Res);
Temp(1)=T1_C;
```

```
T_sur(1)=20 + Temp_grad_meter*L;
Q(1)=U*A_ht*(Temp(1)-T_sur(1));
Enthalpy(1)=XSteam('h_pt',P(1)/(10.^5),Temp(1));

%Inner for-loop running for a given mass flow rate
for i=2:n
     T_sur(i)=T_sur(i-1)-Temp_grad_meter*dL;
    P(i)=P(i-1)+dL*((-g*(Rho1/P(1))*P(i-1).^2*sin(alfa)- ...
    fd*((P(1)*Rho1*V1.^2)/(2*D)))/P(i-1));
    Z(i)=Z(i-1)+dL*sin(alfa);
    Q(i)=U*A_ht*(Temp(i-1)-T_sur(i));
    Enthalpy(i)=Enthalpy(i-1)-Q(i)/(m_dot*1000) -g/(1000)*(Z(i)-Z(i-1));
    Temp(i)=XSteam('T_ph',P(i)/(10.^5),Enthalpy(i));
end

legendInfo{k}=['Massflow (kg/s)= ' num2str(m_dot)];
figure(1)
plot(P/(10.^6),Z-L*sin(alfa));  %Plot to figure at current mass flow rate

figure(2)
plot(Enthalpy, Z-L*sin(alfa));  %Plot to figure at current mass flow rate

figure(3)
plot(Temp, Z-L*sin(alfa));      %Plot to figure at current mass flow rate


m_dot=m_dot+m_dot_step;         %Increase mass flow rate with step given
end
```

```
%% Adding figure info
figure(1)
legend(legendInfo,'location','best');
title('Pressure variation in pipe at different massflow rates');
xlabel('Pressure (MPa)');
ylabel('Depth (m)');
```

```
grid on
hold off

figure(2)
legend(legendInfo,'location','best');
title('Enthalpy variation in pipe at different massflow rates')
xlabel('Enthalpy (kJ/Kg)');
ylabel('Depth (m)');
grid on
hold off

figure(3)
legend(legendInfo,'location','best');
title('Temperature variation in pipe at different massflow rates)')
xlabel('Temperature (degrees)');
ylabel('Depth (m)');
grid on
hold off
```

Appendix C

Power Production - EES script

This appendix contain the scripts developed in EES for the five power plant designs analyzed in this study. The function “saturationindex” iterates isentropically from the given inlet turbine conditions down to the saturation line for a given pressure step. The accuracy of this iteration depends on the iteration step given. A smaller iteration step leads to a better accuracy, but results in more time consuming calculations. This function assumes that the conditions at the inlet of the turbine is at to the right of the saturated vapor line. Furthermore, state 1 is the condition of the reservoir examined in this study, and state 2 is the conditions at the wellhead of the geothermal system, previously calculated by the use of TEPP. Theory behind these scripts as well as results are presented in Chapter 4.

C.1 Case I: Single valve-turbine system. EES script.

```
Function saturationindex(P_start,s_inlet,P_step)
"Function providing the outlet turbine pressure for
given inlet pressure and entropy by assuming
an isentropic expansion"
x_final:=1 "Desired steam quality. Set by user."
P_iteration:=P_start

Repeat
P_iteration:=P_iteration - P_step
h:=enthalpy(Steam,P=P_iteration,s=s_inlet)
x:=quality(Steam,P=P_iteration,h=h)
Until(x<x_final)

saturationindex=P_iteration
End

{Isentropic efficiency}
n_t=0.85

{Variable to be optimized - outlet valve pressure}
P_out=2.841

{Determine the quality of the isentropic expansion}
x_a=quality(Steam,P=P_isentropic[4],h=h_isentropic[4])

{Conservation of mass flow rate}
m_dot[1]=50 [kg/s];
m_dot[2]=m_dot[1];
m_dot[3]=m_dot[2];
m_dot[4]=m_dot[3];

{State 1 - Reservoir}
P[1]=230 [bar]
T[1]=500 [C]
h[1]= enthalpy(Steam, P=P[1], T=T[1])
s[1]=entropy(Steam,T=T[1],P=P[1])
```

```
{State 2 - Well head - previously calculated by the use of TEPP}
P[2]=159.95 [bar]
T[2]= 459.22 [C]
h[2]= enthalpy(Steam, P=P[2], T=T[2])
s[2]=entropy(Steam,T=T[2],P=P[2])
{Valve calculation from point 2 to 3}
h[3]=h[2]

{state 3}
P[3]=P_out
T[3]=temperature(Steam, h=h[3],P=P[3])
s[3]=entropy(Steam,T=T[3],P=P[3])

{state 4s -isentropic expansion through turbine}
s_isentropic[4]=s[3]
P_isentropic[4]=saturationindex(P[3],s_isentropic[4],0.005)
h_isentropic[4]=enthalpy(Steam,s=s_isentropic[4], P=P_isentropic[4])
T_isentropic[4]=temperature(Steam,P=P_isentropic[4],s=s_isentropic[4])

{State 4r - exiting turbine conditions with assumed isentropic efficiency}
h[4]=h[3]-n_t*(h[3]-h_isentropic[4]) "Calculate 'real' enthalpy"
P[4]=P_isentropic[4]
s[4]=entropy(Steam,h=h[4],P=P[4])
T[4]=temperature(Steam,P=P[4],s=s[4])

{Work available from  turbine}
W_tot=m_dot[4]*(h[3]-h[4])
```

C.2 Case II: Double valve-turbine system. EES script.

```
Function saturationindex(P_start,s_inlet,P_step)
x_final:=1 "Desired steam quality. Set by user."
P_iteration:=P_start

Repeat
P_iteration:=P_iteration - P_step
h:=enthalpy(Steam,P=P_iteration,s=s_inlet)
x:=quality(Steam,P=P_iteration,h=h)
Until(x<x_final)

saturationindex=P_iteration
End

{Isentropic efficiency}
n_t=0.85

{Variables to be optimized - outlet valve pressure}
P_out=50.0793
P_out_2=0.73387

{Conservation of mass flow rate}
m_dot[1]=50 [kg/s]; m_dot[2]=m_dot[1];
m_dot[3]=m_dot[2]; m_dot[4]=m_dot[3];
m_dot[5]=m_dot[4]; m_dot[6]=m_dot[5];

{State 1 - Reservoir}
P[1]=230 [bar]
T[1]=500 [C]
h[1]= enthalpy(Steam, P=P[1], T=T[1])
s[1]=entropy(Steam,T=T[1],P=P[1])

{State 2 - Well head - previously calculated by the use of TEPP}
P[2]=159.95 [bar]
T[2]= 459.22 [C]
h[2]= enthalpy(Steam, P=P[2], T=T[2])
s[2]=entropy(Steam,T=T[2],P=P[2])
vol[2]=volume(Steam, T=T[2],P=P[2])
```

{Valve calculation from point 2 to 3}
h[3]=h[2]

{state 3}
P[3]=P_out
T[3]=**temperature**(***Steam***, ***h***=h[3],***P***=P[3])
s[3]=**entropy**(***Steam***,***T***=T[3],***P***=P[3])

{state 4s -isentropic expansion through turbine}
s_isentropic[4]=s[3]
P_isentropic[4]=**saturationindex**(P[3],s_isentropic[4],0.01)
h_isentropic[4]=**enthalpy**(***Steam***,***s***=s_isentropic[4], ***P***=P_isentropic[4])
T_isentropic[4]=**temperature**(***Steam***,***P***=P_isentropic[4],***s***=s_isentropic[4])

{State 4r - exiting turbine conditions with assumed isentropic efficiency}
h[4]=h[3]-n_t*(h[3]-h_isentropic[4])
P[4]=P_isentropic[4]
s[4]=**entropy**(***Steam***,***h***=h[4],***P***=P[4])
T[4]=**temperature**(***Steam***,***P***=P[4],***s***=s[4])

{Work delivered from turbine 1}
W[1]=m_dot[4]*(h[3]-h[4])

{Valve calculation from point 4 to 5}
h[5]=h[4]

{state 5}
P[5]=P_out_2
T[5]=**temperature**(***Steam***, ***h***=h[5],***P***=P[5])
s[5]=**entropy**(***Steam***,***T***=T[5],***P***=P[5])

{state 6s -isentropic expansion through turbine}
s_isentropic[6]=s[5]
P_isentropic[6]=**saturationindex**(P[5],s_isentropic[6],0.005)
h_isentropic[6]=**enthalpy**(***Steam***,***s***=s_isentropic[6], ***P***=P_isentropic[6])
T_isentropic[6]=**temperature**(***Steam***,***P***=P_isentropic[6],***s***=s_isentropic[6])

{State 6r - exiting turbine conditions with assumed isentropic efficiency}
h[6]=h[5]-n_t*(h[5]-h_isentropic[6])
P[6]=P_isentropic[6]
s[6]=**entropy**(***Steam***,***h***=h[6],***P***=P[6])
T[6]=**temperature**(***Steam***,***P***=P[6],***s***=s[6])
vol[6]=**volume**(***Steam***, ***T***=T[6],***P***=P[6])

```
{Work delivered from turbine 2}
W[2]=m_dot[6]*(h[5]-h[6])

{Total work available from all turbines}
W_tot=W[1]+W[2]
```

C.3 Case III: Triple valve-turbine system. EES script.

```
Function saturationindex(P,s,P_step)
x_final:=1.0
P_iteration:=P

Repeat
P_iteration:=P_iteration - P_step
h:=enthalpy(Steam,P=P_iteration,s=s)
x:=quality(Steam,P=P_iteration,h=h)
Until(x<x_final)

saturationindex=P_iteration
End

{Isentropic efficiency}
n_t=0.85

{Variables to be optimized - outlet valve pressure}
P_out=63.28 [bar]
P_out_2=1.366 [bar]
P_out_3=0.3 [bar]

{Conservation of mass flow rate}
m_dot[1]=50 [kg/s]; m_dot[2]=m_dot[1];
m_dot[3]=m_dot[2]; m_dot[4]=m_dot[3];
m_dot[5]=m_dot[4]; m_dot[6]=m_dot[5];
m_dot[7]=m_dot[6]; m_dot[8]=m_dot[7];

{State 1 - Reservoir}
P[1]=230 [bar]
T[1]=500 [C]
h[1]= enthalpy(Steam, P=P[1], T=T[1])
s[1]=entropy(Steam,T=T[1],P=P[1])
vol[1]=volume(Steam, P=P[1], T=T[1])
```

```
{State 2 - Well head - previously calculated by the use of TEPP}
P[2]=159.95 [bar]
T[2]= 459.22 [C]
h[2]= enthalpy(Steam, P=P[2], T=T[2])
s[2]=entropy(Steam,T=T[2],P=P[2])

{Valve calculation from point 2 to 3}
h[3]=h[2]

{state 3}
P[3]=P_out
T[3]=temperature(Steam, h=h[3],P=P[3])
s[3]=entropy(Steam,T=T[3],P=P[3])

{state 4s -isentropic expansion through turbine}
s_isentropic[4]=s[3]
P_isentropic[4]=saturationindex(P[3],s_isentropic[4],0.01)
h_isentropic[4]=enthalpy(Steam,s=s_isentropic[4], P=P_isentropic[4])
T_isentropic[4]=temperature(Steam,P=P_isentropic[4],s=s_isentropic[4])

{State 4r - exiting turbine conditions with assumed isentropic efficiency}
h[4]=h[3]-n_t*(h[3]-h_isentropic[4])
P[4]=P_isentropic[4]
s[4]=entropy(Steam,h=h[4],P=P[4])
T[4]=temperature(Steam,P=P[4],s=s[4])

{Work delivered from turbine 1}
W[1]=m_dot[4]*(h[3]-h[4])

{Valve calculation from point 4 to 5 through 2nd valve}
h[5]=h[4]

{state 5}
P[5]=P_out_2
T[5]=temperature(Steam, h=h[5],P=P[5])
s[5]=entropy(Steam,T=T[5],P=P[5])
vol[5]=volume(Steam, P=P[5], T=T[5])

{state 6s -isentropic expansion through turbine}
s_isentropic[6]=s[5]
P_isentropic[6]=saturationindex(P[5],s_isentropic[6],0.01)
h_isentropic[6]=enthalpy(Steam,s=s_isentropic[6], P=P_isentropic[6])
T_isentropic[6]=temperature(Steam,P=P_isentropic[6],s=s_isentropic[6])
```

```
{State 6r - exiting turbine conditions with assumed isentropic efficiency}
h[6]=h[5]-n_t*(h[5]-h_isentropic[6])
P[6]=P_isentropic[6]
s[6]=entropy(Steam,h=h[6],P=P[6])
T[6]=temperature(Steam,P=P[6],s=s[6])
vol[6]=volume(Steam, T=T[6],P=P[6])

{Work delivered from turbine 2}
W[2]=m_dot[6]*(h[5]-h[6])

{Valve calculation from point 6 to 7 through 3rd valve}
h[7]=h[6]

{state 7}
P[7]=P_out_3
T[7]=temperature(Steam, h=h[7],P=P[7])
s[7]=entropy(Steam,T=T[7],P=P[7])
vol[7]=volume(Steam, P=P[7], T=T[7])

{state 8s -isentropic expansion through turbine}
s_isentropic[8]=s[7]
P_isentropic[8]=saturationindex(P[7],s_isentropic[8],0.01)
h_isentropic[8]=enthalpy(Steam,s=s_isentropic[8], P=P_isentropic[8])
T_isentropic[8]=temperature(Steam,P=P_isentropic[8],s=s_isentropic[8])
vol[8]=volume(Steam, P=P[8], T=T[8])

{State 8r - exiting turbine conditions with assumed isentropic efficiency}
h[8]=h[7]-n_t*(h[8]-h_isentropic[8])
P[8]=P_isentropic[8]
s[8]=entropy(Steam,h=h[8],P=P[8])
T[8]=temperature(Steam,P=P[8],s=s[8])

{Work delivered from turbine 3}
W[3]=m_dot[8]*(h[7]-h[8])

{Total work available from all turbines}
W_tot=W[1]+W[2]+W[3]
```

C.4 Case IV: Single heat exchanger-double turbine system. EES script.

```
Function saturationindex(P,s,P_step)
x_final:=1.0
P_iteration:=P

Repeat
P_iteration:=P_iteration - P_step
h:=enthalpy(Steam,P=P_iteration,s=s)
x:=quality(Steam,P=P_iteration,h=h)
Until(x<x_final)

saturationindex=P_iteration
End

{Isentropic efficiency}
n_t=0.85

{Variables to be optimized - outlet valve pressure}
P_out=19.54


{Conservation of mass flow rate}
m_dot[1]=50 [kg/s]; m_dot[2]=m_dot[1];
m_dot[3]=m_cold; m_dot[4]=m_cold
m_dot[5]=m_cold; m_dot[6]=m_cold
m_dot[7]=m_cold; m_dot[8]=m_hot
m_dot[9]=m_hot

m_dot[2]=m_cold+m_hot
"m_cold and m_hot are yet not known as these are to be
determined from the heat exchanger performance
later in the process"

{State 1 - Reservoir}
P[1]=230 [bar]
T[1]=500 [C]
h[1]= enthalpy(Steam, P=P[1], T=T[1])
s[1]=entropy(Steam,T=T[1],P=P[1])
```

```
{State 2 - Well head - previously calculated by the use of TEPP}
P[2]=159.95 [bar]
T[2]= 459.22 [C]
h[2]= enthalpy(Steam, P=P[2], T=T[2])
s[2]=entropy(Steam,T=T[2],P=P[2])

{state 3}
h[3]=h[2]
P[3]=P[2]
s[3]=s[2]
T[3]=T[2]

{state 8}
h[8]=h[2]
P[8]=P[2]
s[8]=s[2]
T[8]=T[2]

{Valve calculation from point 3 to 4}
h[4]=h[3]

{state 4}
P[4]=P_out
T[4]=temperature(Steam, h=h[4],P=P[4])
s[4]=entropy(Steam,T=T[4],P=P[4])

{state 5s -isentropic expansion through turbine}
s_isentropic[5]=s[4]
P_isentropic[5]=saturationindex(P[4],s_isentropic[5],0.005)
h_isentropic[5]=enthalpy(Steam,s=s_isentropic[5], P=P_isentropic[5])
T_isentropic[5]=temperature(Steam,P=P_isentropic[5],s=s_isentropic[5])

{State 5r - exiting turbine conditions with assumed isentropic efficiency}
h[5]=h[4]-n_t*(h[4]-h_isentropic[5])
P[5]=P_isentropic[5]
s[5]=entropy(Steam,h=h[5],P=P[5])
T[5]=temperature(Steam,P=P[5],s=s[5])

{Work delivered from turbine 1}
W[1]=m_dot[5]*(h[4]-h[5])
```

```
{Heat Exchanger}
P_hot=P[8]                          "hot is the stream flowing from point 8-9"
P_cold=P[5]                         "Cold is the stream flowing from point 5-6"
T_hot_in=T_hot_out
T_hot_out=t_sat(Steam,P=P_hot)              "Set endpoint for point 9 in HE"
T_cold_in=T[5]
T_cold_out=T[9]-5                           "Pinch temperature"
h_cold_in=enthalpy(Steam, T=T_cold_in,P=P_cold)
h_cold_out=enthalpy(Steam, T=T_cold_out,P=P_cold)
h_hot_in=h[8]
h_hot_out=h[9]

m_hot*(h_hot_in - h_hot_out)=m_cold*(h_cold_out - h_cold_in)
"This equation along with the previous defined mass conservation equations
solves for the mass flow rates"

{Enthalpy of vaporization to ensure that point 9 is at the left side in the two phase
envelope}
hfg_hot=enthalpy_vaporization(Steam,T=T_hot_out)

{State 6}
P[6]=P[5]                                   "Assumed isobaric"
T[6]=T_cold_out
h[6]=enthalpy(Steam,P=P[6],T=T[6])
s[6]=entropy(Steam,h=h[6],P=P[6])

{state 9}
P[9]=P[8]                                   "Assumed isobaric"
h[9]=enthalpy(Steam,P=P_hot,T=T_hot_in)-hfg_hot
T[9]=T_hot_out
s[9]=entropy(Steam, h=h[9],P=P[9])

{state 7s -isentropic expansion through 2nd turbine}
s_isentropic[7]=s[6]
P_isentropic[7]=saturationindex(P[6],s_isentropic[7],0.005)
h_isentropic[7]=enthalpy(Steam,s=s_isentropic[7], P=P_isentropic[7])
T_isentropic[7]=temperature(Steam,P=P_isentropic[7],s=s_isentropic[7])

{State 7r - exiting turbine conditions with assumed isentropic efficiency}
h[7]=h[6]-n_t*(h[6]-h_isentropic[7])
P[7]=P_isentropic[7]
s[7]=entropy(Steam,h=h[7],P=P[7])
T[7]=temperature(Steam,P=P[7],s=s[7])
```

```
{Work delivered from turbine 2}
W[2]=m_dot[7]*(h[6]-h[7])

{Total work available from all turbines}
W_tot=W[1]+W[2]
```

C.5 Case V: Double heat exchanger-triple turbine system. EES script.

```
Function saturationindex(P,s,P_step)
x_final:=1.0
P_iteration:=P

Repeat
P_iteration:=P_iteration - P_step
h:=enthalpy(Steam,P=P_iteration,s=s)
x:=quality(Steam,P=P_iteration,h=h)
Until(x<x_final)

saturationindex=P_iteration
End

{Isentropic efficiency}
n_t=0.85

{Variables to be optimized - outlet valve pressure}
P_out=81.64

{Conservation of mass flow rate}
m_dot[1]=50 [kg/s]; m_dot[2]=m_dot[1]
m_dot[4]=m_dot[3]; m_dot[5]=m_dot[3]
m_dot[6]=m_dot[3]; m_dot[7]=m_dot[3]
m_dot[8]=m_dot[3]; m_dot[9]=m_dot[3]
m_dot[12]=m_dot[11]; m_dot[14]=m_dot[13]

{Mass balance equations}
m_dot[2]=m_dot[3]+m_dot[10]
m_dot[10]=m_dot[11]+m_dot[13]

{State 1 - Reservoir}
P[1]=230 [bar]
T[1]=500 [C]
h[1]= enthalpy(Steam, P=P[1], T=T[1])
s[1]=entropy(Steam,T=T[1],P=P[1])
vol[1]=volume(Steam, P=P[1], T=T[1])
```

```
{State 2 - Well head - previously calculated by the use of TEPP}
P[2]=159.95 [bar]
T[2]= 459.22 [C]
h[2]= enthalpy(Steam, P=P[2], T=T[2])
s[2]=entropy(Steam,T=T[2],P=P[2])

{state 3}
h[3]=h[2]
P[3]=P[2]
s[3]=s[2]
T[3]=T[2]

{state 10}
h[10]=h[2]
P[10]=P[2]
s[10]=s[2]
T[10]=T[2]

{state 11}
h[11]=h[10]
P[11]=P[10]
s[11]=s[10]
T[11]=T[10]

{State 13}
h[13]=h[10]
P[13]=P[10]
s[13]=s[10]
T[13]=T[10]

{Valve calculation from point 3 to 4}
h[4]=h[3]

{state 4}
P[4]=P_out
T[4]=temperature(Steam, h=h[4],P=P[4])
s[4]=entropy(Steam,T=T[4],P=P[4])

{state 5s -isentropic expansion through turbine}
s_isentropic[5]=s[4]
P_isentropic[5]=saturationindex(P[4],s_isentropic[5],0.005)
h_isentropic[5]=enthalpy(Steam,s=s_isentropic[5], P=P_isentropic[5])
T_isentropic[5]=temperature(Steam,P=P_isentropic[5],s=s_isentropic[5])
```

```
{State 5r - exiting turbine conditions with assumed isentropic efficiency}
h[5]=h[4]-n_t*(h[4]-h_isentropic[5])
P[5]=P_isentropic[5]
s[5]=entropy(Steam,h=h[5],P=P[5])
T[5]=temperature(Steam,P=P[5],s=s[5])

{Work delivered from turbine 1}
W[1]=m_dot[5]*(h[4]-h[5])

{1st Heat Exchanger}
m_hot=m_dot[11]                    "hot is the stream flowing from point 11-12"
m_cold=m_dot[5]                    "cold is the stream flowing from point 5-6"
P_hot=P[11]
P_cold=P[5]
T_hot_in=T_hot_out
T_hot_out=t_sat(Steam,P=P_hot)     "Set endpoint for point 12 in HE"
T_cold_in=T[5]
T_cold_out=T[12]-5                 "Pinch temperature"
h_cold_in=enthalpy(Steam, T=T_cold_in,P=P_cold)
h_cold_out=enthalpy(Steam, T=T_cold_out,P=P_cold)
h_hot_in=h[11]
h_hot_out=h[12]

m_hot*(h_hot_in-h_hot_out)=m_cold*(h_cold_out - h_cold_in)
"This equation along with the previous defined mass conservation equations
and the equation for the 2nd heat exchanger solves for the mass flow rates"

{Enthalpy of vaporization to ensure that point 9 is at the left side in the two phase
envelope}
hfg_hot=enthalpy_vaporization(Steam,T=T_hot_out)

{State 6}
P[6]=P[5]
T[6]=T_cold_out                    "Assumed isobaric"
h[6]=enthalpy(Steam,P=P[6],T=T[6])
s[6]=entropy(Steam,h=h[6],P=P[6])

{State 12}
P[12]=P[11]                        "Assumed isobaric"
h[12]=enthalpy(Steam,P=P_hot,T=T_hot_in)-hfg_hot
T[12]=T_hot_out
s[12]=entropy(Steam, h=h[12],P=P[12])
```

```
{state 7s -isentropic expansion through 2nd turbine}
s_isentropic[7]=s[6]
P_isentropic[7]=saturationindex(P[6],s_isentropic[7],0.001)
h_isentropic[7]=enthalpy(Steam,s=s_isentropic[7], P=P_isentropic[7])
T_isentropic[7]=temperature(Steam,P=P_isentropic[7],s=s_isentropic[7])

{State 7r - exiting turbine conditions with assumed isentropic efficiency}
h[7]=h[6]-n_t*(h[6]-h_isentropic[7])
P[7]=P_isentropic[7]
s[7]=entropy(Steam,h=h[7],P=P[7])
T[7]=temperature(Steam,P=P[7],s=s[7])

{Work delivered from turbine 2}
W[2]=m_dot[7]*(h[6]-h[7])

{2nd Heat Exchanger}
m_hot_2=m_dot[13]                    "hot is the stream flowing from point 13-
14"
P_hot_2=P[13]                        "the 'cold' stream is the same as in 1st
HE"
P_cold_2=P[7]
T_hot_in_2=T_hot_out_2
T_hot_out_2=t_sat(Steam,P=P_hot_2)   "Set endpoint for HE"
T_cold_in_2=T[7]
T_cold_out_2=T[14]-5                 "Pinch temperature"
h_cold_in_2=enthalpy(Steam, T=T_cold_in_2,P=P_cold_2)
h_cold_out_2=enthalpy(Steam, T=T_cold_out_2,P=P_cold_2)
h_hot_in_2=h[13]
h_hot_out_2=h[14]

m_hot_2*(h_hot_in_2-h_hot_out_2)=m_cold*(h_cold_out_2 - h_cold_in_2)

{Enthalpy of vaporization to ensure that point 14 is at the left side in the two phase
envelope}
hfg_hot_2=enthalpy_vaporization(Steam,T=T_hot_out_2)

{State 8}
P[8]=P[7]
T[8]=T_cold_out_2                    "Assumed isobaric"
h[8]=enthalpy(Steam,P=P[8],T=T[8])
s[8]=entropy(Steam,h=h[8],P=P[8])

{State 14}
P[14]=P[13]                          "Assumed isobaric"
h[14]=enthalpy(Steam,P=P_hot_2,T=T_hot_in_2)-hfg_hot_2
T[14]=T_hot_out_2
s[14]=entropy(Steam, h=h[14],P=P[14])
```

{state 9s -isentropic expansion through 3rd turbine}
s_isentropic[9]=s[8]
P_isentropic[9]=**saturationindex**(P[8],s_isentropic[9],0.001)
h_isentropic[9]=**enthalpy**(***Steam***,***s***=s_isentropic[9], ***P***=P_isentropic[9])
T_isentropic[9]=**temperature**(***Steam***,***P***=P_isentropic[9],***s***=s_isentropic[9])

{State 9r - exiting turbine conditions with assumed isentropic efficiency}
h[9]=h[8]-n_t*(h[8]-h_isentropic[9])
P[9]=P_isentropic[9]
s[9]=**entropy**(***Steam***,***h***=h[9],***P***=P[9])
T[9]=**temperature**(***Steam***,***P***=P[9],***s***=s[9])

{Work delivered from turbine 3}
W[3]=m_dot[9]*(h[8]-h[9])

{Total work available from all turbines}
W_tot=W[1]+W[2]+W[3]

Appendix D

Case Study - Additional Thermodynamic Data

This appendix provides additional thermodynamic diagrams and tables to those presented in sub-chapter 4.1, including pressure-enthalpy diagrams for all the Models evaluated.

D.1 Model I

Table D.1: Thermodynamic properties at each state of Model I with saturated steam exiting the turbine exhaust with a vapour quality of 1.0, as shown in Figure.D.2. Calculated with the developed EES script, available in Appendix C.1.

State	h (kJ/kg)	$\dot{m}$ (kg/s)	P (bar)	s (kJ/kg-K)	T (°C)	P_{is} (bar)	T_{is} (°C)
1	3197	50	230	6.035	500		
2	3171	50	160	6.136	459.2		
3	3171	50	5.39	7.605	351.6		
4	2609	50	0.20	7.902	60.38	0.20	60.38

Table D.2: Thermodynamic properties at each state of Model I with saturated steam exiting the turbine exhaust with a vapour quality of 0.85, as shown in Figure.D.3. Calculated with the developed EES script, available in Appendix C.1.

State	h (kJ/kg)	$\dot{m}$ (kg/s)	P (bar)	s (kJ/kg-K)	T (°C)	P_{is} (bar)	T_{is} (°C)
1	3197	50	230	6.035	500		
2	3171	50	160	6.136	459.2		
3	3171	50	5.39	7.605	351.6		
4	2609	50	0.20	7.902	60.38	0.20	60.38

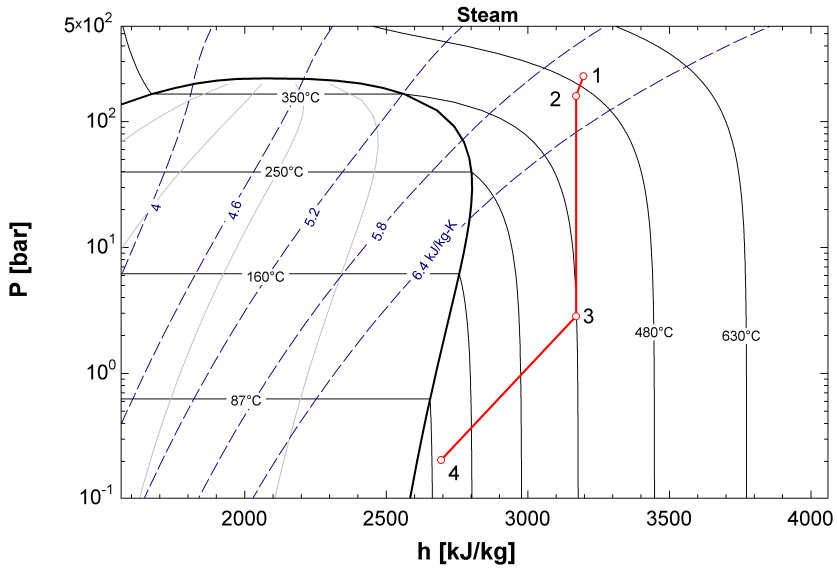

Figure D.1: Pressure-enthalpy diagram for Model I as sketched in Figure 4.11 with calculated thermodynamic properties in Table 4.3.

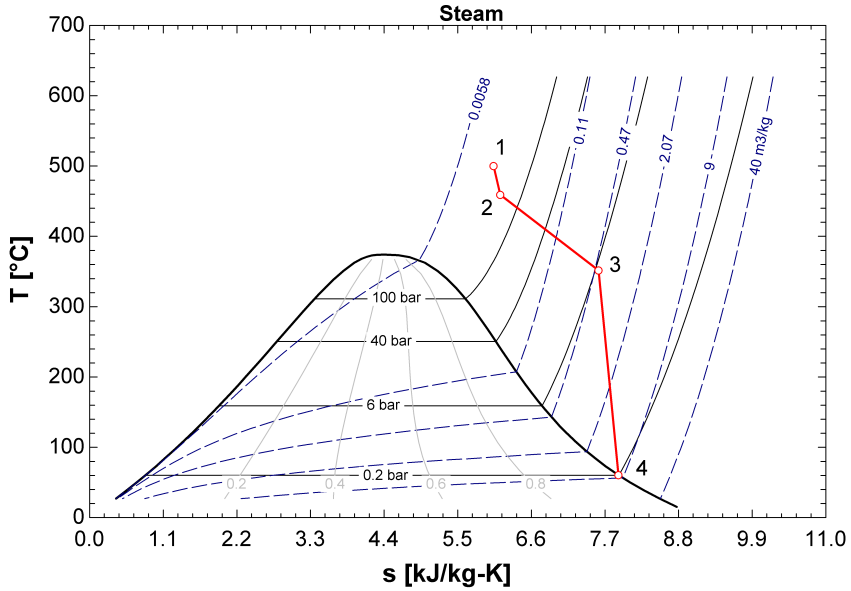

Figure D.2: Temperature-entropy diagram for Model I with saturated steam exiting the turbine exhaust with a vapour quality of 1, with thermodynamic properties in Table D.1.

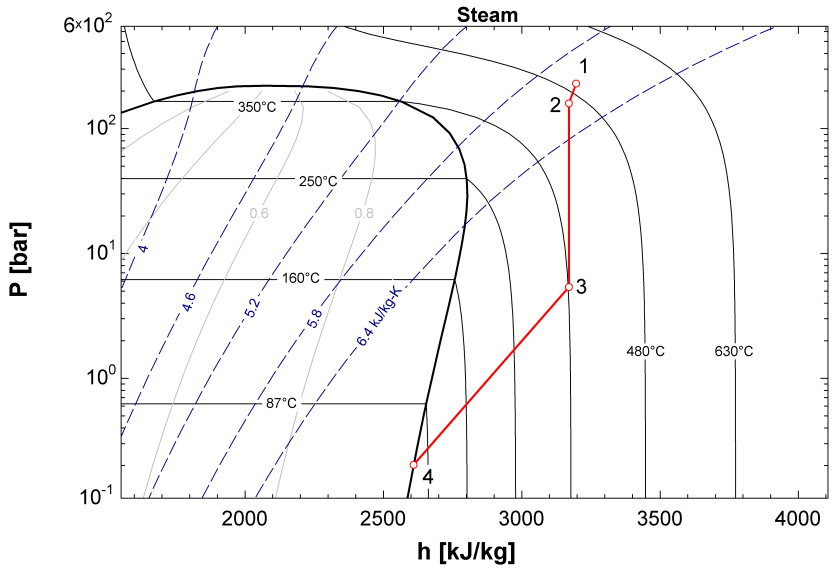

Figure D.3: Pressure-enthalpy diagram for Model I with saturated steam exiting the turbine exhaust with a vapour quality of 1, with thermodynamic properties in Table D.1.

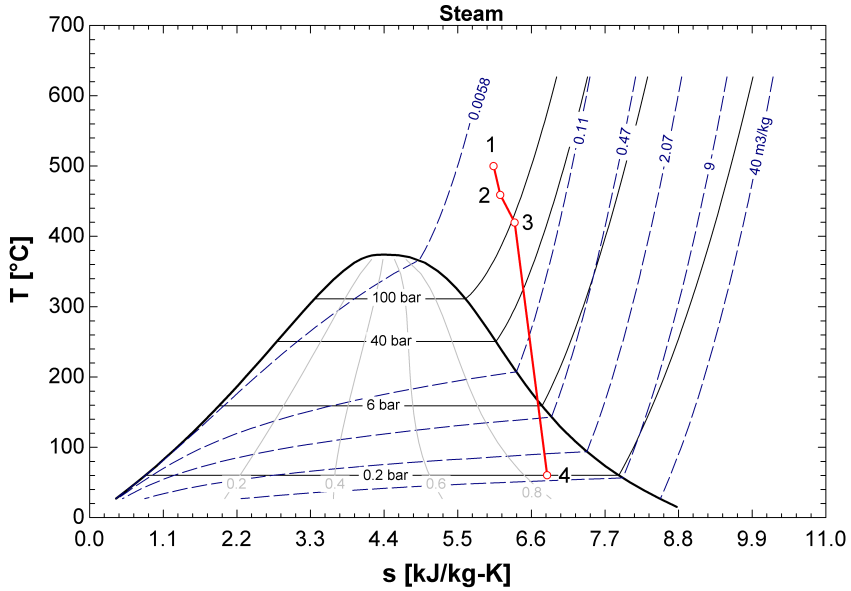

Figure D.4: Temperature-entropy diagram for Model I with steam exiting the turbine exhaust with a vapour quality of 0.85, with thermodynamic properties in Table D.2.

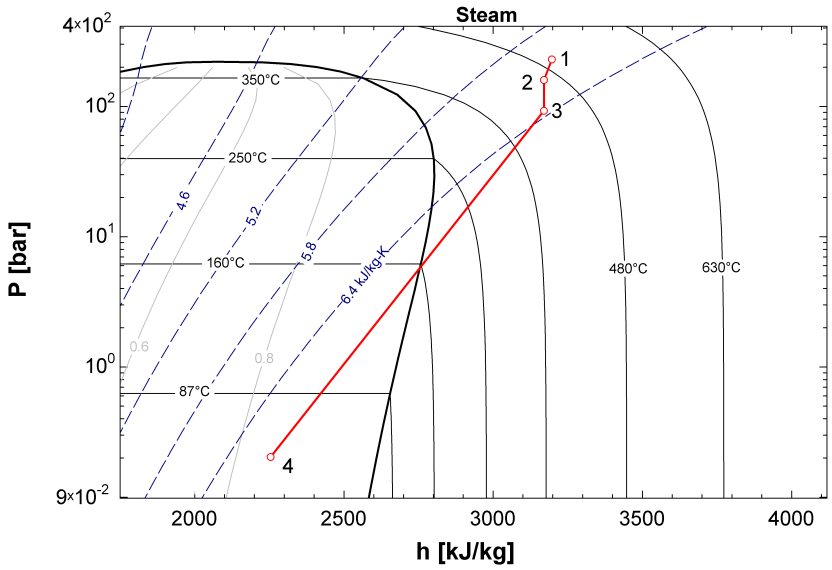

Figure D.5: Pressure-enthalpy diagram for Model I with steam exiting the turbine exhaust with a vapour quality of 0.85, with thermodynamic properties in Table D.2.

D.2 Model II

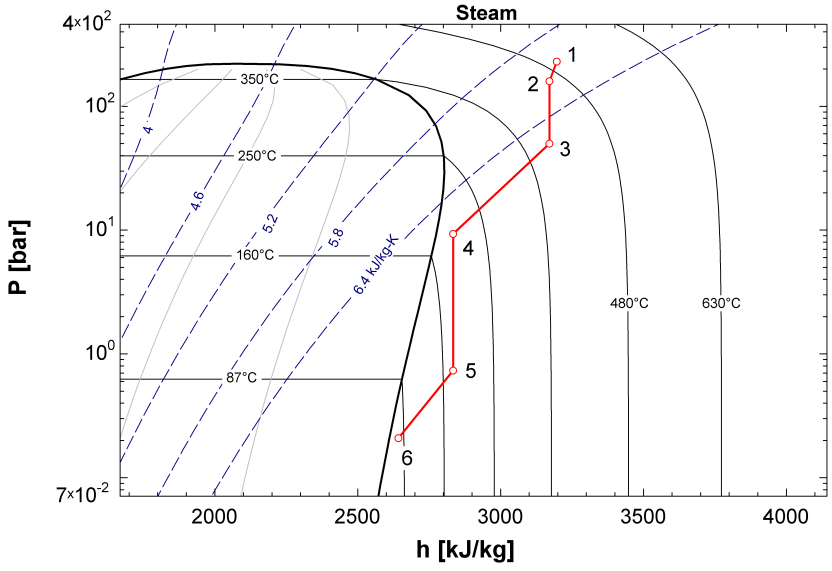

Figure D.6: Pressure-enthalpy diagram for Model II as sketched in Figure 4.13 with calculated thermodynamic properties in Table 4.5.

D.3 Model III

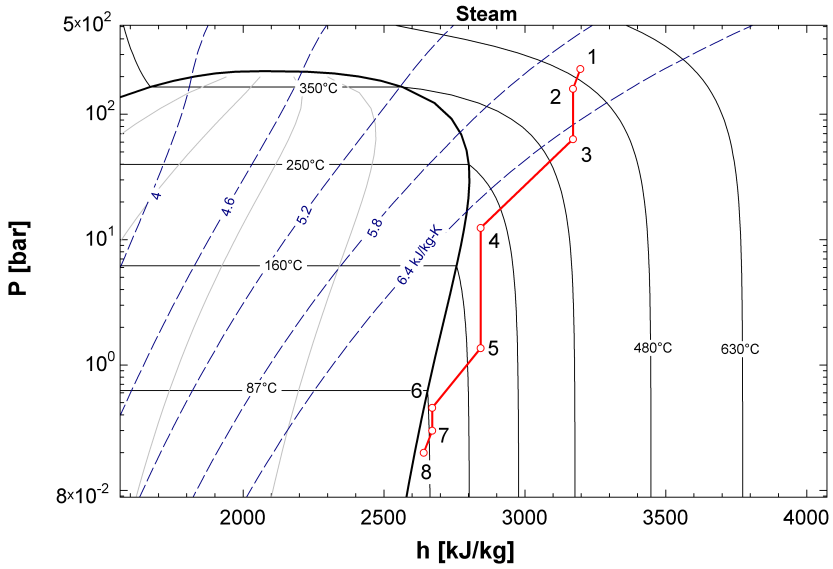

Figure D.7: Pressure-enthalpy diagram for Model III as sketched in Figure 4.15 with calculated thermodynamic properties in Table 4.8.

D.4 Model IV

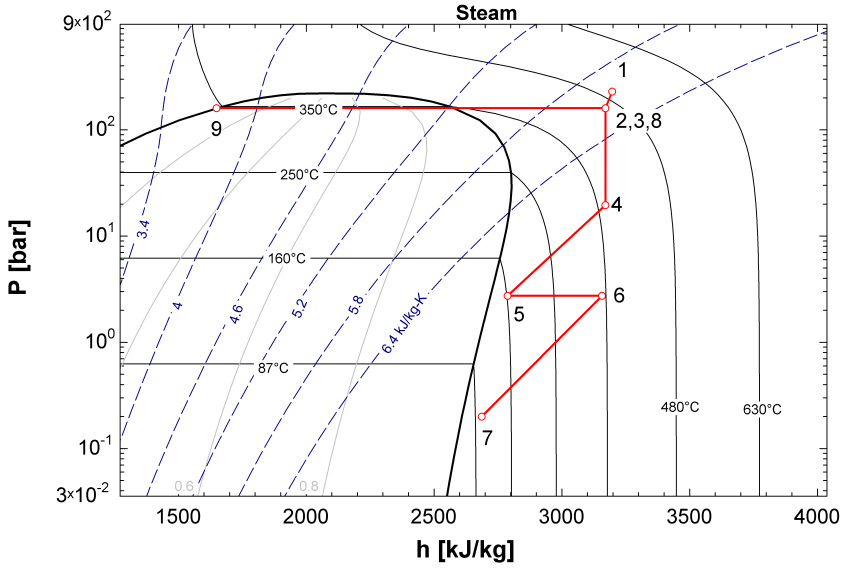

Figure D.8: Pressure-enthalpy diagram for Model IV as sketched in Figure 4.17 with calculated thermodynamic properties in Table 4.9.

D.5 Model V

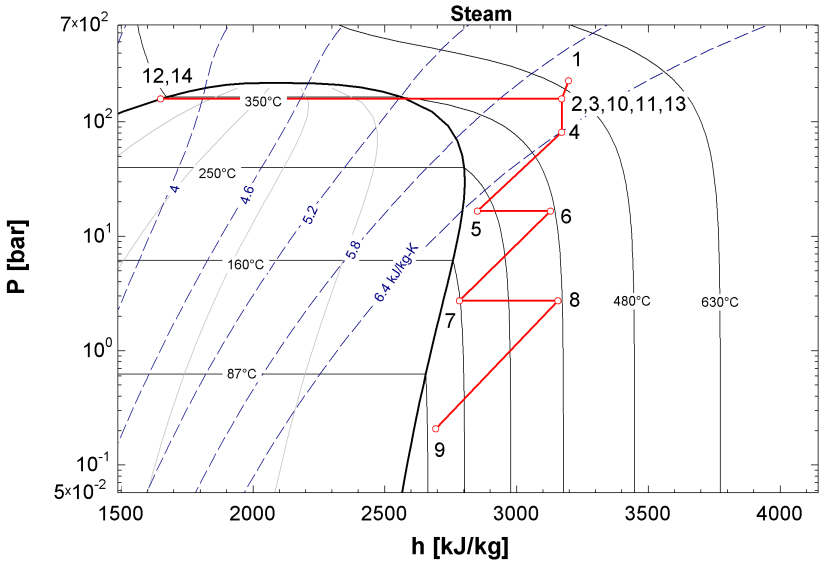

Figure D.9: Pressure-enthalpy diagram for Model V as sketched in Figure 4.19 with calculated thermodynamic properties in Table 4.12.